

Reactions of Organic Molecules on Metal Surfaces studied by STM.

INAUGURALDISSERTATION

zur

Erlangung der Würde eines Doktors der Philosophie

vorgelegt der

Philosophisch-Naturwissenschaftlichen Fakultät

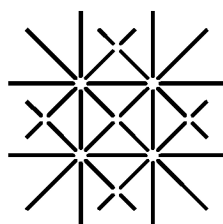
der Universität Basel

von

Markus Wahl

aus Weinstadt (Deutschland)

Basel, 2006



UNI
BASEL

Genehmigt von der Philosophisch-Naturwissenschaftlichen Fakultät auf Antrag von:

Prof. Dr. H.-J. Güntherodt

Prof. Dr. E. Meyer

Dr. T.A. Jung

Basel, den 21. November 2006

Prof. Dr. Hans-Peter Hauri, Dekan

Abstract

Two distinct systems of surface reactions involving complex organic molecules were studied on single crystal metal surfaces by Scanning Tunneling Microscopy (STM), Low Energy Electron Diffraction (LEED) and X-ray Photoelectron Spectroscopy (XPS) under ultra high vacuum conditions.

The first system focused on the Pt-cinchona alkaloid system, which is a powerful catalytic system in the field of enantioselective heterogeneous catalysis. Herein, an achiral reactant molecule is hydrogenated over a cinchona alkaloid modified platinum surface. Due to the modification of the surface with the chiral cinchona modifier, the symmetry of the system is broken and enantioselectivity is introduced. The hydrogenation of the reactant therefore is biased and leads to an enantiomeric excess (ee) of one enantio form of the product.

The aim of the present STM study was to gain direct insight in the molecular processes which occur during adsorption of such modifiers and reactants. Therefore, the adsorption of cinchonidine (CD), cinchonine (CN) and 2,2,2-trifluoroacetophenone (TFAP) was investigated on both Pt(111) and Pd(111) single crystal surfaces in the presence and absence of hydrogen. Different adsorption modes were identified and a change in adsorption geometry upon addition of hydrogen was followed. The findings are discussed in the light of catalytic, theoretical and spectroscopic data available for this system. Our work showed, that the discrimination of different surface species by their mobility and the time-resolved observation of their surface chemical processes by STM provides a powerful tool for the investigation of complex catalyst systems. These studies can complement other surface analytical methods and quantum chemical calculations in order to gain insight into the mechanistic aspects.

The second system is an example how surface reactions can be used to convert large organic molecules subsequent to their deposition in order to efficiently self-assemble larger structures. For this purpose a perylene derivative, 4,9-diaminoperylene-quinone-3,10-diimine (DPDI), was deposited on a Cu(111) single crystal surface and investigated by STM. These highly mobile precursor molecules are then transformed via a thermally induced surface-assisted dehydrogenation reaction by annealing in-situ at 300 °C. The resulting molecules form autocomplementary species of hydrogen-bond donor and acceptors and thereby can interact with each other via H-bonding. Depending on the surface concentration prior to annealing different well-order molecular patterns are created.

The most stable structure among these molecular patterns is an open hexagonal structure. Due to an exact register with the Cu surface and due to a strong so-called resonance-assisted hydrogen-bonding (RAHB) this highly robust and porous structure is well-suited for the incorporation or trapping of guest molecules. Trapping and manipulation experiments of C₆₀ and octaethylporphyrins (OEP) inside the network are presented and discussed.

Contents

Abstract	i
Abbreviations	v
1 Introduction	1
1.1 Motivation and Outline	1
2 Experimental Methods	5
2.1 Scanning Tunneling Microscopy	5
2.1.1 Introduction	5
2.1.2 Theory of STM	6
2.1.3 Imaging Adsorbates with STM	9
2.1.4 Diffusion of Adsorbates	10
2.2 Low Energy Electron Diffraction	11
2.3 X-ray and UV Photoelectron Spectroscopy	14
2.4 The UHV System	15
2.5 Liquid Deposition System	18
2.6 Single Crystal Electron Bombardment Station	19
3 The Pt-Cinchona Alkaloid System	21
3.1 Motivation	21
3.2 Definitions of Stereochemistry	22
3.3 The Cinchona Alkaloid Modified Catalysis on Platinum Metals	24
3.4 Sample Preparation	26
3.5 CD on Pt(111)	27
3.6 CN on Pt(111)	34
3.7 TFAP on Pt(111)	35
3.8 CD on Pd(111)	37
3.9 Discussion	38
3.10 Conclusions and Outlook	41
4 Assembling Organic Molecules on Surfaces with In-situ Reactions	43
4.1 Motivation	43
4.2 A Short Introduction to the Chemistry of DPDI	44
4.3 DPDI on Cu(111) - Linear Chains	46
4.4 DPDI on Cu(111) - Hexagonal Networks	49
4.5 DPDI on Cu(111) - Trimeric Bowls	51
4.6 Discussion	53
4.7 XPS Measurements	56
4.8 Co-adsorbed Mixtures of DPDI and PTCDA	59

Contents

4.9	Trapping Subsequently Deposited Molecules	61
4.9.1	C ₆₀ and OEP at Room-temperature	62
4.9.2	C ₆₀ and OEP at 77 K	63
4.9.3	OEP Switching	64
4.9.4	Manipulation	66
4.10	Conclusions and Outlook	68
	Bibliography	71
	List of Publications	87
	Acknowledgements	89
	Curriculum Vitae	91

Abbreviations

AFM	Atomic Force Microscopy
ATR-IR	Attenuated Total Reflection Infrared Spectroscopy
CD	Cinchonidine
CN	Cinchonine
DFT	Density Functional Theory
DOS	Density of States
DPDI	4,9-diaminoperylene-quinone-3,10-diimine
ESCA	Electron Spectroscopy for Chemical Analysis
HOMO	Highest Occupied Molecular Orbital
LDOS	Local Density of States
LEED	Low Energy Electron Diffraction
LUMO	Lowest Unoccupied Molecular Orbital
ML	Monolayer
OEP	Octaethyl Porphyrin
OLED	Organic Light Emitting Diode
PTCDA	Perylene-3,4,9,10-tetracarboxylic-dianhydride
PES	Photoelectron Spectroscopy
STM	Scanning Tunneling Microscope
STS	Scanning Tunneling Spectroscopy
TFAP	2,2,2-Trifluoroacetophenone
UHV	Ultra-high Vacuum
UPS	Ultraviolet Photoelectron Spectroscopy
XPS	X-ray Photoelectron Spectroscopy
XSW	X-ray Standing Wavefield

1 Introduction

1.1 Motivation and Outline

Since the beginning of science, when there were only the four elements earth, air, fire, and water to distinguish, one was not only interested in the description of these elements, but rather in their interaction. Soon the investigation of reactions alone turned into the very prospering scientific field of chemistry. The impact of chemistry on technology and daily life was always strong and is nowadays stronger than ever: for example if one imagines the huge differences between a world before the emergence of synthetic materials and the world to day. These synthetic materials are the product of organic chemistry.

Most organic synthesis is normally performed in solution, which is reasonable because the physics of chemical reactions are governed by coulomb interactions of the participating atoms or molecular units. In contrast to gravitational interactions which are a typical bulk feature, these coulomb interactions are mediated through the surface of matter. Nevertheless, a lot of matter on earth is solid and chemistry on solid surfaces is central to many areas of practical interest such as heterogeneous catalysis, tribology, electrochemistry and materials processing. With the rise of surface sensitive techniques in the past decades [1], a lot of information and knowledge has been gathered on surface reactions. The adsorption and reaction kinetics of simple inorganic molecules of catalytical systems were extensively studied on single crystal model surfaces [2]. Especially the field of catalysis related surface science studies blossomed, because the industrial need for efficient chemical processes with both low energy consumption and low environmental impact has stimulated the quest for improved catalytic systems.

However, there are huge differences in reactions on surfaces compared to reactions in solution. First of all, the chemical reaction process on surface includes additional reaction steps. Reactants involved in a surface reaction in a first step have to adsorb on that surface and can even adsorb in a variety of different adsorption modes among which only a certain fraction is the chemical active adsorption mode. Furthermore, this first adsorption step is perhaps only an intermediate state for a reactant as e.g. H_2 , which further on has to dissociate to become chemically active. In a second phase the reactants have to meet on the surface that the reaction can proceed at all. In many systems this involves a specific place on the surface, the so-called active site [3], e.g. a step edge or a kink site along a step edge. Diffusion and by that complex molecule-substrate interactions play hence an important role during this step. Additionally, these molecule-substrate interactions may also lead to conformational changes of the reactants upon adsorption or may even induce surface reconstructions caused by the adsorbates.

Because the atoms of organic molecules are covalently bond, all chemical reactions have to entail bond forming, bond breaking or both. The actual reaction pathway therefore often involves a certain attack step where geometrical or sterical aspects play an important role. For example a π -double-bond can not be attacked by a substituent in the nodal plane of its constituting p -orbitals since they do not have any probability density in this plane. Due to the

restriction to two dimensions for reactions on a surface, steric hindrance is of more importance than in solution where the reactants can arrange freely in three dimensions. Therefore the conformational flexibility of larger molecules [4] plays an important role to overcome such steric hindrances. On the other hand, as will be seen in the Pt-cinchona chapter of this thesis, this conformational flexibility may also cause difficulties for experimental methods like STM in terms of resolution.

Finally, the reaction product has to desorb from the surface and its adsorption strength competes with the adsorption strength of new reactants, which try to adsorb on the surface, slowing down or even hindering this adsorption process. Also side products of the reaction might hinder the adsorption of new reactants. In catalysis this is known as poisoning and is a major issue for the longterm efficiency of a catalyst.

Only very recently, surface science studies in this field have been expanded to the study of the chemistry of relatively complex organic molecules on surfaces, in large measure in connection with the selective synthesis and catalysis of fine chemicals and pharmaceuticals (for an extensive review see Z. Ma and F. Zaera [5]). Although the major advances of catalysis were a consequence of mostly empirical trials, advances in the scientific understanding of catalytic systems contributed to further improvement. Therefore the motivation for the work presented in chapter 3 was to further complete the scientific picture of such a complex catalytic system, namely the Pt-cinchona system. This heterogeneous catalytic system can be used for the enantioselective hydrogenation of achiral reactants.

Another strong motivation for research in the field of organic molecules and organic reactions on surfaces is the fascinating idea of molecular electronics. In 1974 Aviram and Ratner proposed a rectifier consisting of a single molecule [6] and thereby marked the laying of the cornerstone of molecular electronics. They suggested that a molecule with a donor-spacer-acceptor structure would behave as a diode when placed between two metallic electrodes. With its basic ideas already established by Feynman in 1960 [7] molecular electronics seeks to use individual molecules to perform non-linear electronic functions as e.g. rectification, amplification or storage. Herein, the necessity of non-linearity for most electronic devices excellently coincides with the non-linearity of quantum mechanical effects which rule the physics of nanoscale systems.

For the same reason of non-linearity of quantum mechanical effects an important point is the reproducibility of such nanoscale systems in order to exactly define the energy levels involved in the functional mechanisms. Organic molecules are made up of covalently bond atoms and are therefore well-defined atomic systems. To use organic molecules as basic building blocks of molecular electronics thus is a natural choice because large amounts of organic molecules can be repeatedly produced with an exactly defined number of atoms and chemical structure. Additionally, the electronic properties of organic molecules can be fine-tuned by variation of certain substituents. A final step along the road to molecular nanoelectronics is then the ability to order the single devices into hierarchical structures forming an electronic circuit. Such ordering processes must follow the same reproducibility and scalability rules known from classical semiconductor electronics in order to be of technological relevance.

In this context it can be very interesting to investigate how reactions of organic molecules can be used to build up higher hierarchical structures by self-assembly [8] on a surface. For this purpose the STM is an invaluable instrument, because it uses the 3rd dimension perpendicular to the surface for an investigative access to the planar molecular structures and reactions on the atomic scale. The fact that STM creates a real-space image of the surface also excellently supports the investigation of sometimes complex hierarchical structures.

In the following, chapter 2 introduces the experimental methods and the instrumentation used in the course of this thesis. Since the work presented in this thesis is based on two distinct projects, chapter 3 and 4 both include their own motivation and conclusion section and can be read separately. Chapter 3 presents our results on a heterogeneous asymmetric catalytic system, the so-called Pt-cinchona alkaloid system. Chapter 4 shows the possibilities and limits of state-of-the-art self-ordering phenomena exemplified by means of a thermally induced surface-assisted reaction which then leads to the formation of highly ordered structures.

2 Experimental Methods

This chapter describes the experimental methods and tools used in this thesis with a special emphasis on scanning tunneling microscopy.

2.1 Scanning Tunneling Microscopy

2.1.1 Introduction

The invention of the scanning tunneling microscope (STM) about 25 years ago in 1981 by Gerd Binnig and Heinrich Rohrer [9] marked a milestone of surface investigation techniques. With the STM a new era of surface science was introduced, since this technique allowed for investigations of many different surfaces in real space with atomic resolution. Its impact on surface science was honored just five years later in 1986 when Binnig and Rohrer received the Nobel Prize for their invention. As the name implies, scanning tunneling microscopy is based on the quantum mechanical tunneling effect through thin energy barriers. In scanning tunneling microscopy a sharp conducting tip is brought into close proximity (in the order of a few Å) to a conductive sample. For the electrons in the two conductors the gap in-between represents an impenetrable energy barrier which cannot be overcome according to classical theory. But since electrons are quantum mechanical objects and the energy barrier is thin, electrons can tunnel through the barrier and give rise to a net tunneling current I in the nanoampere range if a small bias voltage is applied between tip and sample. To obtain a 2D image of the sample surface the tip is then scanned across the surface by piezo-electric actuators. While moving the tip, the corrugation of the sample surface induces variations of the tip sample distance z , which in turn drastically affects the tunneling current. As a rule of thumb, the current reduces by one order of magnitude for an increase of the gap distance by 1 Å. It is exactly this exponential behaviour that is the reason for the high lateral and - to some extent - vertical resolution of scanning tunneling microscopy, because around 90% of the tunneling current is passing through the topmost atom of the tip-apex, if we assume it protrudes about 1 Å further out than the other tip atoms.

Several modes of operation are used while scanning the tip across the surface. In the so called *constant height* mode the z distance is kept constant and the changes in I are measured. Another alternative mode—actually the one most frequently used—is the *constant current* mode, where a feedback system is used to adjust the tip sample distance z in order to keep the tunneling current constant at a certain current set point. In this mode the topographic information is therefore shifted to the feedback output signal z , which is acquired with a data acquisition system and fed to the z piezo-actuator. Generally, the *constant height* mode is used for fast scanning, but the sample has to be perfectly flat and thermal drift has to be small to prevent the tip from crashing into the sample. The *constant current* mode is safer and yields good resolution at the expense of lower scan speeds. The STM images presented in this thesis, for instance, have all been acquired in constant current mode, recording the

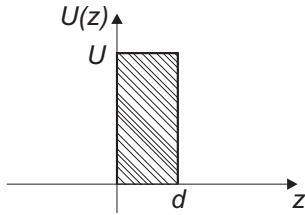
variation of the tip-sample separation which is then presented as a grayscale or color image.

Nowadays, the whole scanning operation and data acquisition is fully computer controlled, which means that scanning parameters like x - y scan speed, bias voltage and current set point are adjusted through computer interfaces. With the arrival of fast computers and field programmable gate arrays even the feedback system has become fully digital, which offers advantages in controlling certain feedback loop parameters, as e.g. the proportional and integral response of the feedback loop or the distance z in hold modes like I - V curves and scanning tunneling spectroscopy (STS) measurements.

2.1.2 Theory of STM

An exact treatment of the tunneling process in STM is virtually impossible, since this would require a detailed description of the quantum mechanical sample and the tip states and their evanescence into the tunneling gap. Especially the description of the tip states is impossible since the exact tip geometry and chemical composition are normally not known. Moreover, it is common knowledge that the tip structure, and hence also the resolution of the STM images obtained, may change during an experiment. Nevertheless, models and theories on different levels of approximation have been developed over the years. An overview of existing theories for the tunneling junction of STM can be found in textbooks [10, 11] or in a review article by Drakova [12].

A one-dimensional tunneling process serves as an elementary model in order to introduce the basic concepts and features of STM imaging. In classical mechanics, an electron with energy E moving in a piecewise constant barrier potential



$$U(z) = \begin{cases} 0 & \text{for } z < 0 \\ U & \text{for } 0 < z < d \\ 0 & \text{for } z > d \end{cases}$$

is described by

$$\frac{p_z^2}{2m} + U(z) = E$$

where m is the electron mass and p_z its momentum. If $E < U$ the electron has a nonzero momentum p_z in regions outside the barrier, but it cannot penetrate the barrier and is therefore confined to one side of the barrier. In quantum mechanics, however, the state of the same electron is described by a probability wavefunction $\psi(z)$, which satisfies the stationary Schrödinger equation

$$-\frac{\hbar^2}{2m} \frac{d^2}{dz^2} \psi(z) + U(z)\psi(z) = E\psi(z), \quad (2.1)$$

with the reduced Planck constant \hbar . In the classically allowed region $z < 0$,

$$\psi(z) = \psi(0)e^{+ikz} \quad (2.2)$$

with the wave vector $k = \sqrt{2mE}/\hbar$ is the solution of Eq. 2.1 for an electron moving in positive z direction. In the classically forbidden region—the barrier—the solution is

$$\psi(z) = \psi(0)e^{-\kappa z} \quad (2.3)$$

with the decay constant

$$\kappa = \frac{\sqrt{2m(U - E)}}{\hbar}. \quad (2.4)$$

Hence, the probability w of observing an electron at the end of the barrier at $z = d$ is

$$w \propto |\psi(d)|^2 = |\psi(0)|^2 \exp(-2\kappa d). \quad (2.5)$$

If we consider this potential as a model for the metal-vacuum-metal junction of our tunneling gap, the work function Φ of the metals plays the role of the potential barrier height U , assuming the work functions to be equal and neglecting the thermal excitation of the electrons in the metal. The electron can tunnel from one metal to the other and *vice versa*. However, without a bias voltage, there is no net tunneling current. By applying a bias voltage V , a net tunneling current occurs and we end up with a model like Fig. 2.1.

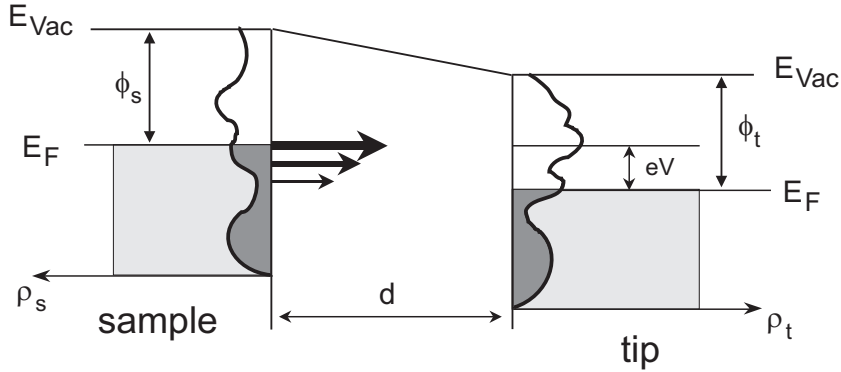


Figure 2.1: Schematic 1-dimensional diagram of a tip-sample junction. In this representation a negative bias U has been applied to the sample and electrons therefore tunnel from occupied sample states into unoccupied tip states. The size of the horizontal arrows indicates the different transmission coefficients (and therefore of the tunneling probabilities) for electrons of different energies.

Assuming $eV \ll \Phi$, an electron in the n th sample state ψ_n with the energy E_n between the Fermi level E_F and $E_F - eV$ has the probability

$$w \propto |\psi_n(d)|^2 = |\psi_n(0)|^2 \exp(-2\sqrt{2m\Phi}d/\hbar) \quad (2.6)$$

to be present at the tip surface. $\psi_n(0)$ is the value of the n th sample state at the sample surface and a summation over the total number of those states within the energy interval eV leads to the tunneling current

$$I \propto \sum_{E_n=E_F-eV}^{E_F} |\psi_n(d)|^2. \quad (2.7)$$

If eV is small enough so that the density of electronic states does not vary significantly within $[E_F - eV, E_F]$, the sum in Eq. 2.7 can be conveniently expressed with the *local density of states* (LDOS) $\rho_s(z=0, E_F)$ of the sample at the Fermi level E_F

$$I \propto V \rho_s(z=d, E_F) = V \rho_s(z=0, E_F) \exp(-2\sqrt{2m\Phi}d/\hbar) \quad (2.8)$$

According to the previous equation, a constant-current STM image at low bias voltages is a contour map of the sample surface LDOS at the Fermi energy and at the position of the tip

2 Experimental Methods

surface. Additionally the equation includes the exponential decay of the tunneling current I with increasing tip-sample distance d which, as already stated, is the main reason for the high resolution in STM.

As early as 1961, Bardeen [13] introduced a way to calculate the tunneling current between two planar metal plates in the context of metal-insulator-metal tunneling junctions. Instead of trying to solve the Schrödinger equation of the whole system, Bardeen considered two separate subsystems with a semi-infinite insulator first. He obtained the electronic wavefunctions for the separate subsystems by solving their stationary Schrödinger equations individually and then calculated the rate of the electron transfer by using time-dependent perturbation theory. This concept was first applied to the tip-sample geometry by Tersoff and Hamann in the so-called *s-wave approximation* [14, 15].

From Fermi's golden rule [16] the probability w of an electron to tunnel between a sample state ψ_s and a tip state ψ_t is

$$w = \frac{2\pi}{\hbar} |M|^2 \delta(E_{\psi_s} - E_{\psi_t}) \quad (2.9)$$

if only elastic tunneling is considered, i.e. only tunneling between states with the same energy $E_{\psi_s} = E_{\psi_t}$. As Bardeen already showed, the amplitude of electron transfer, or the tunneling matrix element M , is determined by the overlap of the surface wavefunctions of the two subsystems at a separation surface S_0 as

$$M = \frac{\hbar^2}{2m} \int_{S_0} (\psi_s^* \nabla \psi_t - \psi_t \nabla \psi_s^*) dS. \quad (2.10)$$

If a bias voltage V is applied the tunneling current is calculated by summing over all the possible states

$$I = \frac{2\pi e}{\hbar} \int_{-\infty}^{\infty} [f(E - eV) - f(E)] \rho_s(E - eV) \rho_t(E) |M|^2 dE \quad (2.11)$$

where $f(E) = [1 + \exp((E - eV)/k_B T)]^{-1}$ is the Fermi distribution function of the thermally excited electrons at temperature T and ρ_s and ρ_t are the densities of states (DOS) of the two electrodes. k_B is the Boltzmann constant. If $k_B T$ is smaller than the energy required in the measurement, the Fermi distribution can be approximated by a step function and the tunneling current becomes

$$I = \frac{2\pi e}{\hbar} \int_0^{eV} \rho_s(E_F - eV + E) \rho_t(E_F + E) |M|^2 dE. \quad (2.12)$$

If the tunneling matrix element $|M|$ does not change appreciably in the interval of interest, the tunneling current is determined by a convolution of the DOS of the two electrodes

$$I \propto \int_0^{eV} \rho_s(E_F - eV + E) \rho_t(E_F + E) dE. \quad (2.13)$$

Clearly, the electronic structure of the two participating electrodes is incorporated in the formula in a symmetric way and the two parts are interchangeable. If one DOS, e.g. the tip DOS, can be regarded as constant, the current scales with the DOS of the sample. Tersoff and Hamann now faced the difficulty of evaluating the tunneling matrix element M of Eq. 2.10

by approximating the tip as a protruded piece of metal, with spherical symmetry and radius R modeled in the jellium model. Among the different solutions of this quantum mechanical problem Tersoff and Hamann showed that for most problems the main contribution comes from the s-wave solution, lending their approach the name s-wave approximation. This solution yields the tunneling matrix element

$$M \propto \kappa R e^{\kappa R} \psi_s(r_0), \quad (2.14)$$

where $\kappa = \sqrt{2m\phi}/\hbar$ is the minimum inverse decay length for the wave functions in the vacuum gap with an effective local barrier height ϕ . $\psi_s(r_0)$ is the sample wavefunction at the center r_0 of the tip apex. Proceeding on all the assumptions made up to this point [17], this approach leads to the following current dependency for small bias voltages

$$I \propto V \frac{R^2}{\kappa^2} e^{2\kappa R} \rho_t(E_F) \rho_s(E_F, r_0), \quad (2.15)$$

with ρ_t being the DOS of the tip. As can be seen in equation 2.8 the tunneling current is proportional to the sample LDOS ρ_s at the Fermi level at the center of the tip apex. The exponential dependence on the gap distance d is again reproduced here, due to the exponential decay of the sample wavefunctions into the vacuum gap: $\rho_s = \sum_s |\psi_s(r_0)|^2 \delta(E_{\psi_s} - E_F)$ and $|\psi_s(r_0)|^2 \propto \exp(-2\kappa(R + d))$.

By assuming an s-wave for the tip, the approach of Tersoff and Hamann relates the tunneling current only to properties of the sample alone. A constant current image therefore reflects the contour of constant LDOS at the Fermi level of the sample. For metals the LDOS at the Fermi level almost coincides with the total electron density, because of the faster exponential decay of the energetically deeper lying occupied states. These surface charge density contours exhibit the periodicity of the surface atoms and directly reflect the surface topology.

2.1.3 Imaging Adsorbates with STM

One has to be aware that the simple topographic interpretation of constant current STM images of metal substrates does not hold true for single atom or molecular adsorbates¹. This is for instance seen for the imaging of O on Pt(111) [18, 19], which is counterintuitively imaged as a depression with respect to the bare metal surface. Another example is the imaging of CO on Cu(211) [20, 21] where CO can appear as both a depression or a protrusion, depending on the proximity of neighbouring molecules and the modification of the tip by adsorbed CO. Even in the case of large organic molecules with an extended π -electron system, the height interpretation is not necessarily straight forward as the example of porphyrin molecules shows [22]. These molecules are imaged as depressions or protrusions depending on their substituents.

Before the first successful STM images of organic molecules were reported [23–26], it was debated whether molecular imaging should be possible at all. The doubts stem from the fact that most organic molecules have a rather large energy gap between their highest occupied molecular orbital (HOMO) and their lowest unoccupied molecular orbital (LUMO). Since the tunneling current is proportional to the LDOS at the Fermi energy according to Tersoff and Hamann, the molecules should not be visible at low bias voltages. Adsorbate states far from

¹Even for clean metal surfaces the topographic interpretation is sometimes too simplistic, if one thinks of features like surface state images at step edges

the Fermi level may, however, influence the LDOS at the Fermi level, since they interact with a continuum of states in the band structure of the solid [27, 28] and a new band around the adsorbate state emerges, which in turn affects the LDOS at the Fermi energy.

The clarifying work in the interpretation of the contrast mechanism of simple atomic adsorbates was performed by Lang [29, 30], who proved that these adsorbates are imaged as protrusions or depressions, depending on whether they add or deplete the electron density at the Fermi energy. Therefore even insulating atoms can be seen in STM as discussed by Eigler and coworkers for the case of Xe physisorbed on Ni(110) [31]. As a rule of thumb elemental adsorbates with increasing electronegativity or decreasing polarizability tend to be imaged as depressions [32, 33].

When it comes to simulating an STM image the knowledge of the electronic structure of the complete system, namely substrate, adsorbate and tip, is a prerequisite. On top of all the approximations coming from the choice of the ab initio method used to calculate the electronic structure and the inherent problem of an unknown tip, another level of approximations comes into play depending on the method used to actually simulate the tunneling current. The most popular class of methods relies on perturbation theory, following Bardeen and Tersoff and Hamann, as sketched above. Another famous approach for this purpose is the electron scattering quantum chemical (ESQC) method by Sautet and Joachim [34], which describes the interaction of sample and tip in a scattering theory formalism. The basic idea is to consider the tunnel gap as a two-dimensional defect inserted between two semi-infinite periodic systems. The tunnel event is then viewed as a scattering process: incoming electrons, for example from the bulk of the sample, scatter from the tunneling junction and have a small probability to penetrate into the tip, and a large one to be reflected towards the bulk. Maybe the most prominent example of a successful application of the ESQC method is for the adsorption of benzene on Pt(111), where three different experimental imaging modes could be successfully modelled as corresponding to three different adsorption sites [35, 36]. A recent review by Sautet [37] discusses STM contrast mechanisms and the theoretical approaches taken to reproduce STM images of adsorbates in detail.

2.1.4 Diffusion of Adsorbates

Since migration or diffusion of adsorbates plays an essential role in various physical and chemical aspects of surface science, as e.g. in crystal and film growth, in the formation of self-assemblies or in heterogeneous catalysis, increasing interest has been devoted to the understanding of surface diffusion dynamics. Two major focus points can be distinguished. On the one hand, there are experiments where the mobility of an adsorbate is observed with respect to the whole ensemble of adsorbates as e.g. the oxidation of Cu(110) [38] or the nucleation of sub-phthalocyanine molecules on Ag(111) [39]. On the other hand, a number of direct observations of single adsorbate diffusion are known [40–43]. From these studies the so-called tracer diffusion coefficient D can be determined. D is directly connected to the random motion of the diffusing particles and is defined as

$$D = \lim_{t \rightarrow \infty} \frac{\langle (\Delta x)^2 \rangle}{2mt}, \quad (2.16)$$

where $(\Delta x)^2$ is the mean-square displacement in the time interval t and m is the dimensionality of the diffusive process. Most of the studies to date focus on ad-atoms or small molecules,

where diffusion can be theoretically described as random-walk, i.e. a result of uncorrelated displacements or hops between adjacent minima of the corrugated potential energy hypersurface, representing the adsorbate-substrate interaction. The frequency with which those hops are observed is the so called hopping rate h . The mean-squared displacement $(\Delta x)^2$ in the time interval t is then given by

$$\langle(\Delta x)^2\rangle = \lambda^2 h t, \quad (2.17)$$

with the jump length λ . Equation 2.16 can therefore be expressed as

$$D = \frac{1}{2m} \lambda^2 h. \quad (2.18)$$

The temperature dependence of the hopping rate h normally follows the exponential law

$$h = h_0 e^{-\frac{E_D}{k_B T}}, \quad (2.19)$$

which is the so-called Arrhenius form [44]. Herein h_0 is the attempt frequency or pre-exponential factor, E_D the activation energy or barrier height of the corrugated potential and k_B is the Boltzmann constant. If hopping rates at several temperatures are available, the Arrhenius parameters can be extracted from an Arrhenius plot, which plots $\ln h$ versus $1/k_B T$ and therefore should show a linear function if the assumptions for equation 2.19 are valid. For more details and further reading on the lattice gas model described above the readers is referred to [45, 46] and an excellent review by Gomer [47]. The lattice gas model is appealing because it is simple and many of its assumptions have been found to agree well with the direct experimental observation.

However, for larger organic molecules, similar studies on the surface mobility are rare [48] and very often restricted to (110) oriented surfaces. This excellent experimental simplification reduces the diffusion process to a 1D problem and does typically not allow for rotational degrees of freedom. Generally, the energy dissipation to the substrate is rather weak for large organic molecules and therefore the assumption of uncorrelated hops is too simplistic: Once a molecule has reached the energy of the diffusion barrier, it does not stop in the adjacent energy minimum but has a high chance to move on for several minima. By including these so called long jumps the lattice gas model has been slightly modified [49].

The more complex the adsorbate-substrate system gets, the more difficult it is to gain information on the precise adsorption sites. The typically increased structural flexibility of larger molecules and the complex surface adsorbate interaction involving several surface atoms together, yield a very complex energy potential well for the adsorption process. On strongly interacting surfaces this complexity is further enhanced by conformational changes, which are likely to occur in the molecule [4], and by structural changes of the surface itself in the course of the adsorption process. As a consequence, the lattice gas model will probably not be able to describe the diffusion process adequately for such a case, as will become apparent in chapter 3.

2.2 Low Energy Electron Diffraction

Another important surface science technique used in this thesis is low energy electron diffraction (LEED) which was developed by Germer [50] some thirty years after his original experiment [51],

2 Experimental Methods

where he and Davisson proved the wave particle dualism for electrons. The LEED technique relies on the fact that by tuning the energy of an electron beam, its de Broglie wavelength

$$\lambda = \frac{h}{p} = \frac{h}{\sqrt{2mE}} \quad (2.20)$$

can be chosen to be in the same range as the typical interatomic spacings—say $\sim 1 \text{ \AA}$ —of typical crystalline structures studied in surface science. This is why electron waves of an appropriate wave length impinging on a crystal get diffracted at the periodic lattice of the crystal and give valuable information about the crystal symmetry and structure.

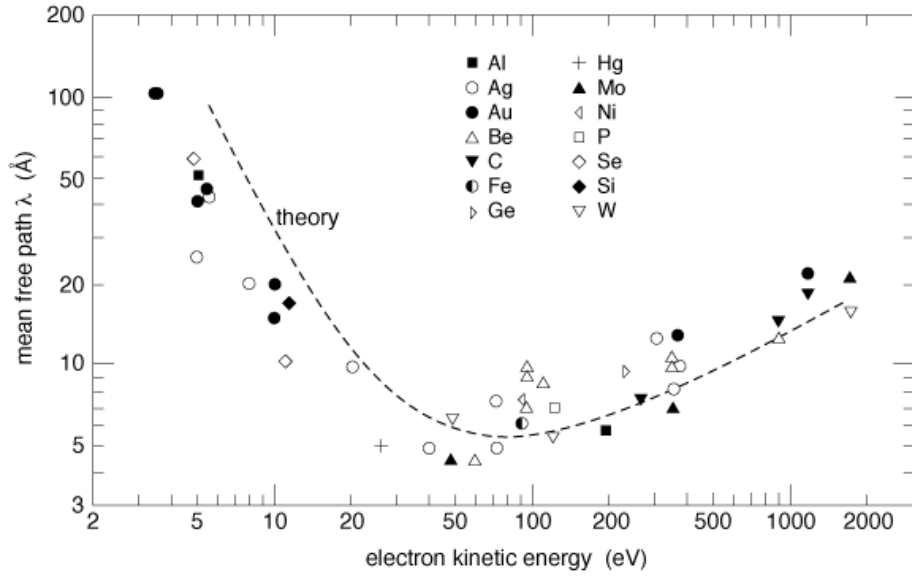


Figure 2.2: Universal curve of electron mean free path. Adapted from ref. [45] and references therein.

The electron energy needed for such de Broglie wavelengths lies in the range of 10–200 eV. Therefore is close to the energy corresponding to the minimum of the universal curve of electron mean free path in solids (Fig. 2.2). This fortunate coincidence is the reason for an extraordinary surface sensitivity of the diffraction process of LEED, since a small electron mean free path is tantamount to a small penetration depth and small escape depth for the elastically backscattered electrons. Therefore, only the very few topmost layers of the crystal are involved in the diffraction process, leading to a pronounced surface sensitivity, which is crucial in order to observe phenomena such as surface reconstructions or self-assemblies of submonolayer ultra-thin adsorbate films. Without exaggeration it can be stated that nowadays LEED is the most important diffraction technique to investigate crystal structures of surfaces due to its simple UHV lab based setup and its ease of use. Other surface sensitive diffraction techniques like Grazing Incidence X-ray Diffraction (GIXD), which bear similar information of the in-plane crystallographic structure, involve the use of high flux x-ray sources of synchrotron radiation facilities and are not that widely used.

By means of an electron gun, electrons with a certain - but variable - energy between a few to some hundreds of eV are accelerated perpendicular towards the sample surface. The backscattered and diffracted electrons are then energy filtered by a retarding field between

two grids and collected on a fluorescent screen placed on the same side of the sample as the electron gun. Energy filtering has to be applied, because only electrons which undergo an elastic scattering process (about 1% of the total yield) give rise to sharp diffraction peaks. The inelastically scattered electrons would give rise to a blur background due to the additional momentum transfer received from the inelastic scattering process and are therefore filtered out by the retarding field.

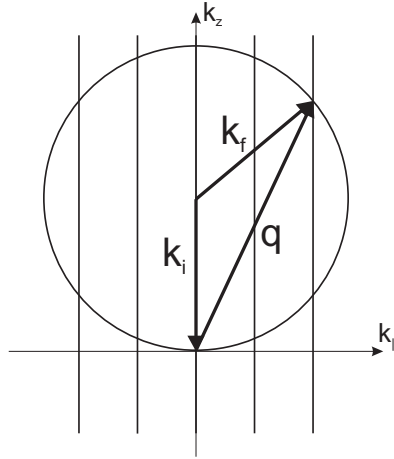


Figure 2.3: Ewald construction in a reciprocal space representation of a 2D lattice. The surface rods of the lattice (vertical lines) always cut through the Ewald sphere, if the magnitude of the initial wave vector k_i (sphere radius) is large enough, i.e. if the wave length of the impinging electrons is small enough.

The LEED pattern observed on the fluorescent screen is a projection of the reciprocal space of the sample surface. In order to recall the complete idea and features of reciprocal space one should refer to common solid state physics books such as [52, 53], but mathematically reciprocal space is the Fourier transformation of real space. Since LEED probes the atomic structure of the first few layers, the real space sample surface can be described by a 2D lattice of 1st (and 2nd) layer atomic positions in xy -direction and a δ -function in z direction perpendicular to the surface. The Fourier transformation of such a structure is a 2D grid of so called *surface rods*, because the transformation of a δ -function is an infinitely dense constant function. Now, the concept of the Ewald construction to find the Laue conditions for constructive interference in x-ray scattering [54] can also be applied to find the LEED spots of a given surface at a certain initial electron energy. As marked in Fig. 2.3, the magnitude of the initial wave vector k_i defines the radius of the Ewald sphere in reciprocal space. The final wave vector k_f after *elastic* scattering is of the same magnitude and therefore has to lie somewhere on the sphere surface. Constructive interference—maximum of intensity on the fluorescent screen—is achieved if the scattering vector $q = k_f - k_i$ coincides with a reciprocal lattice vector or rather a point in reciprocal space. For 3D reciprocal lattices this condition is only fulfilled for selected energies and scattering geometries since the respective lattice point has to lie exactly on the Ewald sphere surface. Due to the infinite density of lattice points along the surface rods, this condition is always fulfilled in the case of LEED, as long as the initial wave vector has a magnitude large enough to reach a rod. For each energy the 2D lattice rods cut through the sphere surface and the pattern on the screen can be used to conclude on the crystallographic structure of the surface [55].

Note that this simple kinematic LEED analysis does not bear on the question of the arrangement of atoms within a surface unit cell. In contrast to X-rays, electrons which are used for LEED interact strongly with matter and therefore undergo multiple scattering within the first layers. The correct intensity profiles can consequently only be calculated from dynamic scattering theory which includes these multiple scattering events. Nevertheless, a lot of applications of LEED as a powerful surface science technique have been published. For an overview of examples see the book of Van Hove et al. [56] or the review paper from Heinz [57].

2.3 X-ray and UV Photoelectron Spectroscopy

Today, photoelectron spectroscopy (PES) is a well established surface science technique to probe for chemical and electronic sample properties. Like LEED, photoelectron spectroscopy is a non-local method since it provides information integrated over a macroscopic area of the sample. PES is based on the phenomenon of photoemission: electromagnetic radiation impinging on a surface liberates electrons from the surface. Photoemission was first detected by Hertz [58] in 1887. In the following years his experiments have been refined and in 1905 Einstein was able to explain the systematics of photoemission by invoking the famous quantum nature of light [59].

Due to the fundamental law of energy conservation, a photoelectron emitted from a surface on which the electromagnetic radiation with angular frequency ω impinges has a kinetic energy

$$E_{\text{kin}} = \hbar\omega - E_{\text{b}} - \Phi, \quad (2.21)$$

where E_{b} is the binding energy of the emitted electron (measured relatively to the Fermi energy) and Φ is the work function of the sample. Since in PES the impinging radiation is monochromatic, its photon energy $\hbar\omega$ is constant. Therefore the binding energy of each emitted electron can be measured by determining its kinetic energy in an electrostatic energy analyser. Nowadays, most electron energy analysers are so-called spherical deflection analysers (SDA), which consist of two concentric hemispheres with a constant potential applied in between. The electrons entering the SDA get deflected by the electrostatic field and only the electrons with a certain energy, the so-called *pass energy* can pass through the whole analyser and get detected by an electron detector at the analyser exit slit. By sweeping a retarding field in front of the analyser, the number of electrons N at each kinetic energy E_{kin} is measured. $N(E_{\text{kin}})$ is called the photoelectron spectrum of the sample and is the convolution of the density of states (DOS) of the occupied states of the sample, the intrinsic line shape of the radiation, an analyser acceptance function and other secondary electron effects. The task of extracting certain aspects of the DOS from the spectrum is not a trivial one and subject to elaborated data treatment techniques.

Different sources of electromagnetic radiation with different energy and different intrinsic line width can be used to excite the electrons of the sample. Depending on the energy, usually two excitation regimes are distinguished. In X-ray photoelectron spectroscopy (XPS), the energy of the incident photons exceeds ≈ 100 eV, whereas for ultraviolet photoelectron spectroscopy (UPS) the photon energy is below ≈ 100 eV. Although conceptually equal, XPS and UPS offer different kinds of information about the sample.

With the high energy range of XPS the energetically deep lying core levels of atoms can be probed, which allows the determination of the chemical composition of the sample. For example, the intensity of the different peaks can be compared in order to determine the sample

stoichiometry at the surface. Moreover, for the investigation of molecules and solids, one is usually not interested in the absolute binding energy of the core level, but in the slight change in binding energy between different chemical forms of the same element. This difference is called *chemical shift* and is due to the influence of the valence electron configuration on the core level states. Therefore, measurements of the chemical shift are an excellent method to distinguish different chemical forms of the same element, for which the term ESCA (Electron Spectroscopy for Chemical Analysis) was coined [60]. ESCA allows for studies how adsorbates interact with the substrate or helps to distinguish different chemical species.

UPS, applying photons in the lower energy range, is used to probe the DOS of the valence band and states which are close to the Fermi edge. Those states are the direct finger print of molecular interactions or the interaction between the adsorbate and the surface involved in a system.

Common to UPS and XPS as well as to LEED is the high surface sensitivity due to the short electron mean free path. Although the electromagnetic radiation of UPS and especially of XPS can penetrate deep (several μm or more) into the sample, the maximum escape depth of the electrons is given by the electron mean free path. Since the electron mean free path depends on the electron energy (as already stated in Fig. 2.2 of the LEED section), UPS provides information about the first 1–2 atomic layers and XPS about the first 3–8 layers.

2.4 The UHV System

To study reactions on surfaces at the atomic or molecular scale, the ability to precisely control the environment and condition of the surface at hand is an absolute prerequisite. From this perspective, ultra high vacuum (UHV) is a fundamental tool which allows one to keep the surfaces free of contaminants. Almost all experiments presented in this PhD thesis were therefore performed in the Nanolab of the Institute of Physics at the University of Basel. The Nanolab instrumentation consists of a very versatile multi-chamber UHV system connecting six separate chambers. Each chamber is equipped with its own pumping system combining turbo, ion getter and titanium sublimation pumps. The chambers are interconnected with normally closed gate valves and the base pressure is in the high 10^{-11} mbar or the low 10^{-10} mbar range depending on the chamber. A fast entry air lock allows to insert samples and STM tips as well as transferable evaporation sources into the system without breaking the vacuum of the main system. The samples, mainly metal single crystals, are mounted on modified VG stubs and can be transferred through the whole UHV system.

The standard course of an experiment starts with the preparation and cleaning of the metallic substrates with standard sputtering and annealing cycles [61]. Then the sample is transferred into the so-called molecule chamber which has been set up during the PhD thesis of S. Berner [62], where the molecules under investigation are evaporated onto the samples *via* sublimation from resistively heated crucibles. A quartzcrystal micro balance setup allows the repeatable preparation of molecular layers down to 0.05 ML. Additionally, the molecule chamber provides a facility to deposit molecules from their liquid phase by means of a liquid deposition system which will be described in more detail later on.

The prime instrument employed in the Nanolab and therefore the prime surface science technique used in this thesis is the STM. The microscope is a home-built STM, which is operating at room temperature and is described in more detail in the PhD thesis of T.M. Schaub [63]. In order to obtain a good signal to noise ratio, the STM is equipped with a

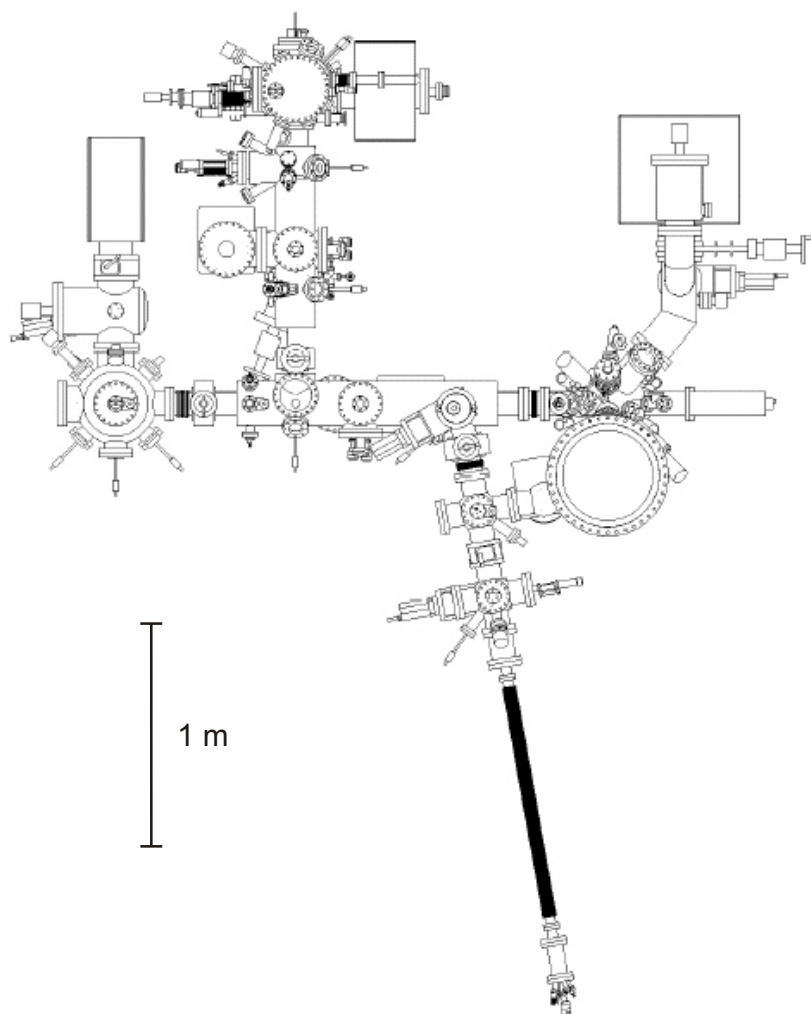


Figure 2.4: Plan (topview) of the Nanolab multi-chamber system. Drawing by A. Heuri.

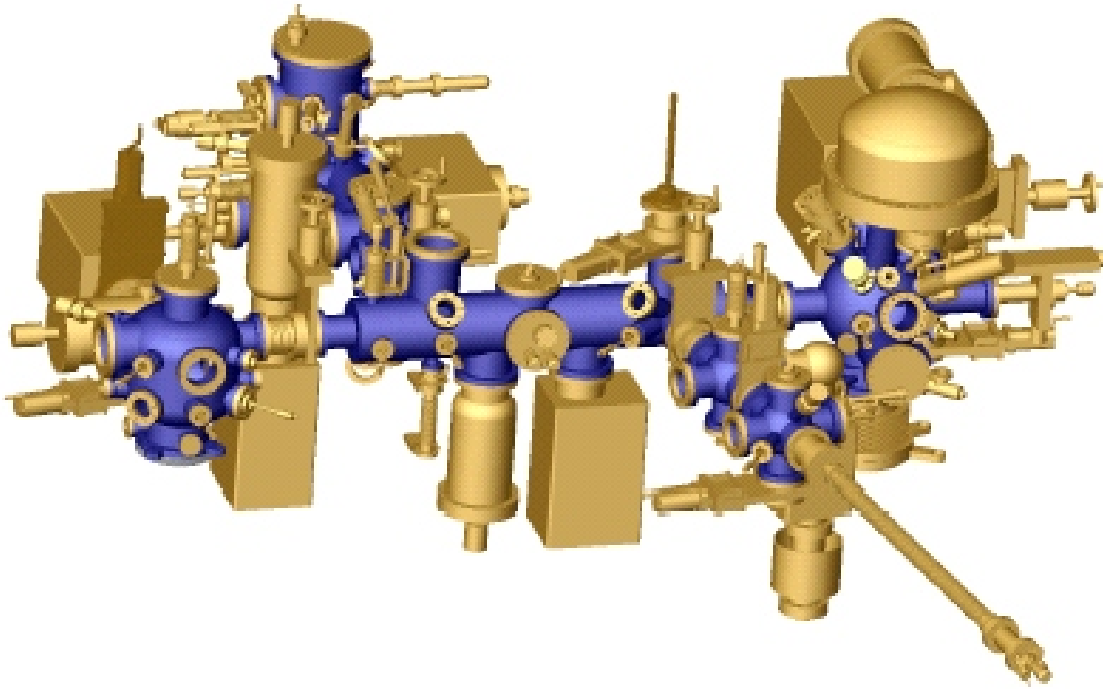


Figure 2.5: 3D view of the Nanolab. Drawing by A. Heuri.

pre-amplifier which is situated very close to the tip-sample junction on the STM stage inside the UHV. The STM is mounted on a multistage vibration isolation and damping system, whose main component is an Eddy-current damping system consisting of a ring of copper plates moving in magnetic fields. When working with larger molecular adsorbates, an important feature of our STM is the possibility to exchange the scanning tips without breaking the vacuum. As scanning tips electrochemically etched tungsten tips are used after in-situ cleaning by electron bombardment. The bias voltage is applied to the sample. Therefore a negative bias voltage corresponds to tunneling from occupied sample states to unoccupied tip states.

The other major analysis tool in the Nanolab is the ESCA (electron spectroscopy for chemical analysis) chamber equipped with the commercial ESCALAB MKII system from Thermo Vacuum Generators (Hastings, United Kingdom) for UPS, XPS and Auger electron spectroscopy. The X-ray source is a non-monochromatized Mg/Al twin anode, whose main excitation lines Mg K_{α} and Al K_{α} are at the photon energies of 1235.6 eV and 1486.6 eV, respectively. For UPS a non-monochromatized He gas discharge source is used, whose main line is the HeI $_{\alpha}$ (21.2 eV), besides the lamp can be optimized to run with HeII $_{\alpha}$ (40.8 eV) excitation energy. The electron analyzer is a spherical deflection analyser of 150° equipped with three channeltron electron detectors.

Additionally, a rear view LEED system is attached to the main transfer chamber in order to be able to quickly check the crystallographic structure of sample surfaces. Further details about the Nanolab system can be found in the following references [62–67].

2.5 Liquid Deposition System

As some of the molecules used during the investigation of the catalytic Pt-Cinchona system are liquid at room temperature, they consequently have a much higher vapour pressure than other molecules normally sublimated from their solid powder phase. Therefore, a liquid deposition system was constructed as schematically shown in Fig. 2.6.

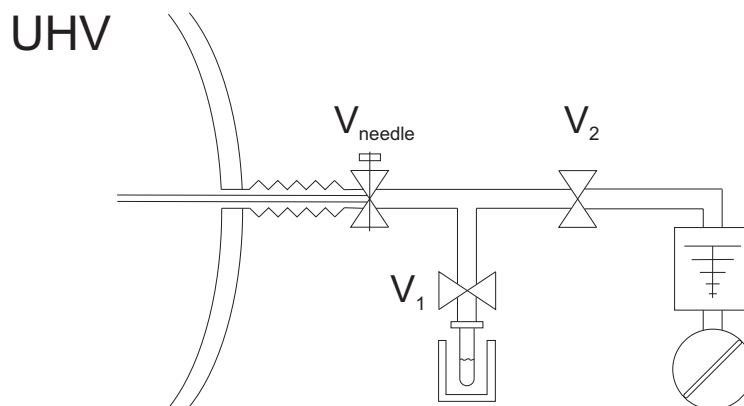


Figure 2.6: Valve scheme of the liquid deposition system.

The liquid molecules are kept in a transparent glass tube reservoir in order to have visual feedback during cleaning of the molecules and to check for signs of deterioration of the material. The first step when working with liquid molecules is the cleaning procedure.

For solid powders one repeatedly heats the crucible with the material slowly up to a temperature slightly below the sublimation temperature of the molecules. This step is known as degassing and one assumes that most of the impurities and solvents involved in the synthesis or preparation of the compound are more volatile than the compound itself. Therefore the pressure burst due to the sublimation of the volatile impurities will get smaller as their fraction in the crucible gets smaller. After the pressure in the chamber has recovered and the crucible is heated to the sublimation temperature of the desired molecules the rate of molecules impinging on a quartz micro balance can be measured. For liquid molecules, so-called freeze-pump-thaw cycles are applied. With the valve V_1 still closed, the liquid is frozen by filling the bath around the reservoir with liquid nitrogen. When the liquid is frozen completely, valve V_1 is slowly opened and the vapour pressure remaining above the frozen solid is pumped by the turbo pump *via* the open valve V_2 . Under the same assumption as for the solid case, the fraction of impurities and solvents in this residual vapour phase should be higher than that of the molecule itself. After closing valve V_1 again, the liquid nitrogen bath is removed and the molecules start to thaw. First, the more volatile impurities start to evaporate and small bubbles can be seen through the glass tube. After the material in the reservoir is completely thawed, the cycle starts again and one therefore reduces the fraction of impurities step by step.

After the last cleaning step the valve V_2 towards the turbo pump is closed and the vapour phase above the liquid is expanded into the volume in front of the needle valve V_{needle} . During deposition this needle valve is opened until the cold cathode pressure gauge inside the UHV chamber shows a desired pressure value and the total deposition amount is regulated by the deposition time.

2.6 Single Crystal Electron Bombardment Station

Normally, the metal single crystals used in the Nanolab are mounted on stubs with an internal filament included in the lower cylindrical part of the stub. By applying a current of about 3–4 A to the internal filament the stubs can be resistively heated to a maximum temperature of 1100 K. Unfortunately, this temperature is not high enough to conveniently anneal the platinum and palladium single crystals. For this reason, an electron bombardment station has been designed and improved several times.

For electron bombardment three different electric contact leads are needed. Two contacts are used for running a current through a filament in order to emit electrons. The third contact is then used to accelerate those electrons towards the target which has to be heated. With this method higher heating power can be achieved and by changing the positive potential of the target, the heating power can be regulated easily. The main difficulty of electron bombardment in sample preparation and especially of our VG stub system, is the fact that the single crystals have to be heated from the back side in order to keep the surface under investigation atomically flat and clean. This means the electron emitting filament has to be setup on the back side of the sample normally inaccessible due to sample holder.

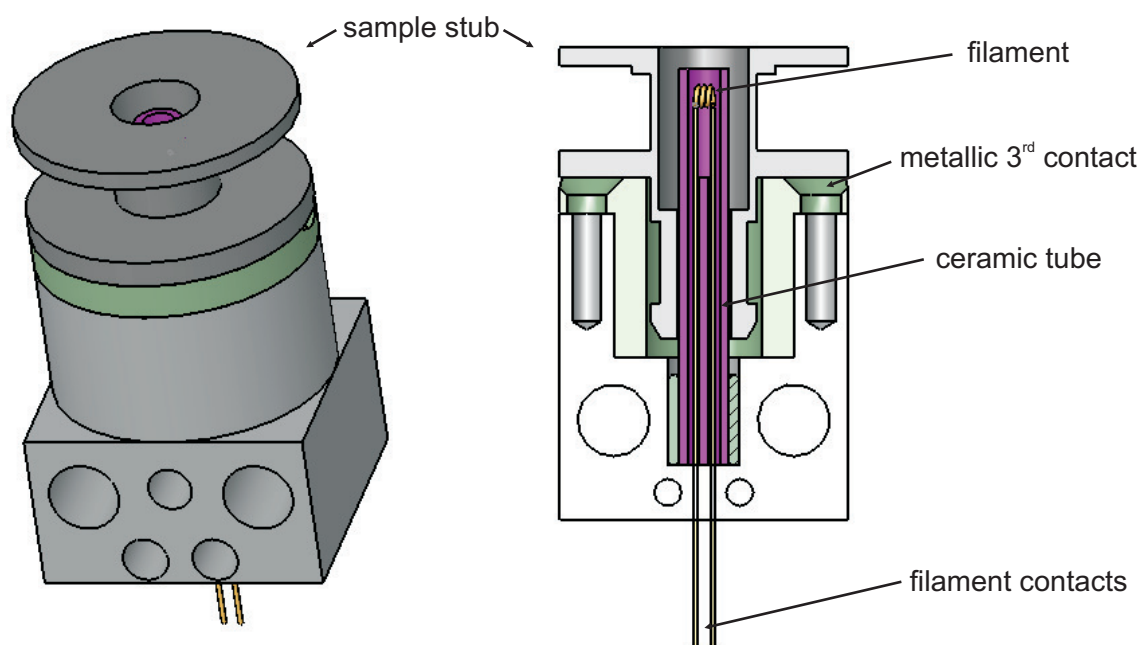


Figure 2.7: Single crystal electron bombardment station for the preparation of the Pt and Pd single crystals. Drawing by A. Heuri.

In our system this was achieved by incorporating the filament with its two contacts in a small ceramic tube on a fixed macor station as shown in Fig. 2.7. The small ceramic tube fits into the hollow stub, which acts as the third contact through which the electrons are accelerated towards the mounted single crystal. During the course of this thesis several improvements have been made to prevent the filament and the ceramic tube from changing its position inside the tiny setup under thermal load.

3 The Pt-Cinchona Alkaloid System

The following chapter deals with the STM results on the cinchona alkaloid modified platinum system. This catalytic system is a prominent example of heterogeneous enantioselective catalysis, where the outcome of a reaction of a pro-chiral reactant is biased in a way that preferably a product with only one handedness or chirality is produced.

3.1 Motivation

The investigation of complex organic molecules on metal surfaces by scanning probe microscopies (SPM) has become a topic of great interest in recent years. Most of the research has been centered on the study of molecular self assembly on rather unreactive metal surfaces (for a few selected examples see [68–70]). Much less is known about the behaviour and the surface chemistry of molecules on more reactive surfaces as used in catalysis. Particularly challenging in this context is the study of the behaviour of chiral molecules adsorbed on catalytically active metal surfaces due to their relevance to heterogeneous asymmetric catalysis.

Since most of the biologically active molecules are chiral, chirality is a fundamental principle of nature with a huge impact on life itself. Especially amino acids, which are the building blocks of proteins, are chiral and therefore a lot of reactions of living organisms are aware of chirality due to the chirality of enzymes involved. Interestingly, most amino acids show the same kind of chirality and one speaks of the homochirality of biological systems, whose origin is still subject to highly philosophical debates [71, 72]. Due to this natural relevance of chirality, the chirality of manmade pharmaceuticals also has to be considered when a new compound is brought into market. A very famous example is the pharmaceutical Contergan, whose one stereomer showed effectiveness against insomnia, but the other stereomer caused the well known severe problems of deformity of children when taken during pregnancy. If there is one good point of the Contergan case, it is the fact that nowadays a strong set of rules is assuring that all possible stereomers of a compound are tested in extensive studies or that it has to be made sure that the pharmaceutical drug is optically pure, meaning only the physiologically effective stereomer is included.

In the end, the choice is up to pharmaceutical industries to either produce both enantiomers and try to separate them later, which is difficult since all the physical properties despite the optical activity are identical. Or to produce only one stereomer of the compound by employing—among other methods—enantioselective/asymmetric catalysis. In this context, asymmetric catalysis is unique in the sense that with a small amount of an optically active catalyst a large quantity of a chiral compound can be produced. This circumstance was also dubbed chiral multiplication and the importance and topicality of research in this field was shown by the Nobel prize 2001 being awarded to Sharpless, Noyori and Knowles [73–75] for their advances on homogeneous asymmetric catalysis. For production purposes, however, the use of heterogeneous catalysis is preferred since it offers inherent practical advantages connected to separation, reuse and stability of the catalyst and it furthermore affords the

opportunity for continuous process operation [76]. Unfortunately, the variety and application ranges of heterogeneous asymmetric catalysts are yet rather limited compared to the number of highly selective homogeneous asymmetric catalysts known to date.

In the past, various strategies have been pursued in the development of heterogeneous asymmetric catalysis, but only two of them show synthetic potential [77]: The immobilization of enantioselective homogeneous transition metal complexes on a surface and the modification of active metal surfaces by an adsorbed chiral modifier, among which the enantioselective hydrogenation of α -functionalized ketones over cinchona alkaloid modified platinum is a prominent example [78, 79].

Today, three catalytic systems based on chiral modification of active metal surfaces are known, which afford an enantiomeric excess of more than 90% for the hydrogenation of certain substrates. These are the Ni-tartaric acid, Pt-cinchona, and Pd-cinchona systems [80–86]. The Ni-tartaric acid system has been investigated by means of STM by Raval and coworkers [87–89]. The platinum cinchona system has been addressed recently with a combined STM and photoelectron-spectroscopy approach by the group of Lambert [90, 91]. However, this work mainly focused on the oligomerization of the reactant methyl pyruvate (MP) and the adsorption of the simplified modifier (S)-1-(1-naphthyl)ethylamine, which is not an actual chiral modifier but a precursor to a chiral modifier for enantioselective hydrogenation on Pt [92]. For cinchonidine, the most powerful modifier, only STM studies on Cu(111) in solution exist so far [93, 94]. Therein, Xu et al. observed the formation of ordered cinchona adlayers with a (4×4) symmetry. Until now, their results could not be reproduced by others [95] and are highly questioned due to the fact that the (4×4) symmetry could already be observed for the pure solvent. Additionally, copper is not active for this type of reaction and therefore the observed assembly of cinchonidine is unlikely to be relevant for the catalytic system.

The aim of the present study was to gain direct insight in the molecular processes which occur during adsorption of the modifiers and reactants of the enantioselective Pt-cinchona and Pd-cinchona systems. Different adsorption modes were identified and a change in adsorption geometry upon addition of hydrogen was followed. The findings are discussed in the light of catalytic, theoretical and spectroscopic data available for this system. Additionally the time-resolved STM investigations uncovered details of the dynamic surface processes, which would be hardly accessible by other surface analytical techniques.

3.2 Definitions of Stereochemistry

This section briefly introduces the basic principles of stereochemistry and explains some conventions used when dealing with the chirality or handedness of molecules [96, 97].

Structures of the same *constitution*, i.e. the same atoms and the same sequence of bonding in between them, can still differ in their spatial arrangement, their so-called *configuration*. For example four different substituents around a sp^3 hybridized C atom can be arranged in two non-superimposable configurations. All such isomers of a given structure are called *stereoisomers* and the structure itself is called *chiral*. The atom or the center where chirality occurs is known as a chiral atom or chiral center. Since molecules in general may possess more than one chiral center, more than two stereoisomers may exist (for a molecule with N chiral centers up to 2^N stereoisomers). Pairs of stereoisomers that are exact mirror images of each other, i.e. each chiral center has the opposite chirality of the other isomer, are called *enantiomers*. All other pairs are named *diastereomers*.

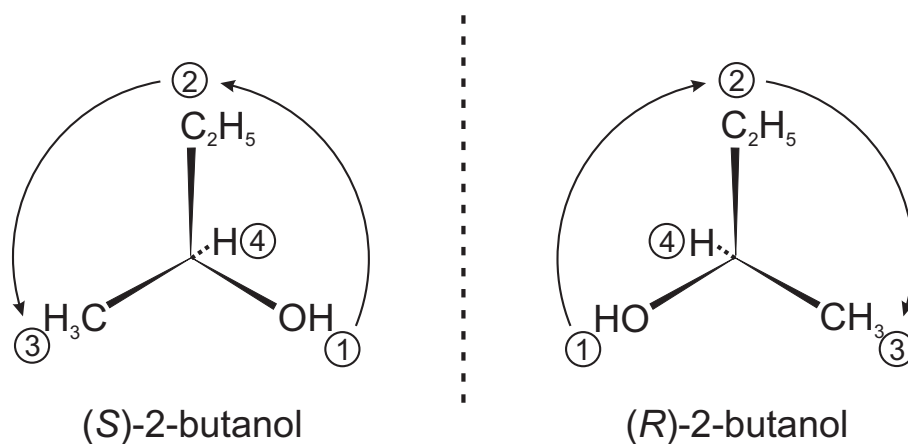


Figure 3.1: The Cahn-Ingold-Prelog convention exemplified for 2-butanol. The substituents of the chiral C atom in the center are marked from highest priority (1) to lowest priority (4), according to decreasing atomic numbers. In the case of equal elements (2 and 3) the atomic numbers or weights of the follow-up substituents are compared until the priority of all substituents has been established. Then the lowest priority, in our case the hydrogen atom, is placed behind the chiral center. If the remaining substituents decrease in priority clockwise or anticlockwise, the configuration is assigned R (rectus = *lat.* right) or S (sinister = *lat.* left), respectively. Figure adopted from [46].

In an achiral environment enantiomers show identical physical and chemical properties with the exception that they are optically active. That is, they rotate the plane of polarized light in opposite directions. Samples with equal amounts of the two enantiomers are called racemic mixtures and show a zero net rotation. Since it is possible to separate enantiomers of chiral compounds, samples with different enantiomeric compositions can be obtained. Samples containing only one enantiomer are known as enantiomerically pure or homochiral.

An important value for mixtures of two enantiomers is the *enantiomeric excess* (ee), which is defined by

$$ee[\%] = 100 \frac{n_{\text{major}} - n_{\text{minor}}}{n_{\text{major}} + n_{\text{minor}}}$$

where n is the molar concentration.

An important convention used to distinguish between the two different chiralities is the Cahn-Ingold-Prelog (CIP) convention, which will be explained and used in the following. To determine the chirality of a chiral center unambiguously, one first has to establish some sort of ordering rules for the different substituents around a chiral center. The CIP convention is based on the rule that the substituent atoms are assigned decreasing priority in the order of decreasing atomic numbers. If, in a first step, there are two or more atoms of the same element, the next attached atoms of those are compared in a second step until a complete ordered set has been found. This process of hierarchical assignment of substituents can in certain cases be very complicated and puzzling. For details and refined rules the reader is referred to the original papers [98, 99]. The molecule is now viewed in an orientation which places the lowest-priority substituent behind the chiral center as shown in Fig. 3.1. If the remaining three substituents decrease in priority clockwise or counterclockwise, the configuration is assigned the descriptor R (rectus = *lat.* right) or S (sinister = *lat.* left), respectively.

3.3 The Cinchona Alkaloid Modified Catalysis on Platinum Metals

In 1979, Orito et al. discovered the Pt-cinchona alkaloid system for the enantioselective hydrogenation of α -ketoesters to α -hydroxy esters [100–103]. In the following years a lot of knowledge has been gathered on this catalytic system, which helped to broaden the scope of the reaction and to some extent understand the mechanisms involved in the enantiodifferentiating step (for recent reviews see [78, 104–106]). Depending on the choice of reactants, the cinchona alkaloid modifiers and the solvents used, a wide range of reaction conditions is needed in order to achieve high enantioselectivity. This fact already reflects the enormous complexity of the interactions (reactant-substrate, modifier-substrate, reactant-modifier, solvent related) involved in a real world catalytic system.

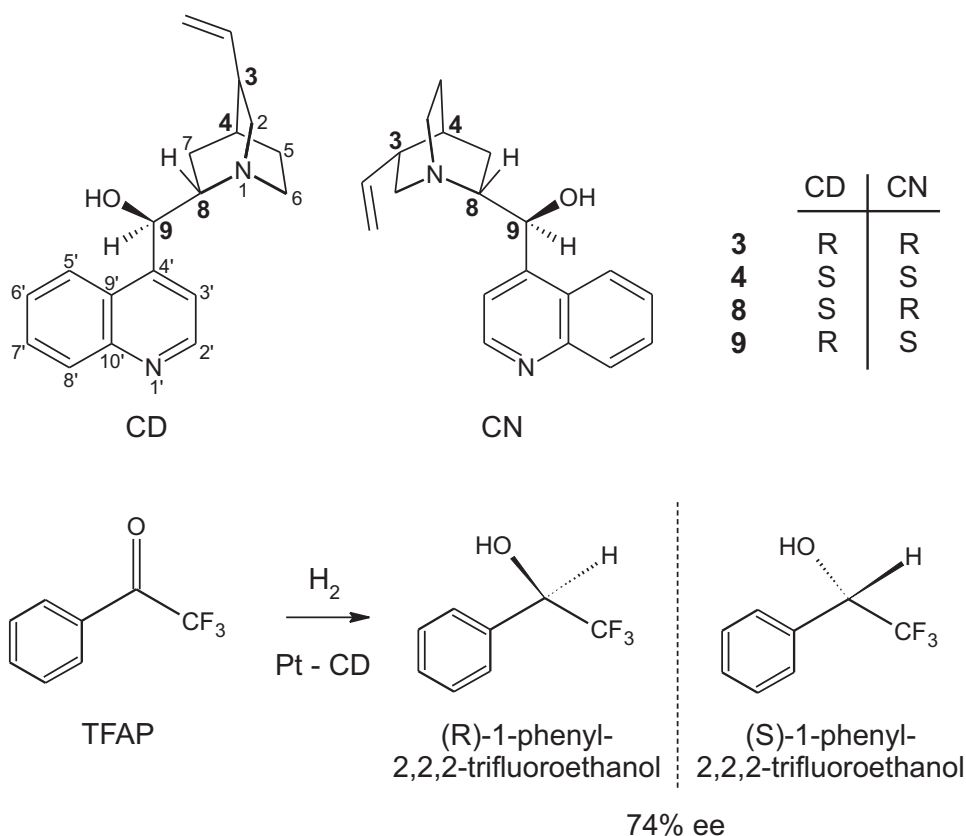


Figure 3.2: Structure of natural cinchona alkaloid modifiers (top) used for the enantioselective hydrogenation of a trifluoromethyl ketone over chirally modified platinum (bottom).

The modifier around which the Pt-cinchona system is centered is a natural product called cinchonidine (CD), which is shown in Fig. 3.2. The molecule mainly consists of two moieties, a flat quinoline π -system (designated with primed numbers in Fig. 3.2) and a rather bulky quinuclidine moiety (normal numbers). Important to note is the rotational flexibility of the quinuclidine moiety around the C8–C9 and the C9–C4' bonds of the molecule, which will become important later on during the discussion of the STM results. Another well known modifier used during this study is cinchonine (CN), the quasi-enantiomer of cinchonidine, which leads to the opposite enantioselectivity of the catalytic system.

In 1994, Baiker and coworkers proposed a 1 : 1 interaction model of the modifier and the reactant of a Pt-cinchona system based on quantum chemical calculations and the existing experimental knowledge [107]. The theoretical model assumed that enantiodifferentiation can be traced down to the different stabilities of the diastereomeric complexes formed between the cinchonidine modifier anchored to the Pt catalyst surface and the reactant adsorbed in its two enantiofacial forms (via *re*- and *si*-faces), leading to S and R products, respectively, upon hydrogenation. According to these models the reactants interact with the quinuclidine nitrogen atom via a N—H···O hydrogen bond or a N···H—O hydrogen bond, depending on the solvent used. This intermolecular interaction and the steric repulsion exerted by the quinoline group is thought to cause the preferential adsorption of the reactant on one enantioface. It was also shown in a combined theoretical and experimental study of different α -substituted ketones as reactants [108], that it is even possible to explain the rate acceleration effect—in presence of the modifier the reaction is 2–100 times faster compared to the unmodified reaction [109–111]—with this 1 : 1 hydrogen bond model. The study uncovered a relationship between the keto carbonyl orbital energy and the hydrogenation rate. It has then been shown that within the 1 : 1 model the more stabilized diastereomeric complex also undergoes a larger stabilization of the keto carbonyl orbitals, leading to a lowering of the activation barrier and therefore to faster kinetics. An interesting side effect of this rate acceleration is that the typical ratio between reactant and modifier is 150–1800, which nicely demonstrates the efficient chiral multiplication of the Pt-cinchona system.

Despite the wealth of knowledge and detailed models, so far mostly indirect pictures exist of the Pt-cinchona system and our STM study was aimed at filling this gap. The close collaboration with Prof. Baiker at the ETH Zurich and the fact that Dr. Matthias von Arx, my supervisor who initiated this project, has already worked on the chemical aspects of this reaction, provided a lot of knowledge about the system and assured that the interpretation of our measurements were consistent with former findings.

From the various reactions known for the cinchona alkaloid over platinum system, our studies concentrated on the enantioselective hydrogenation of an α -ketone, namely 2,2,2-trifluoroacetophenone (TFAP), over cinchonidine (CD) or cinchonine (CN) modified Pt(111) and Pd(111) single crystal model surfaces.

As shown in figure 3.2 the hydrogenation of TFAP over platinum produces (R)- and (S)-1-phenyl-2,2,2-trifluoroethanol. By the addition of the cinchona modifier enantioselectivity is introduced and the outcome of the reaction is biased. For ideal reaction conditions an remarkable ee of 74% towards the (R)-enantiomer of the chiral alcohol product is achieved in the case of the CD modifier. Among the different reactants known for the cinchona alkaloid system we choose to use TFAP as the reactant for our studies. First, because an electron withdrawing group (such as CF₃) in alpha-position to the ketocarbonyl group being reduced is a necessity for effective enantioselectivity [112]. The second reason to choose TFAP is the exceptional high electronegativity of fluor, which often leads to distinct features or signals in various kinds of physical investigations.

During the PhD thesis of M. von Arx, the reactions normally have been carried out in different solutions, at room-temperature and under approximately ambient pressures [79]. Therefore, all the statements made in this thesis have to be considered on the background of the well known *pressure gap*, which describes the pressure gap between real world catalytic systems and their investigation under UHV conditions. Nevertheless, the role of the surface hydrogen concentration is a key kinetic parameter of the reaction conditions used, since hydrogen is a compulsory ingredient of enantioselective hydrogenation reactions. For example

α -ketoester hydrogenation [113, 114], as hydrogenation of most reactants, is performed at high hydrogen partial pressure in order to improve enantiodifferentiation. We therefore not only investigated the adsorption behaviour of CD, CN and TFAP in the absence of hydrogen, but also in the presence of a hydrogen background pressure in the UHV chamber. We thereby can vary the surface hydrogen concentration and track its influence on the adsorption behaviour of the modifier and reactants involved.

3.4 Sample Preparation

As already explained in the introduction of this chapter, one of the difficulties of this project was to prepare and maintain clean (111) oriented single crystal surfaces of the very reactive platinum and palladium metals, since their high reactivity comes hand in hand with a high sticking coefficient.

The Pt(111) and Pd(111) single crystals (Mateck GmbH, Germany) were cleaned by repeated cycles of Ar⁺ ion sputtering (800 eV, 4×10^{-7} mbar, 30 min) and subsequent annealing [61] at about 700 °C for 10–12 minutes via electron impact heating on the single crystal electron bombardment station described in section 2.6. If a new crystal was introduced into the chamber, in the beginning annealing temperatures were kept much lower (≈ 300 °C) and were slowly increased during the following cycles until the targeted value was achieved. This procedure prevents superficial defects (caused by contaminants) from growing into the crystal and destroying the perfect crystal structure, which has been crosschecked at times by LEED.

To remove any organic impurities, every second annealing cycle was carried out in the presence of a standing oxygen pressure of 5×10^{-8} mbar regulated via a leak valve. After closing the oxygen leak valve to the chamber the samples were flashed at a slightly higher temperature (800 °C) for about 2 minutes in order to reduce the oxygen coverage on the surface before the next sputter cycle. The last annealing cycle always has to be carried out without oxygen. Thus a sample preparation normally included an even number of sputter-anneal cycles. Typically four cycles a day lead to atomically clean and flat surfaces. STM images displayed terraces with a width of about 50–500 nm.

Due to the high sticking coefficient for most residual gas components on both Pd and especially Pt, special care had to be taken to make sure that the base pressure in the system remained in the low 10^{-10} mbar range once the clean samples were prepared. The separate molecule deposition chamber was used to sublime the CD and CN molecules from home-built resistively heated tantalum crucibles at temperatures of about 100 °C. The substrate was kept at room temperature during the deposition process and a cooling trap attached to the chamber was cooled with liquid nitrogen in order to keep residual gas pressure at a minimum. Before and after deposition, a home-built quartz microbalance was used to monitor the evaporation rate at the position where the sample was placed during deposition.

Being liquid at room temperature, TFAP was deposited via the liquid deposition system described in the experimental methods section 2.5. The vapour phase above a liquid reservoir of TFAP was expanded via a leak valve (and a capillary) into the UHV chamber. The exposure was determined by measuring the pressure increase during the inlet with a cold cathode pressure gauge.

All samples were characterised using a home-built STM operating at room temperature. All STM images and time-lapse imaging sequences were obtained in constant-current mode by recording the vertical tip movement of an etched and electron bombarded tungsten tip. The

standing hydrogen pressure of 10^{-10} to 10^{-6} mbar in the STM chamber was controlled in situ by a leak valve.

The average displacement data shown were obtained from time-lapse series of STM images, where scan range and scan speed were set appropriately in order to be able to distinguish the appearance and mobility of different molecular species while still imaging a statistically meaningful number of molecules in one frame. In some cases this was a difficult task, because good topographical imaging of individual molecules typically depends on the tip quality and the scanning condition used. Therefore the image quality can vary during experiments due to tip changes or due to different scan speeds. High resolution images have been achieved at slow scan speeds (≈ 200 nm/s), while higher scan speeds (≈ 600 nm/s) were required in order to track very mobile molecules.

The image sequences were evaluated by tracking 10 to 15 single molecules by using the particle analysis tool in the STM image processing software WSXM (Nanotec Electronica S.L.). The resulting xy-paths were drift corrected and their integral displacement was calculated by summing up the distances measured from frame to frame, fully neglecting the fact that due to the limited scan speed the molecules may have moved a longer distance in between the images as a result of a back-and-forth movement. Therefore, all mobilities given here are lower limits. By taking the slopes of such integral displacements and averaging over the whole population of a surface species, we obtained the average displacement and its standard deviation in nanometers per minute.

3.5 CD on Pt(111)

Figures 3.3 and 3.4 show STM images of less than half a monolayer of CD deposited on Pt(111). In contrast to earlier findings of CD on Cu(111) [93, 94], the individual molecules are randomly distributed on the surface. The random distribution was observed on all samples investigated and independent of the coverage. This indicates a low mobility and a rather small molecule-molecule interaction compared to the molecule-substrate interaction. On the reactive substrate surfaces of platinum and palladium, hence the formation of molecular assemblies both on terraces and at step edges is prevented. This is well in line with the findings of ab initio calculations [115], which predict a strong chemisorption of CD on Pt involving several Pt atoms.

The dimensions of the CD molecules appear somewhat bigger than anticipated from the molecular structure, which is typical when imaging individual protrusions with STM. One has to bear in mind that, when imaging an adsorbate with a high aspect ratio one does not image the electronic structure of the adsorbate itself, but rather its convolution with the electronic structure (shape) of the tip. Therefore individual adsorbates normally appear larger than they are or appear in an ordered assembly [116].

From the appearance of the individual molecules, two distinct forms can be identified. Some examples are highlighted by red and green circles in Figure 3.4 and hence are denominated red and green species in the following.

The appearance of the red species in Fig. 3.4 is characterized by three lobes forming sort of a triangular arrangement. The apparent height of these molecules is around 1.5 to 2 Å on the full width (1.5 nm) and length (2 nm) of these molecules (see Fig. 3.3 a and b). The green species has a more random shape distribution, but are identified by a characteristic apparent height profile ranging from -1 to 3 Å (Fig. 3.3 c and d). This characteristic profile

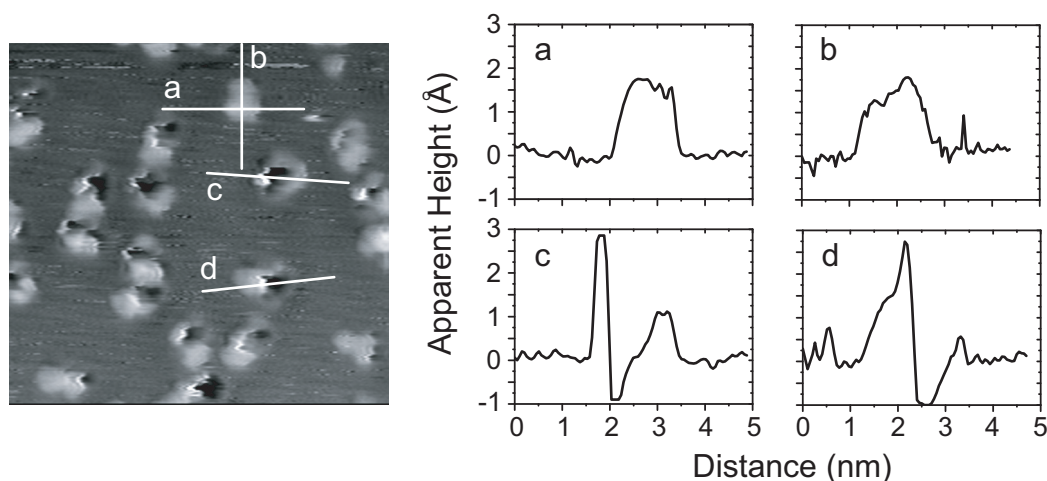


Figure 3.3: STM apparent height image of cinchonidine (CD) on Pt(111). The image corresponds to the area marked in Fig. 3.4 a. Image size: $12 \times 12 \text{ nm}^2$, $I = 50 \text{ pA}$, $U = 1.0 \text{ V}$. The profiles a to d on the right correspond to the line cuts shown in the image.

shows that the tip moves both, further away from the surface and very close to the surface for each scanline contributing to the image of these molecules.

Based on this observation and the arguments given below, the green species is tentatively assigned as CD molecules adsorbed via the quinoline ring in the so-called flat adsorption mode (see Fig. 3.5 a). In such an adsorption mode the molecule is anchored strongly to the surface via the quinoline π -system, while the quinuclidine part points away from the surface. Therefore, the rotational flexibility of the quinuclidine moiety around the C8–C9 and the C9–C4' bonds of the molecule described above (see Fig. 3.5a and 3.2) is not blocked by any interaction with the metal surface, and the molecule can adopt different conformations (e.g. closed(1), closed(2), open(3), closed(4) etc., for a detailed naming convention see [118, 119]). This identification can explain the observed apparent height profiles in Fig. 3.3 c and d and the overall appearance of these species: Each time the STM tip approaches a flatly adsorbed CD molecule it starts to interact with the molecule and withdraws in order to maintain a constant current. The CD molecule is affected by the interaction force induced by the tip and as a result changes its conformation by rotation of the quinuclidine moiety around the flexible bonds, lowering the interaction with the tip. This process occurs on a timescale much faster than the feedback loop settings, which control the tip movement. The feedback loop, trying to keep a constant current, lowers the tip towards the surface and as a consequence, the tip exhibits the pronounced sharp directional change shown in Fig. 3.3 c and d. If the speed of the feedback is decreased (increased), the effect persists, while the characteristic profile is slightly rounded (sharpened). In other words, the appearance of the flatly adsorbed, green species as imaged by STM is partly the result of the feedback system responding to the fast change in conformation of the molecule. Due to this conformational flexibility, the shape of the molecules is intrinsically not very well defined, nonetheless their appearance is very distinct (Figures 3.3 and 3.4).

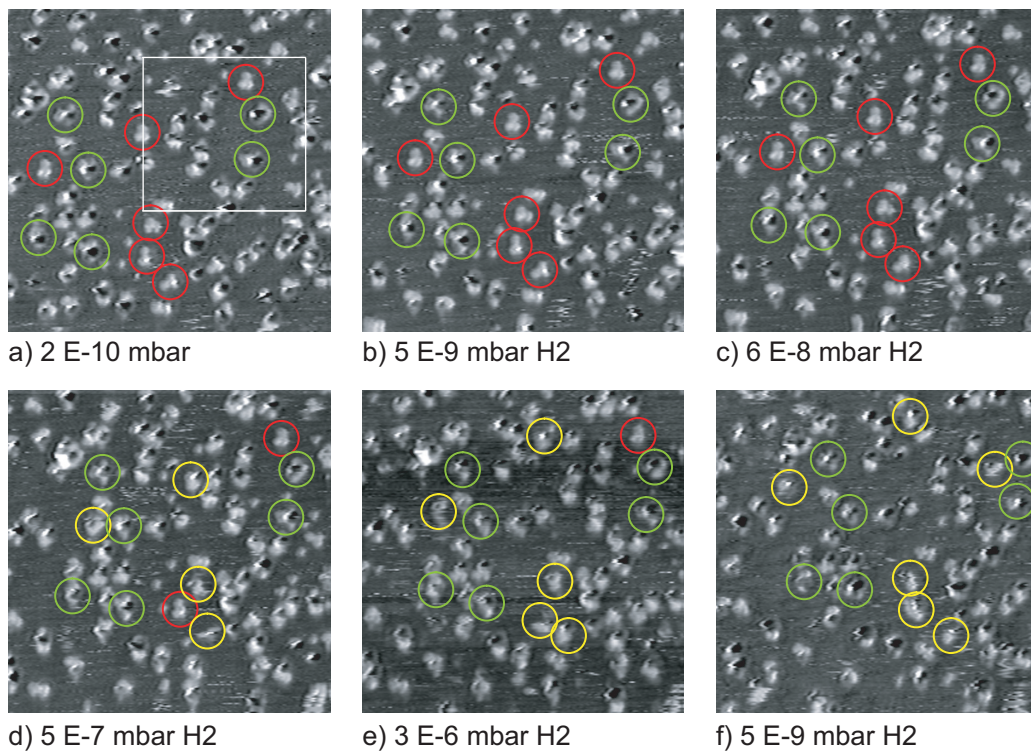


Figure 3.4: STM sequence showing the evolution of the molecular adsorbates while increasing the hydrogen pressure in the chamber from 2×10^{-10} to 3×10^{-6} mbar. The selected molecules marked in red, green and yellow represent different adsorption modes of CD on Pt(111). The red species flips to a different adsorption mode (yellow) at elevated hydrogen pressure. The images selected correspond to the images number 2, 8, 12, 17, 22 and 36 of a sequence of 40 images in total. All images were obtained in constant-current mode by recording the vertical tip movement and have been taken at a rate of 52 s per image. The full sequence is available as movie in the supporting material of our paper [117]. The area marked in white corresponds to the area shown in Fig. 3.3. Image size: $25 \times 25 \text{ nm}^2$, $I = 50 \text{ pA}$, $U = 1.0 \text{ V}$

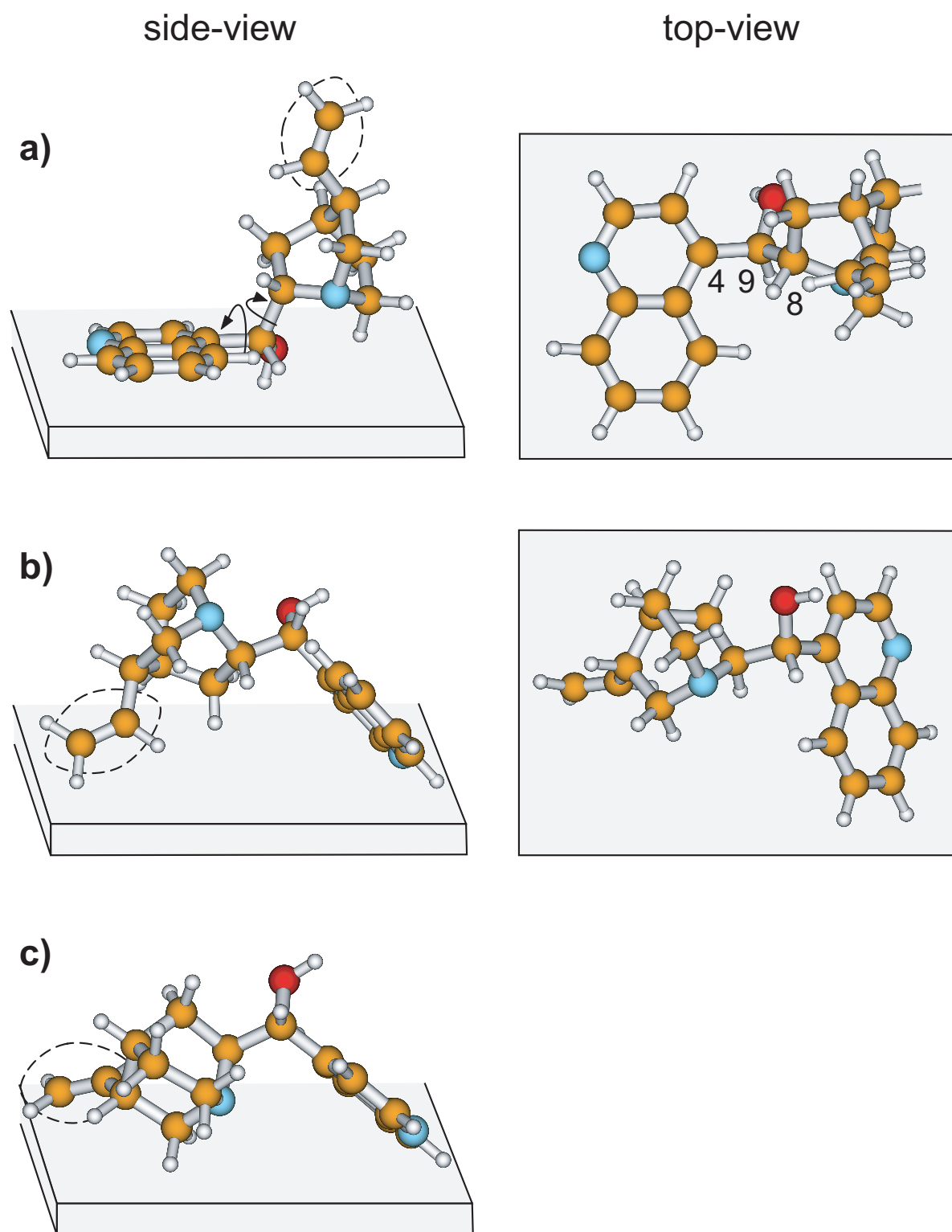


Figure 3.5: Schematic top- and sideview of CD on a Pt surface. The CD structures are optimized open(3) (a and b) and closed(1) (c) structures, respectively. Molecules with the given conformation are drawn in proximity to a schematic metal surface. a) represents the flat adsorption mode of CD (green species) while b) and c) represent two variations of the tilted upside-down adsorption mode (red species). The terminal C=C-double bond is marked by a dashed line

The absence of such a characteristic effect in the imaging of the red species not only leads to a more uniform appearance of the molecules, but implies that no such conformational switching takes place. As a consequence this CD species must interact differently with the metal surface and adopt another adsorption geometry compared to the green species described before. More insight into the possible adsorption geometry of the red species was gained by the time-resolved observation of the CD molecules during a stepwise increase of the hydrogen background pressure in the STM chamber (Fig. 3.4 a–f and Fig. 3.6).

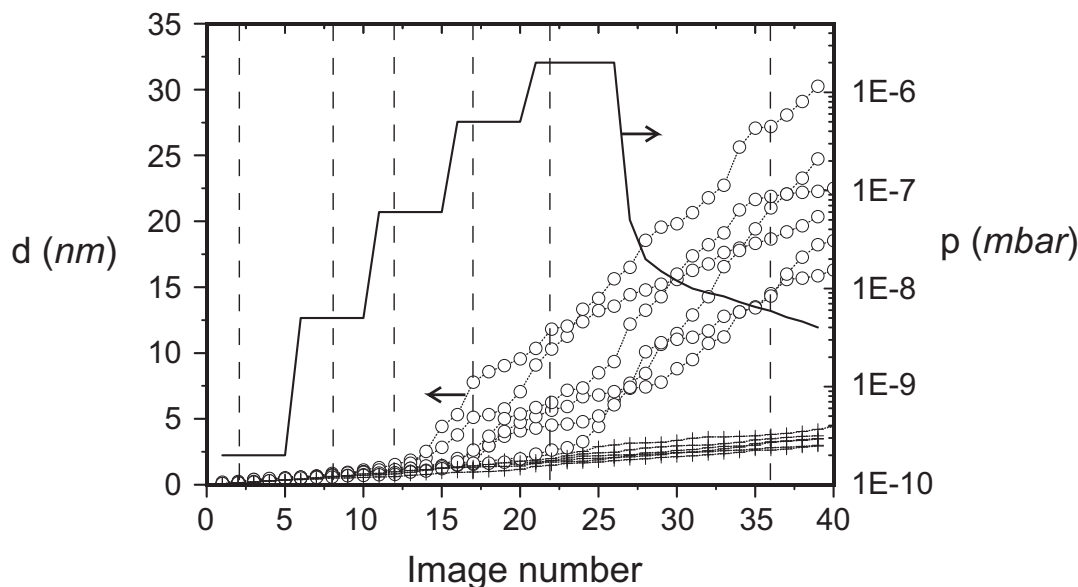


Figure 3.6: Effect of the hydrogen pressure p on the mobility of the green (crosses) and the red (circles) species during the full sequence of 40 images taken. The integral displacement d of the molecules is displayed versus the image number. The mobility is initiated by the hydrogen-induced transformation of the red into the yellow species and persists when the hydrogen pressure is lowered again. The dashed lines mark the images displayed in Fig. 3.4 a–f.

In the first period (images a–c), all molecules are virtually immobile and stay at their place up to a hydrogen pressure of 6×10^{-8} mbar. Upon further increase in hydrogen pressure, 4 out of 6 molecules of the red species change their appearance (image c and d). These molecules are marked yellow. Similar to our observations with the green species (tentatively assigned as flatly adsorbed molecules), the appearance of these molecules marked in yellow is dominated by a characteristic, sharp profile. Therefore, it is suggested that these CD molecules have changed their adsorption mode in a way which released the quinuclidine part of the molecule from a fixed to a free position. It is important to note that this transformation was induced by the presence of hydrogen on the Pt surface. When no hydrogen was available in the chamber, such a transformation has never been observed. Furthermore, the transformation was irreversible. After closing the leak valve, no back-conversion from the yellow to the red species was observed, as illustrated in image f. The full image sequence consisting of 40 images is available online as movie in the Electronic Supplementary Information of reference [117]. In this movie the changes in adsorption geometry and the surface dynamics of the different species can be seen best, as the static representation by six snapshots (Fig. 3.4) can not adequately illustrate the entire information available.

On the basis of these experiments, we tentatively assign the red species to a tilted upside-down adsorption mode, similar to the one shown in Fig. 3.5 b. In this illustration the open(3) conformer, which is the most stable in gas phase [118], is placed in an upside-down fashion on the schematic Pt surface. Compared to a flat adsorption (Fig. 3.5 a) the adsorption energy is expected to be lower because the interaction between the aromatic moiety and the Pt surface is weakened, if they are not parallel [115, 120]. However, some adsorption energy is gained by the additional interaction of the terminal C=C-double bond and the quinuclidine N atom (Fig. 3.5 b and c), which are brought into close proximity to the Pt surface. Through this additional interaction the position of the quinuclidine moiety is fixed, explaining the lack of the sharp dark-bright feature, which is present for the green species, in the images of the red species. It is well known that with increasing hydrogen pressure the terminal C=C-double bond can undergo hydrogenation [121, 122], which weakens the bonding of this part of the molecule to the surface. Hence, the molecule could flip to an energetically more favourable adsorption mode similar to the flat adsorption mode shown in Fig. 3.5 a.

Despite the similarities between the yellow species and the flatly adsorbed molecules, there is a significant difference between them concerning the surface mobility. It can be seen in Fig. 3.4 d–f (and in the movie) that the yellow species change positions within the image sequence. They have a higher mobility than both the flatly adsorbed as well as the tilted upside-down molecules. The change in mobility concomitant with the flipping of the adsorption mode is shown in Fig. 3.6, where the integral displacement d for each of the six molecules marked in red (later yellow) and green is shown. Note that in addition to the appearance of the molecules in the STM images, the different surface mobilities of the adsorbed species is an additional, very strong argument for the discrimination of different surface species. This increased mobility is further confirmed by these molecule’s appearance in STM: they move slightly under the influence of the tip during the imaging process, which leads to a *jagged* outline. This makes it more difficult to identify a precise adsorption mode of this yellow species. However, we suggest an adsorption mode similar to the flat one depicted in Fig. 3.5 a. The higher mobility may be due to a partial hydrogenation of the aromatic ring system. This partial hydrogenation is known to occur as a side reaction during the catalytic process, weakening the adsorption strength of CD, and decreasing the efficiency of this catalyst system [123, 124]. Interestingly, only those molecules which have been converted from the red into the yellow species exhibit an increased mobility in our experiments. We may thus speculate, that during this transformation, the molecules have a higher activity towards hydrogenation than the green species which we observe to be inert in our experimental sequence.

After these first experiments with this catalytic system, a more refined study was initiated in order to gain more detailed information (Fig. 3.7). Compared to the results of our earlier study [117], the refined analysis method described in section 3.4 allows a more detailed description of the surface diffusion of the different surface species populations. In the new series of STM movies (81.5 seconds/frame), the molecules were tracked individually while the hydrogen pressure in the STM chamber was increased stepwise in larger steps than before from 1×10^{-10} mbar to 2×10^{-6} mbar. Then the mobility was determined by calculating an average displacement for each surface species population and for each hydrogen pressure.

In general, the new results support the conclusions made earlier: two clearly distinct adsorption modes can be identified. They have been assigned as flat (quinoline ring system parallel to the surface, strong interaction with the surface, low mobility) and tilted adsorption modes (quinoline ring system inclined to the metal surface, weaker interaction with the surface,

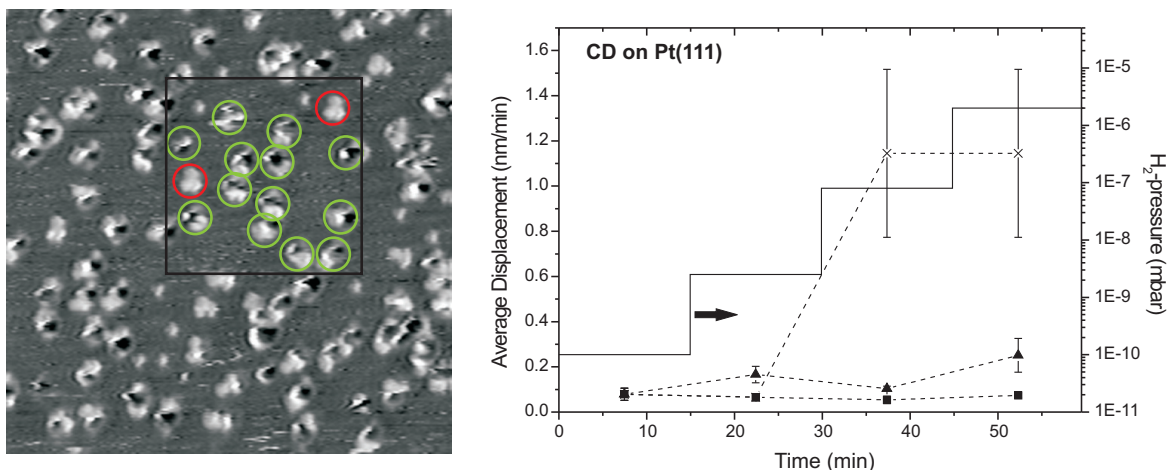


Figure 3.7: (a) STM image of CD (0.27 ML) on Pt(111) at low hydrogen pressure (2×10^{-10} mbar). Inside the marked area, representative for the whole sample, the two different adsorption modes of CD are highlighted. Green circles designate the flatly adsorbed molecules, red circles mark the molecules in the tilted adsorption mode. Image size: $25 \times 25 \text{ nm}^2$, $I = 50 \text{ pA}$, $U = 1.0 \text{ V}$. (b) Average displacement measured for CD on Pt(111). The step function represents the hydrogen pressure used in the time-lapse series. Filled symbols show the mobility of flatly adsorbed molecules, where the triangles stand for free molecules and the squares stand for molecules in clusters. Crosses represent molecules initially adsorbed in a tilted adsorption mode. They flip into a different adsorption mode with significantly increased mobility at elevated hydrogen pressures.

high mobility at elevated hydrogen pressure), respectively, as discussed above and in detail in reference [117].

Furthermore, the new data set revealed more details in the diffusion behaviour. In particular, a difference in the mobility of the flatly adsorbed molecules depending on their local surface density becomes apparent. This surface species population has to be divided into two groups. The molecules which are isolated (no other molecules in close proximity, filled triangles in Fig. 3.7 b) show a slight increase in mobility when increasing the hydrogen pressure, while the molecules in a dimer/cluster configuration (one or more molecules in close vicinity, filled squares in Fig. 3.7 b) stay practically immobile on the timescale and in the pressure range of our experiments. The slight mobility increase of the isolated molecules mainly originates from a wobbling motion of the molecules at elevated pressure: the molecules seem to be pinned to the surface by one part of the molecule while the remaining part wobbles from side to side, typically in angles of 60° . The population of molecules with a tilted adsorption geometry (crosses in Fig. 3.7 b) show the same behaviour as described before. They remain immobile until, at a threshold hydrogen pressure of 8×10^{-8} mbar, the mobility increases instantaneously to a much higher value. At the same time the appearance of these molecules changes significantly. As already stated, this transformation is irreversible as no reversal to the original appearance and mobility is observable upon lowering the hydrogen pressure back to the original value. The new set of data shows that the mobility increases by a factor of 10 or even more in the course of this transformation. The average displacement value for this species has a relatively high variance (see error bars) because of the clustering effect: On its track across the surface, such a molecule—at times—gets in close proximity to other molecules ("cluster"), which leads to a temporal decrease in the mobility. As the time during which

an individual molecule remains inside such "clusters", varies from molecule to molecule, the average displacement value for the whole population varies. Of course this effect depends on the (local) coverage of the sample.

3.6 CN on Pt(111)

CN differs from CD only in the absolute configuration of two of the 4 stereocenters (Fig. 3.2 top). Therefore the two molecules are diastereomers. But due to the mirror plane symmetry of the stereocenters C8 and C9, which are crucial for the stereochemical control of the catalytic reaction, the two molecules are often called *near-* or *quasi-enantiomers*. An example of the topographic image obtained from 0.15 ML CN on Pt(111) is given in Fig. 3.8 a. As observed for CD, the CN molecules are distributed randomly on the surface, which again indicates a low mobility due to a strong molecule-surface interaction. On a first sight, the molecules appear quite different from the images obtained for CD (Fig. 3.7 a). But this is mainly due to tip effects: as already indicated in the section above and in chapter 2 the very apex of an STM tip and scanning conditions may change from experiment to experiment, from sample to sample or even during a scan. This leads to significant differences in the image of objects, in particular of isolated objects (in contrast to regular arrays of objects) such as CD or CN, which are randomly distributed on the substrate surface. Compared to the CD/Pt(111) sample shown in Fig. 3.3, 3.4 and 3.7 a, the tip allowed only lower resolution in the case of the CN/Pt(111) sample shown in Fig. 3.8 a. As a result, the molecules appear a bit broader, and the characteristic up/down feature described above (Section 3.5) for the image of the flatly adsorbed CD molecules is not visible for the CN molecules in Fig. 3.8 a.

Nonetheless, the molecules appearing as a grey oval with a brighter spot, which are marked with a green circle in Fig. 3.8 a, are assigned as flatly adsorbed molecules. This assignment is justified by the following facts: (i) with a lower resolution the flatly adsorbed molecules of CD appear exactly the same; (ii) by changing the scanning speed and/or the response speed of the feedback loop of the tip movement, the image of a flatly adsorbed CD in Fig. 3.7 a changes towards the appearance observed for the CN molecules in Fig. 3.8 a and vice versa; (iii) the diffusion behaviour of these molecules is similar to the one observed for the flatly adsorbed CD molecules but clearly distinct from the molecules marked with red circles in Fig. 3.8 a.

The result of the analysis of the surface diffusion of CN on Pt(111) is given in Fig. 3.8 b. As shown by the step function in Fig. 3.8 b we used approximately the same hydrogen pressures as in the measurements of CD on Pt(111). Again, the two surface species populations can be clearly discriminated concerning their mobility. The flatly adsorbed molecules in dimers or clusters are immobile while the ones which are free show a slight mobility, which is increasing by a factor of $\approx 2-3$ with increasing hydrogen pressure. In this respect, this surface species population differs from the corresponding surface species population of CD (compare filled triangles in Figs. 3.7 b and 3.8 b). The surface species population marked with red circles in Fig. 3.8 b shows the same behaviour as the tilted CD molecules (compare crosses in Figs. 3.7 b and 3.8 b). At a hydrogen pressure of 7.5×10^{-8} mbar, these molecules show an instantaneous increase in their mobility by more than a factor of 10. For this reason we tentatively assign these molecules to a tilted adsorption geometry, in analogy to their CD counterparts. For the last two data points in Fig. 3.8 b no error bars are given, because only few molecules could be tracked. Due to their very high mobility, these molecules get out of view quickly, limiting the precision of the measurement of their average displacement.

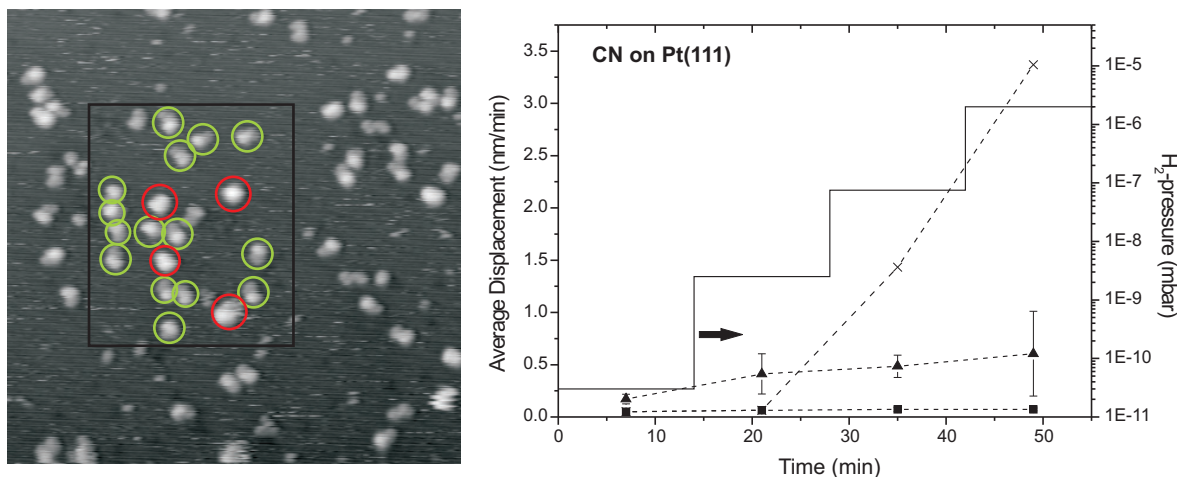


Figure 3.8: (a) STM image of CN (0.15 ML) on Pt(111) at a hydrogen pressure of less than 10^{-10} mbar. As for CD, the two different adsorption modes of CN are highlighted for all molecules inside the marked area. Green circles designate the flatly adsorbed molecules. Red circles mark molecules in the tilted adsorption mode. Image size: $30 \times 30 \text{ nm}^2$, $I = 25 \text{ pA}$, $U = 0.8 \text{ V}$. (b) Average displacement measured for CN on Pt(111). The step function represents the hydrogen pressure used in the time-lapse series. Filled symbols show the mobility of flatly adsorbed molecules, where the triangles stand for free molecules and the squares stand for molecules in clusters. Crosses represent molecules initially adsorbed in a tilted adsorption mode. They swap into a different adsorption mode with significantly increased mobility at elevated hydrogen pressures.

All together this means that the diffusion behaviour of CD and CN on Pt(111) in the presence and absence of hydrogen is very similar. Nevertheless, there is one significant difference: the flatly adsorbed CN molecules which are free (not in a dimer/cluster) show a significantly higher mobility than their CD analogues. It can be excluded, that this difference is due to the different coverages on the samples measured. In both cases our results were measured in the low coverage regime, with a high number of free molecules available. Also the very subjective human perception supports this result when movies of both systems are compared: The overall mobility of CN on Pt appears higher.

3.7 TFAP on Pt(111)

From a first glance on the STM image (Fig. 3.9 a) of about 0.17 ML TFAP deposited on Pt(111) a clear tendency of the molecules to form dimers can be seen. As highlighted by the circle in the lower part of the image, individual TFAP molecules are imaged as a pair of spots: a small dark spot next to a bigger bright spot. Dimers—a typical example is marked by an ellipse in the center—are often imaged as a bone like bright structure having a dark spot on each side. It is interesting to note that similar dimers have already been observed with STM by Lambert and coworkers for ethylpyruvate on Pt(111) [91] As already stated in section 2.1.3 and from various STM investigations it is well known, that electronegative elements like oxygen or fluor are imaged as depressions in STM [32, 33]. Therefore we tentatively assign the dark spot as the image of the carbonyl part of TFAP whereas the larger bright spot is assigned to the benzene ring of the molecule. Not surprisingly, for a smaller molecule

chemisorbed with a smaller π -system and interacting with fewer platinum surface atoms, TFAP has a higher mobility than CD and CN. Therefore one has to scan faster whereby the time per image was reduced to 21.2 seconds. During such STM series it very soon became clear that the TFAP dimers are not stable at room temperature. The TFAP molecules are characterised by a threefold dynamic behaviour. First, there is a dynamic equilibrium between monomers and dimers and second, the dimers can move as an intact entity on the surface. As expected, this mobility is smaller than the mobility of the monomers, which is the third dynamic process on this sample. As a consequence the best way to quantify the mobility of TFAP at different hydrogen pressures was to track individual monomers in time regardless whether they temporarily were a member in a dimer or not.

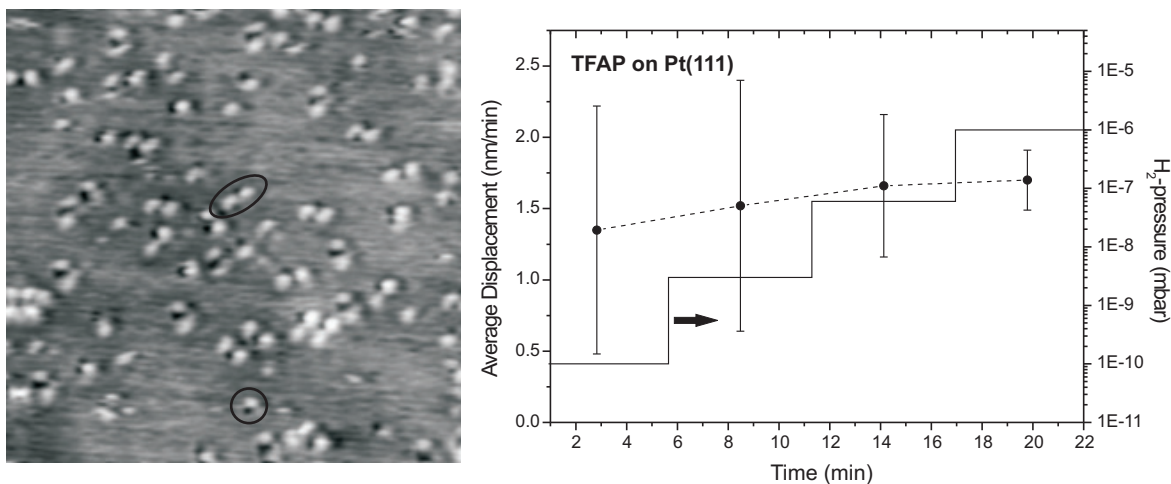


Figure 3.9: (a) STM image of TFAP on Pt(111) at low hydrogen pressure 2.5×10^{-10} mbar. Single TFAPs show as a small dark spot next to a bigger bright protrusion (circle in the lower part of the image). Dimer TFAP look like a bright bone with two dark spots on each side (ellipse in the upper part). Image size: $25 \times 25 \text{ nm}^2$, $I = 20 \text{ pA}$, $U = 0.65 \text{ V}$. (b) Average displacement of TFAP on Pt(111). The step function represents the hydrogen pressure during the time-lapse series. The data points represent the mobility of TFAP at each hydrogen pressure step.

Nevertheless, the different contributions to the overall mobility can be extracted from the plot in Fig. 3.9 b. While the average displacement of the TFAP molecules increases only slightly with increasing hydrogen pressure, the standard deviation of the values for individual molecules (given by the error bars) is becoming significantly smaller. This is a consequence of TFAP's tendency to form dimers. At low hydrogen pressure a higher fraction of the TFAP molecules is part of a dimer than at higher pressures, where almost exclusively monomeric TFAP is present. Therefore the average displacement measured at low pressure consists of a contribution from the dimers (low mobility) and from the monomers (high mobility), which leads to a high standard deviation. On the other hand, at high pressures the average displacement value consists almost exclusively of the values of the monomers, resulting in a smaller error bar.

Based on this argumentation one would expect to see a more prominent increase of the average displacement in Fig. 3.9 b, since most of the TFAP molecules are present in a monomeric form. The apparent contradiction is an excellent example for the influence of the local adsorbate coverage on the mobility of an adsorbed species [125–127]. As a high fraction

of TFAP molecules is tightly bound into dimers at low hydrogen pressure, a big part of the surface is available for the unhindered diffusion of the monomers. In other words, the strong tendency to form dimers at low hydrogen pressure favours a high average displacement of the monomers. In the high pressure regime, however, almost all TFAP molecules are monomers. This leads to a homogeneous distribution of molecules with a equally high density of molecules in the neighbourhood of each monomeric molecule. As result, all monomers move in smaller jumps interacting more regularly with adjacent molecules. This model explains why there exist higher displacement values in the low pressure regime than in the high pressure regime, as can be seen from upper limits of the error bars in Fig. 3.9 b.

3.8 CD on Pd(111)

An STM image of 0.25 ML of CD deposited onto a Pd(111) single crystal is shown in Fig. 3.10 a. Although this is a different substrate, again a random distribution of the molecules is observed and at least two different adsorption modes can be distinguished. One of them is clearly similar to the flat adsorption mode identified for CD and CN on Pt, even though the resolution in the image shown is lower than in the previous images it is clearly visible that this adsorption mode consist of two parts: a rather flat, oval bottom part and a relatively flexible (under the tip influence flexible) top part. This is in agreement with a flat adsorption mode as identified before. At first sight, the time-lapse image series revealed that already in the low pressure regime, the flatly adsorbed molecules, which are not part of a larger cluster, show a remarkable high mobility (filled triangles in Fig. 3.10 b). This is a significant difference to the mobility observed for the analogous surface species population on Pt, which can be seen if one compares the graph of filled triangles in Figs. 3.7 b and 3.10 b). Since a high fraction of all molecules on Pd belongs to this surface species population, the overall mobility in this image series is much higher than on Pt. Furthermore the mobility of all adsorbed species is almost independent of the hydrogen pressure. With one exception: At the highest pressure range the species represented by triangles couldn't be tracked any more, as shown by the missing data point. Probably their mobility gets so high that we can't image the molecules anymore since these molecules only appear as streak noise in the STM image.

The molecules marked with dashed circles in Fig. 3.10 a differ from the flatly adsorbed molecules in several ways. In the topographical image they lack the characteristic signature for the flexible top part, which is a clear sign for an adsorption geometry significantly different from the flat adsorption mode. However, the resolution obtained does not allow any conclusion on the precise adsorption geometry. The surface mobility of this surface species population (circles in Fig. 3.10b) is clearly distinct from the flatly adsorbed molecules. There is virtually no mobility observable, independent of the local environment (free molecules vs. dimers/clusters) and independent of the hydrogen pressure. This is a further justification for the identification of these molecules as a second surface species population. Changes in the mobility pattern like those identified as flipping events from the tilted to flat mode of the CD/CN on Pt systems have never been observed on Pd(111) for any surface species.

Altogether this means that on Pd(111) the flatly adsorbed surface species population is the more mobile species, in contrast to the observations for CD and CN on Pt(111). In addition there seems to be no (measurable) effect of the hydrogen pressure on the surface diffusion on Pd, at least in the pressure regime accessible in our experiments.

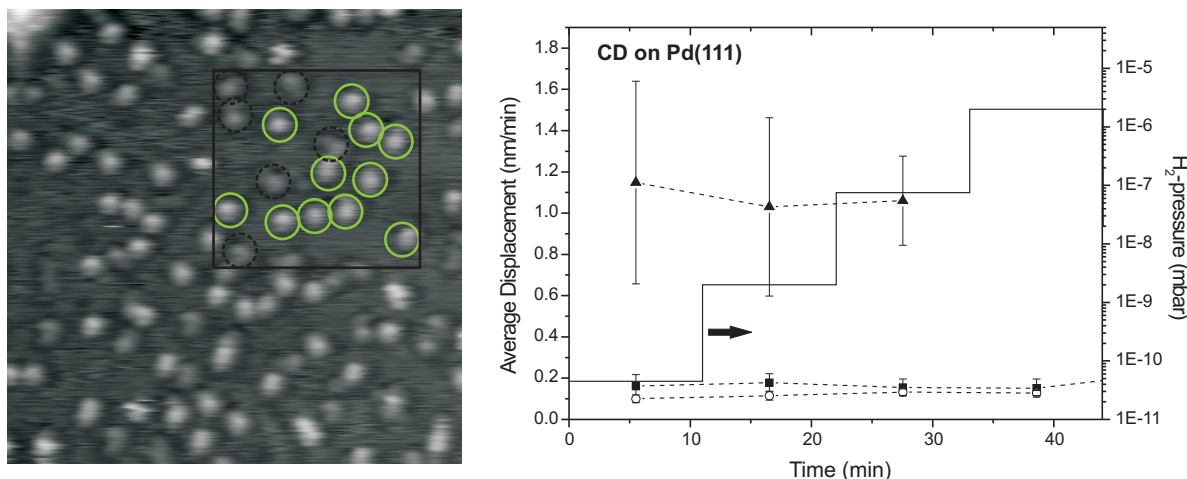


Figure 3.10: (a) STM image of CD (0.25 ML) on Pd(111) at low hydrogen pressure (2×10^{-10} mbar). Inside the marked area, representative for the whole sample, two different adsorption modes of CD are highlighted. Green circles designate the flatly adsorbed molecules, dashed circles mark a different adsorption mode. Image size: 25×25 nm, $I = 22$ pA, $U = 1.05$ V. (b) Average displacement measured for CD on Pd(111). The step function represents the hydrogen pressure used in the time-lapse series. Filled symbols show the mobility of flatly adsorbed molecules, where the triangles stand for free molecules and the squares stand for molecules in clusters. Outlined circles represent molecules adsorbed in a different adsorption mode, with a rather dark appearance.

3.9 Discussion

For the sake of clarity not all molecules in Figures 3.3, 3.4 and 3.7 have been marked as green, red or yellow species. However it can be seen easily, that the majority of those molecules which have not been marked, are characterized by the sharp dark-bright feature typical for the green species. If all molecules are summed up, almost 90% of the CD molecules adopt this flat adsorption mode. This interpretation is supported by the fact, that all these molecules are virtually immobile, very much the same as the 6 selected molecules which have been marked with a green circle.

Unfortunately, there is no direct proof for the adsorption geometries we suggest in Fig. 3.5. However we could not identify any other adsorption geometry of CD which could explain both, the very low mobility of the molecules on Pt(111) and the flexibility of the quinuclidine moiety, we observed for the green species. Furthermore, recent calculations showed that such an adsorption geometry of CD is very stable on Pt(111) [115]. Still, with the resolution possible to obtain with STM at room temperature, we can not exclude that the full population of the green species consists of different adsorption geometries which differ from the one shown in Fig. 3.5 a in some respect as e.g. (i) the precise angle between the Pt surface and the plane of the quinoline ring or (ii) the rotation of the quinoline ring around the C9–C4' bond by 180° , discriminating between open(3) and open(4) or closed(1) and closed(2) conformations.

For the adsorption geometry of the red species the situation is less evident. Besides the adsorption geometry shown in Fig. 3.5 b and c, other structures, where the quinuclidine part of CD is fixed to the surface by an additional interaction are possible. Such a structure bearing the potential for the hydrogenation of the terminal C=C-double bond has been found recently through calculations [115].

It is interesting to compare our STM data with the wealth of spectroscopic and catalytic data available for the Pt/CD system. Even though the results presented here have been measured at conditions far from the real catalysis conditions (pressure gap) there is a good level of agreement with the findings obtained by other techniques. For example, the predominantly flat adsorption as well as the existence of tilted (mainly at higher coverage) adsorption modes has been observed by different spectroscopic methods [121, 122, 128]. The importance of flat adsorption of CD has also been demonstrated by catalytic studies [129]. The hydrogenation of the terminal C=C-double bond is known to occur fast under catalytic conditions and during *in-situ* ATR-IR spectroscopy [121–123], and the partial hydrogenation of the aromatic moiety of CD and its consequences for enantioselective hydrogenation have been investigated by various groups [123, 124, 130]. Finally, the very low surface mobility observed for most CD species is also in agreement with the observation of Bakos et al., who showed by cyclic voltametry that the adsorption of CD on Pt is irreversible [131].

The random distribution of the CD molecules on the whole Pt(111) surface, independent of coverage, stands in contrast to findings recently reported on copper [93, 94]. As already stated, those findings are very doubtful as a second group could not reproduce the CD assemblies, but could attribute the assemblies to the solvent used [95]. Anyhow, with Pt the formation of an ordered assembly is not possible, due to the much stronger interaction of the molecules. Future investigations should therefore focus on Pt, as the investigation of CD on nonreactive metals such as Cu are likely to be of no or minor relevance concerning the surface processes involved in asymmetric catalysis.

As already stated in the introduction the complex systems addressed in our experiments do not allow for the determination of physical quantities such as the hopping rate h or the diffusion barrier energies E_D , because the potential energy hypersurface for the adsorption of molecules like CD and CN is very complex and subject to changes in the course of dynamic processes. As a consequence the value of our measurements lies in the possibility to directly compare the results obtained under identical conditions on different molecule-substrate combinations.

It is therefore interesting to relate the surface diffusion behaviour of CD and CN, and in particular the observed differences between them, to the well known catalytic behaviour of the Pt and Pd cinchona alkaloid system. As shown in Figs. 3.7 b and 3.8 b, the dynamic behaviour of these two chiral modifiers on Pt(111) is very similar but not identical. This is not surprising, as one would expect an identical behaviour only for real enantiomers, while CD and CN are "near-enantiomers" or to be precise: diastereomers. This is also reflected in a wealth of catalysis experiments, which show that CD and CN behave almost like enantiomers, yielding the products with different absolute configuration at the newly formed stereocenter. However, the efficiency of the reaction concerning the enantiodifferentiation is slightly different for CD and CN. Typically the enantiomeric excess (ee) to the (R)-product achieved with CD is higher (by a few percent) than the one with CN to the (S)-product, as already observed in the original studies by Orito et al. [102]. The origin for this small difference is still not clear. No direct evidence for a difference in the adsorption mode or the conformational behaviour has been found so far. The first indirect clue has been given by Huck et al. [130] who found that predominantly the product with the absolute configuration expected for a reaction with CD as chiral modifier was formed, when using 1 : 1 mixtures of CD and CN or even an excess of CN. However, from these experiments it could not be concluded whether the origin of this nonlinear effect lies in a difference of the adsorption strength of the two modifiers and/or (subtle) differences in the conformational or geometrical configuration between modifier and reactant, responsible for the enantiodifferentiation.

Our STM and diffusion analysis data provide further important evidence for answering this longstanding question. In principle, either different surface species populations with different chiral efficiencies or differences in the adsorption strength could be at the origin of the nonlinear effect observed. While different surface species population cannot be ruled out with the presently available experimental evidence, our STM and diffusion analysis data clearly indicate a difference in the adsorption strength between the flatly adsorbed CD and CN molecules as the origin of the nonlinear effect. Indeed this is the only difference we observe between the two modifiers in our diffusion analysis. Compared to CD, the average displacement is higher for the flatly adsorbed CN molecules. As the adsorption of these molecules is through strong chemisorption, including several chemical bonds between several surface atoms and various carbon atoms of the quinoline ring system [132, 133], the average displacement is a direct measure of the adsorption strength. As a consequence the flatly adsorbed CN molecules adsorb less strongly on the Pt surface than the flatly adsorbed CD molecules. As all existing mechanistic models consider the flatly adsorbed CD/CN molecules as the catalytically relevant species [78], our results could explain the nonlinear effect: If CD and CN are coexisting in a reactor fluid, the concentration of the flatly adsorbed CD molecules is higher on the surface than the concentration of the analogous surface species of CN. Of course this effect could be complemented by subtle differences in the geometrical configuration of CD/CN and reactant on the surface, which are beyond the resolution power attainable by STM for this system.

The other interesting observation is the difference in the diffusion behaviour of CD on Pt(111) and Pd(111). While on Pt the population of the flatly adsorbed molecules is almost immobile (Fig. 3.7 b), the flatly adsorbed CD molecules show a high mobility on Pd. This indicates that the adsorption strength for this surface species is higher on Pt than on Pd. Again this is in line with a well known fact: to obtain good enantioselectivities in hydrogenation reactions over Pd much higher CD concentrations are needed than on Pt [85, 134]. Due to the competition with reactant and solvent molecules a high concentration of CD is needed to cover a significant amount of the surface with CD molecules. On Pt, however, the interaction of CD with the surface is so strong, that small amounts of CD are enough to compete with other adsorbates. As a result, too high CD concentrations lead to a drastic decrease in reaction rate on Pt, since the reactants have to compete with CD for the adsorption sites.

Finally the differences between Pt and Pd observed here, complement existing knowledge attained by ATR-IR-spectroscopy [135], where it was found, that tilted adsorption geometries are more abundant on Pd than on Pt. This is clearly supported by our STM measurements. Our mobility analysis shows that on Pd the surface species population with the unknown adsorption geometry is less mobile than the flatly adsorbed molecules. Obviously there are adsorption geometries that bind more strongly to the Pd surface than the flat adsorption mode of CD. As a result, the flat adsorption mode is less abundant on Pd than on Pt, as observed in ATR-IR-spectroscopy.

The studies of TFAP on Pt as the only reactant in our study show an interesting case of cluster formation—the formation of TFAP dimers at low hydrogen pressures. The nature of this TFAP-TFAP interaction is most probably a dipol-dipol interaction, since TFAP has a strong electric dipol moment due to its carbonyl and CF_3 groups. This dipol-dipol interaction is further amplified on the metallic substrate surface by mirror image dipoles induced in the conductive substrate [136]. The interesting pressure dependency of TFAP—at higher hydrogen pressure only TFAP monomers are present—hasn't been investigated so far in the community of heterogeneous enantioselective catalysis and can become of interest on the background of

the 1 : 1 interaction model [107]. At low hydrogen pressure the formation of a TFAP-modifier complex competes with the TFAP-TFAP cluster formation and may thereby influence the reaction kinetics. As already noted, the splitting of TFAP dimers into monomers is reversible when going back to lower hydrogen pressures after closing the hydrogen leak valve. This could indicate that the TFAP molecules are not hydrogenated or otherwise chemically changed during the whole process.

3.10 Conclusions and Outlook

Compared to all other catalytic and spectroscopic techniques used on the Pt-cinchona system, the fundamental difference of our STM approach lies in the fact that we can gain information on the level of single molecules and follow their behaviour with time. This is particularly advantageous because in heterogeneous catalytic processes it is impossible to know a priori whether the most abundant surface species is also the most relevant for the catalytic process [137]. The discrimination of different surface species by their mobility and the time-resolved observation of their surface chemical processes provides a powerful tool for the investigation of complex catalyst systems such as the Pt-cinchona system. The results presented in this thesis demonstrate the feasibility of such an approach, although the ultimate goal - the elucidation of the mechanisms involved in the enantiodiscrimination on a single molecule level - has not been reached. The main obstacle to achieve this goal is the lack of high resolution images of the CD molecules due to their flexibility and the complexity of the substrate molecule interactions.

Nevertheless, our analysis of the adsorption and surface mobility of CD, CN and TFAP on Pt and Pd has revealed some interesting facts:

- No ordered assembly of CD and CN could be found on both, Pt and Pd substrates. Instead a random distribution was observed, which corroborates the 1 : 1 interaction model.
- The discrimination of flat and tilted adsorption modes of CD and CN was possible in accordance with the results of Ferri et al. [122].
- The time-lapse STM series with varying hydrogen pressure showed that the tilted species of CD and CN on Pt flip to a flat adsorption mode at higher hydrogen pressure. This is in agreement with the catalytic observation of side reactions (hydrogenations) occurring at the quinoline ring of the modifier during catalytic reactions performed at technological relevant conditions.
- The different mobility of CD and CN on Pt indicates the origin of the non-linear effect to be due to the difference in adsorption strength between the flatly adsorbed species of the quasi-enantiomers CD and CN [138].
- CD has a higher mobility on Pd than on Pt in agreement with the experimental finding that much higher CD concentrations are needed on Palladium for high catalytic efficiency.
- Adsorption of TFAP on Pt showed dimer formation at low hydrogen pressure whereas at higher pressure monomeric species became dominant. The shift in the dimer/monomer population upon change in hydrogen pressure was reversible, indicating that no irreversible chemical reaction (hydrogenation) occurred.

All together our work showed that STM investigations can complement other surface analytical methods and quantum chemical calculations in order to gain insight into the mechanistic aspects of this complex catalyst system. The results presented demonstrate the possibilities and limits of STM investigations for complex catalytical processes. The next step, the co-deposition of the complete enantioselective system of TFAP and CD, was already done but no conclusive statement could be made so far. One major drawback of STM herein is the lack of chemical information. In order to take a closer look on such a system it would be of great interest to know if the reactant (TFAP in our case) is already hydrogenated after complex formation with the modifier or not. It is also not clear yet if the low UHV hydrogen pressures used will induce the hydrogenation at all. An IR spectrometer combined with the STM could probably help to elucidate this problem if the signal to noise ratio is sufficiently high.

The major problem to solve in the future is the improvement of the resolution for scanning the modifier molecules. One possibility would be the investigation of modifiers which don't exhibit the flexibility of the quinuclidine part. An hungarian group of researchers [139] once described a synthetic cinchona derivative (α -isocinchonine) with a fixed open conformation, which still showed enantioselectivity.

Another option would be to extend the quinoline ring of the CD/CN modifiers by adding e.g. a phenyl group, which would certainly improve the possibility to identify their adsorption mode and geometric relation towards the reactant. In the same sense, larger reactants would be desirable to be able to discriminate whether they are adsorbed in a pro-R or pro-S enantiofacial form. The choice of a new reactant is not as easy as expected, because in addition to its function in the catalytic system, its usability under UHV conditions is of importance. One also could think of a reactant which forms ordered chains or structures via self-assembly. A reactant forming a complex with a modifier would thereby mediate its enantiofacial chirality into an ordered tail or structure far from the modifier's flexible moieties and give us the possibility to indirectly conclude on its enantiofacial form.

As a final remark I would like to mention that STM studies on such real catalytic system are experimentally most demanding. Not only are the CD/CN molecules large and complex in comparison to small molecules as e.g. CO investigated successfully so far [2], but also those molecules are not standard STM 'white mice' molecules as e.g. perylene and porphyrin derivatives normally done in the Nanolab. Additionally, the handling of the very reactive Pt and Pd surfaces was difficult in the rather big Nanolab UHV system, also seen in the light of a room-temperature system used for several other projects. A direct evidence for these experimental difficulties is the fact that there do not exist many studies of comparable real catalytic systems [46, 87, 91] and even the existing ones have sometimes questionable results [93, 95]. Nevertheless, the field of catalysis on surfaces still provides a lot of interesting questions and promising advances may be possible by the combination of different techniques as shown very recently by Berner et al. [140].

4 Assembling Organic Molecules on Surfaces with In-situ Reactions

This chapter summarizes the work on a project done in collaboration with Prof. Lutz Gade from the University of Heidelberg. Prof. Gade provided us with a perylene derivative, 4,9-diaminoperylene-quinone-3,10-diimine (DPDI), which was deposited and self-assembly was induced via an in-situ reaction on the metal surface.

4.1 Motivation

With Moore's law [141] in mind and the traditional fabrication methods of semiconductor industry rapidly approaching their fundamental limits [142–145], an alternative route to build smaller functional devices may be the use atomic and molecular systems as already suggested 56 years ago by Richard P. Feynman in his famous statement: "There's plenty of room at the bottom" [7]. The physics at such small length scales is dominated by quantum mechanical effects and therefore new materials and technologies as e.g. nano-powders or quantum computing [146] with completely new characteristics are imaginable. This new field of research is called *nanotechnology*, since the structural length scales of such systems are in the range of 0.1–100 nm.

One major need for technological applications in this context is the possibility to build large arrays of such nanostructured materials with sub-nanometer positioning accuracy of the individual functional units in order to achieve the same scalability as known from classical semiconductor microelectronics [147]. The most promising route to achieve this goal is to use autonomous ordering phenomena like self-assembly [148], self-organized growth or at some later point maybe even self-organization to structure organic molecular systems [8]. This so called *bottom-up* approach is fundamentally different from the classic *top-down* methods like lithography used in device fabrication until now. In contrast to top-down methods, which externally impose a structure on the material being processed, bottom-up methods aim to guide autonomous ordering by choosing wisely the individual constituents which should build up the new material. Making use of their inherent physical and chemical properties, setting up the right environmental conditions like temperature, deposition rates, cooling rates, etc. and intelligently designing linker groups attached to the constituents finally leads to desired structures. Thus, the bottom-up technique does not rely on an often time consuming step during which one actively has to build the structure. Once the mechanisms controlling the self-ordering phenomena are fully understood, the bottom-up approach combines the ease of (massively) parallel fabrication with exquisite control over shape, composition and mesoscale organization of the structures formed.

In this context, the concepts of supramolecular chemistry [149] have shown impressive results for molecular self-assembly on surfaces [150], making use of the sophisticated interplay between individual structural units. Moreover, it was possible to obtain self-assemblies of

nanoporous networks on surfaces which may later on act as a framework for trapping or placing functional units. In most cases, the assembly of the underlying building blocks of such networks is based on noncovalent interactions that shape extended supramolecular entities in variable dimensions [69, 151, 152] [153–158]. There are striking examples of molecular surface structures, whose formation is driven by metal co-ordination [159], dipolar coupling [155] or hydrogen bonding [160] interactions. However, the formation of such thermodynamically controlled aggregated structures is reversible in most cases and the interaction between the molecular components is frequently weak.

Therefore, the original goal of this project was to produce polymeric structures on surfaces by covalent cross-linking, which may exhibit better conductive properties and thus would be better suited for electronic devices. Up to now, various approaches to construct polymeric structures on surfaces have already been reported. For example molecules possessing acetylene and diacetylene groups were used [161, 162] to build up 1D as well as 2D structures on highly oriented pyrolytic graphite (HOPG) surfaces. These structures were obtained by irradiation with UV light to induce the covalent coupling between the individual monomers. While the one-dimensional (1D) wires generated by photo-polymerization were randomly distributed on the surface, the length of the polymeric chain and its position on the surface could be controlled using STM polymerization. This has been nicely demonstrated by the group of Okawa and Aono [163], which employed a diacetylene containing compound to produce linear conjugated polymer nanowires either by applying a voltage pulse with a STM tip or by irradiation with UV light. Another class of molecules used for surface polymeric structures are thiophene derivatives, either as pre-synthesized polythiophenes which spontaneously self-organize on a surface [164, 165], or thiophene monomers which are transformed into 1D wires by electrochemical epitaxial polymerization [166]. However, in all these approaches the dimensionality of the resulting polymer is given and cannot be varied.

4.2 A Short Introduction to the Chemistry of DPDI

The starting material for this surface study was 4,9-diaminoperylene-quinone-3,10-diimine (DPDI **1** Fig. 4.1), which we kindly obtained from the inorganic chemistry group of Prof. Gade in Heidelberg. From bulk DPDI it was known that it polymerizes under the release of ammonia and therefore was a good starting point for our goal of covalently linked surface self-assemblies. Basically, DPDI is a planar aromatic molecule consisting of a core of five benzene rings with one amine and imine functional end group on each short side of the molecule. This so-called perylene core forms a large π -system and molecules with large π -systems, as e.g. pentacene and perylene derivatives, phthalocyanines, porphyrins or flake like aromatic hydrocarbons, are popular to be studied in surface science and a wealth of literature exists [167–171]. To a large extent this is due to the fact that these flat aromatic molecules are often easy to handle both from a chemical point of view and under UHV conditions needed for many surface science methods. Such molecules are often flat lying on a substrate surface when deposited in a submonolayer regime since the extended π -system couples unspecifically to the metallic substrate surface. Additionally, their often relatively simple, almost rectangular shape facilitates a laterally dense packing. Depending on the functional groups applied to such aromatic molecules various sorts of assemblies can be formed. A very famous example of the perylene family is perylene-3,4,9,10-tetracarboxylic-dianhydride (PTCDA) [172, 173] which assembles in a herringbone pattern on Ag(111) [174], HOPG and MoS₂ [175] and is

envisioned as an organic semiconductor for technological applications in organic field effect transistors (OFETs) [176, 177] or organic light-emitting devices [178, 179].

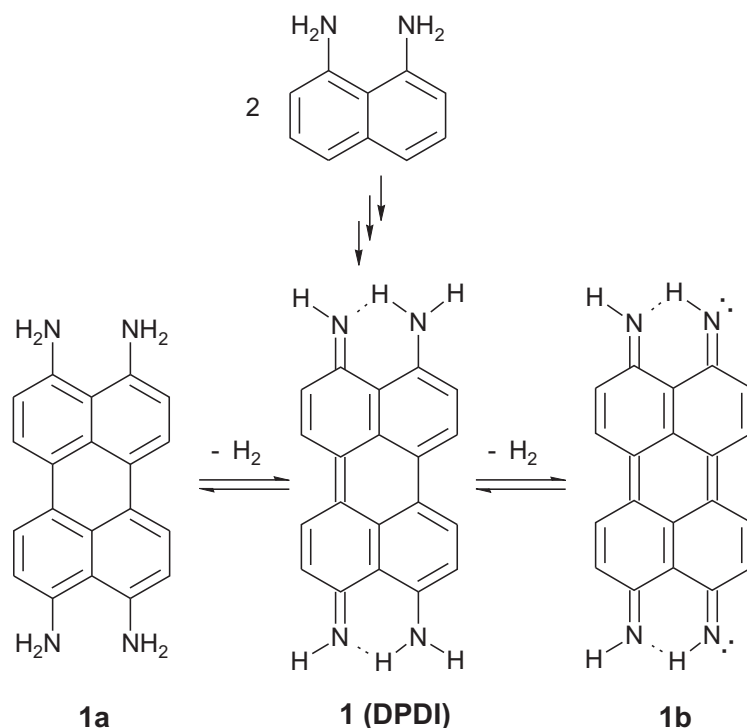


Figure 4.1: The formation of DPDI **1** by oxidative coupling of two 1,8-diaminonaphthalene molecules, and its redox conversion into **1a** and **1b**.

Synthesis of DPDI was first reported by Zinke et al. [180] in 1929. Their preparation started from parent perylene which was converted to 3,4,9,10-tetranitroperylene by treatment with concentrated nitric acid. This resulting compound was then reduced in alkaline solution to give DPDI. However, it has received little attention since then, due to its cumbersome synthesis and the extremely low yield for the desired product. In 1998, Hellmann et al. [181] presented a new one-pot synthesis for DPDI by oxidative coupling of two silylated 1,8-diaminonaphthalene molecules which involves the—probably—concerted demetalation and coupling of two thallium amides. After treatment of the resulting silylated quinoidal perylenes with KF in methanol or water the parent DPDI compound is received with a high yield for the final product.

DPDI displays a particularly rich redox chemistry [182]. Its most stable form corresponds to the semiquinoidal structure **1** displayed in figure 4.1, which on the one hand can be reversibly converted to the perylene **1a** by a two-electron reduction, as previously shown for derivatives bearing bulky N-silyl groups. On the other hand, a two electron oxidation gives rise to the quinoidal redox state **1b** by dehydrogenation of the amine groups. It is important to note that the combination of amine and imine groups connected to a naphthalene moiety as in the semiquinoidal form **1** is not common in chemistry, since such compounds are likely to polymerize under release of ammonia. Probably the delocalized π -system of the perylene core stabilizes the imine and amine end-groups in the case of DPDI. Additionally, DPDI exhibits tautomerism, a special form of structural isomerism, since the two H atoms in-between the N atoms jump from one side to the other at room-temperature, changing the arrangement of the imine and amine groups. The energy barrier for such structural changes could be analyzed by

ab initio transition state calculations but this is very demanding in terms of computing time. Since the DPDI molecule in its semiquinoidal form **1** is only surrounded by a ring of H atoms and does not exhibit a strong quadrupole moment as PTCDA, it will essentially interact via van-der-Waals interaction with other molecules when deposited on a substrate.

4.3 DPDI on Cu(111) - Linear Chains

Unless otherwise stated, the experiments described in the following were performed in the same Nanolab multi-chamber UHV system as used for the experiments of the previous chapter. The Cu(111) and Ag(111) single crystals were cleaned and prepared by repeated Ar⁺ ion sputtering (800 eV, 4×10^{-7} mbar, 20–15 min) and subsequent annealing at 600–700 K and 870 K, respectively, via resistively heated stubs for about an hour. This standard procedures lead to clean and flat surfaces. In the molecule deposition chamber the DPDI molecules were sublimed from a resistively heated tantalum crucible at about 200 °C. During deposition the substrate was kept at room temperature and a custom-built quartz microbalance was used to measure the deposition rate. Annealing of a covered sample was performed in the ESCA chamber with the external filament of the manipulator, which—in contrast to the stub internal filaments—is heating the whole manipulator head. This allows for a better temperature repeatability while the temperature is measured via a thermocouple connected to the manipulator head. The samples were investigated with our home-built STM operated at room temperature. All STM images were obtained in constant-current mode.

If one deposits DPDI on atomically clean Cu(111) or Ag(111) surfaces and checks the results with an STM, no ordered structures can be found for submonolayer coverages prior to annealing. Only a highly mobile 2D gas phase of DPDI is present on the surface. If exactly 1 ML of DPDI is deposited and scanning conditions are good, different rotational domains of a tiled pattern with a rectangular unit cell of 0.92 nm × 1.3 nm can be found on the whole surface. This arrangement is controlled by the molecular shape of DPDI, whose size approximated with van der Waals radii is similar to the dimensions of the unit cell found. In the following, one monolayer of DPDI corresponds therefore to the amount of molecules that is needed to cover the complete surface with flat lying molecules and corresponds to 0.84 molecules per nm². The high mobility of DPDI on the metal surface is unsurprising as there is no possibility for lateral intermolecular interactions other than van-der-Waals forces. In principle, the amine functional endgroups of **1** might act as hydrogen-bond donors. However, an appropriate acceptor functionality is missing, since the molecule is surrounded by a ring of hydrogen-saturated C and N atoms. The nitrogen atoms of the imine and amine endgroups also do not bind to the surface or otherwise influence the electronic structure of the molecule in a way which would increase the diffusion barrier E_D for the molecules and lead to a registry with the corrugated energy surface of the substrate. For the similar PTCDA molecules on Ag(111), for example, it is known that the electron-withdrawing carboxyl groups of PTCDA enhance the π -bonding to the metal support, thus locking the molecules into specific sites and orientations. Additionally, the carboxyl oxygen binds to the surface and PTCDA has a strong quadrupole moment. Thereby self-assembled islands of PTCDA on Ag(111) [183–185] are formed.

As will become apparent in the following discussion, the deposited DPDI molecules will be chemically modified on the Cu surface while annealing at 300 °C. Whereas on the Ag(111) surface such structures as presented below could never be observed, since annealing caused the

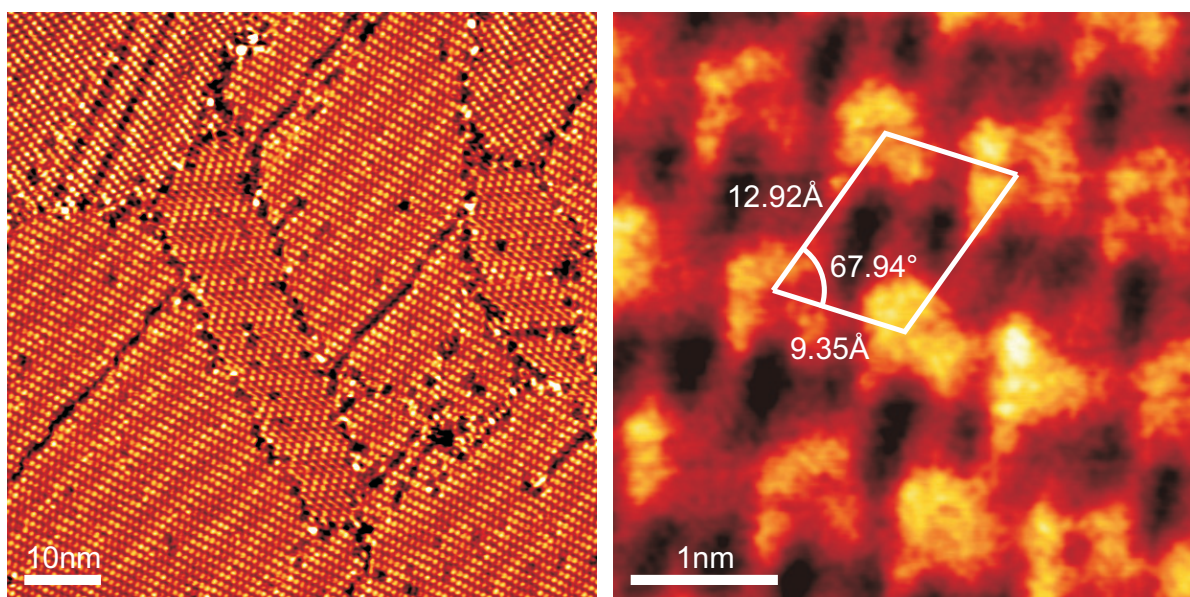


Figure 4.2: (left) STM image of 1 ML DPDI deposited on Cu(111) and annealed at 300 °C showing different domains. (right) Zoomed STM image with the adsorbate unit cell superimposed.

desorption of the molecules before any reaction could take place. Therefore all the following results are unique to the Cu(111) surface. In Fig. 4.2 STM images of 1 ML DPDI on Cu(111) after annealing are shown. The most obvious difference to an unannealed sample is the fact that the former rectangular unit cell changed to a rhombic one. This can be clearly seen from the STM image in Fig. 4.2 right in which the unit cell is superimposed. The parameters of the unit cell have been achieved by averaging over several STM images of different size and from different samples. In overview STM images like the one in Fig. 4.2 left six different rotational domains are observed, while the minimum angle between two domains is about 22°. The domains exhibit a one-dimensional moiré pattern with the modulation running along the short unit cell direction. Such modulated structures are often observed with STM in the case of lattice-mismatched systems consisting of substrate and adsorbed layer. For example moiré patterns were observed for monolayer graphite on metal substrates [186, 187]. Such patterns are often explained in the simple picture, that the superposition of two periodic structures having different periodicities leads to beating in the electronic structure¹ similar to the beating known for the superposition of two waves with slightly different frequency. However, the complete picture is more complicated and two publications by Kobayashi [188, 189] give an excellent theoretical introduction to the problem.

Following these argumentations, the observed periodicity of 6 from one bright (large apparent height) molecule to the next bright molecule indicates a 6×1 coincidence supercell along the short direction of the adsorbate unit cell in our case. With this indication in mind, the LEED experiments described in the following could be evaluated and the superstructure could be understood.

¹The emphasis on electronic structure should be noted here: Since the corrugation of such moiré patterns is much higher than the atomic corrugation of the surface and such patterns haven't been observed by AFM yet, the phenomenon cannot be solely explained by small atomic displacements.

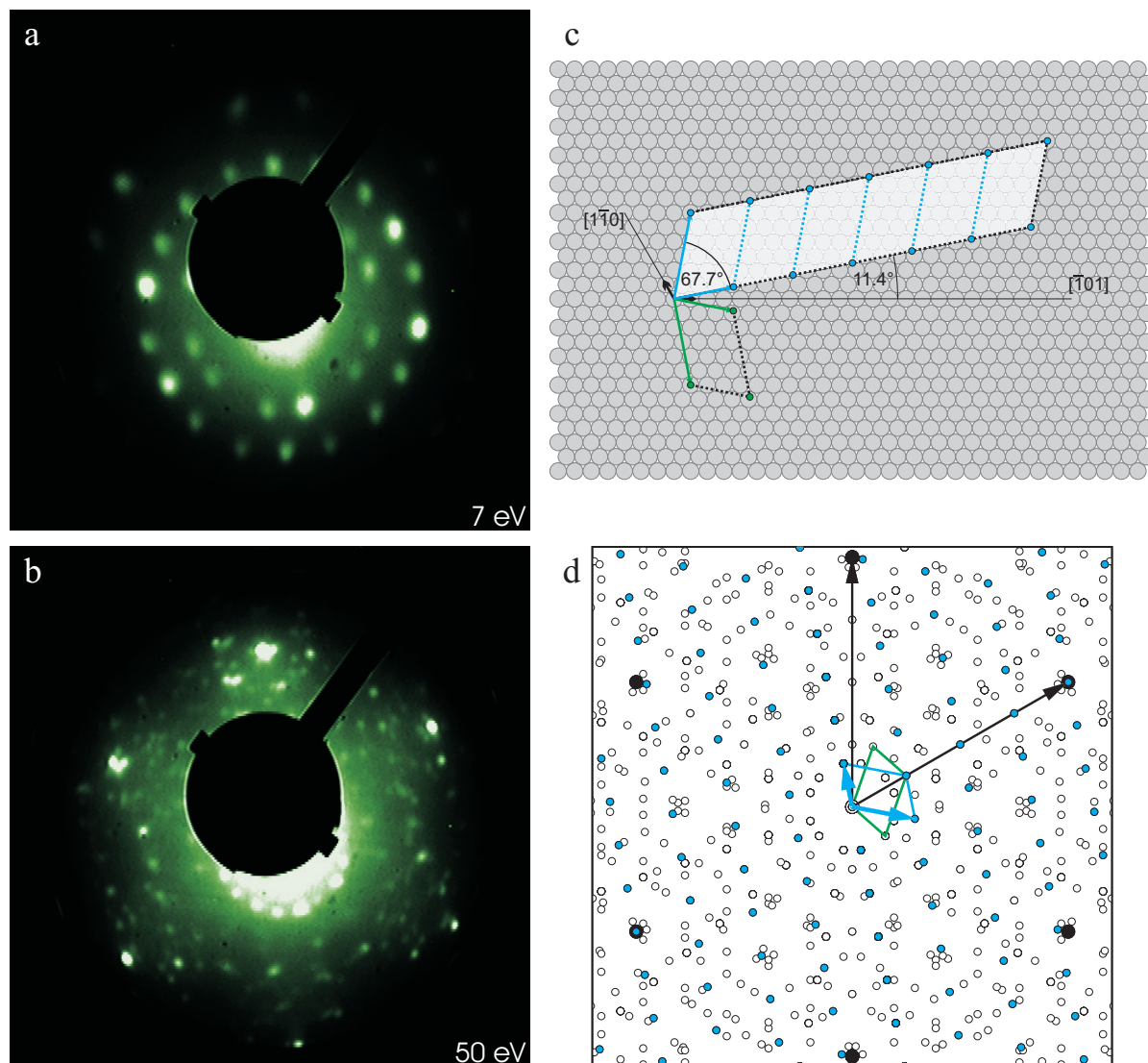


Figure 4.3: Surface structure determination of 1 ML DPDI on Cu(111) annealed at 300 °C. LEED patterns of the sample taken with (a) 7 eV and (b) 50 eV beam energy. (c) Superstructure model with coincidence supercell and mirror unit cell (green). (d) Simulated LEED pattern for comparison.

In order to better determine the superstructure LEED measurements of 1 ML DPDI on Cu(111) were carried out after annealing at 300 °C. Fig. 4.3a and 4.3b show two LEED patterns: The one at 7 eV shows the first diffraction order of the molecular adsorbate structure, the other one at 50 eV shows the first diffraction order of the Cu(111) substrate. For a better visibility of the first order adsorbate diffraction spots the sample has been slightly turned away from normal incidence conditions. In Fig. 4.3c and 4.3d the real space adsorbate structure and a simulated LEED pattern obtained with LEEDpat2 [190] is shown. As a starting point the averaged unit cell values from the STM data ($r_1=9.35$ Å; $r_2=12.92$ Å; $\gamma = 67.94^\circ$) have been used. The complete pattern is constructed by mirroring the adsorbate structure along the $[\bar{1}01]$ substrate direction (shown green in the upper right part of figure 4.3) and allowing three rotational operations by 120° due to the threefold substrate symmetry. By comparison of the simulated with the real pattern the real matrix notation of the superstructure is found to be

$$M = \begin{pmatrix} 4 & 0.8333 \\ 4 & 6 \end{pmatrix}, \quad (4.1)$$

which relates the two adsorbate lattice vectors \mathbf{b}_1 and \mathbf{b}_2 with the substrate lattice vectors \mathbf{a}_1 and \mathbf{a}_2 via

$$\begin{pmatrix} \mathbf{b}_1 \\ \mathbf{b}_2 \end{pmatrix} = M \cdot \begin{pmatrix} \mathbf{a}_1 \\ \mathbf{a}_2 \end{pmatrix}. \quad (4.2)$$

Herein, \mathbf{a}_1 and \mathbf{a}_2 point in the $[1\bar{1}0]$ and $[\bar{1}01]$ directions of the substrate.

The fact that one number of the matrix is a rational number indicates that the adsorbate lattice and the substrate lattice are rationally related lattices [56]. From the STM moiré patterns and the fact that $6 \cdot 0.8333 = 5$ —an integer number—it is concluded that the unit cell of the combined adsorbate-substrate system (shown slightly transparent in Fig. 4.3c) is 6 times the adsorbate unit cell. This larger unit cell generates the so-called coincidence lattice. Following the conventions of [191] one speaks of a point-on-line coincidence of type IA. According to the criteria suggested therein this is an indication for rather low molecule-substrate interactions. The general wood notation [55] ($r_1=9.3210$ Å; $r_2=13.4933$ Å; $\alpha_1 = 11.39^\circ$; $\alpha_2 = 79.11^\circ$) of M with an inner angle of $\alpha_2 - \alpha_1 = 67.72^\circ$ compares well to the STM results noted above, which were used as a starting point for the LEED evaluation.

4.4 DPDI on Cu(111) - Hexagonal Networks

For lower surface coverages, only a mobile 2D gas phase can be imaged at room-temperature before annealing. After annealing at 300 °C, however, the mobile monomers aggregate to give a well-ordered 2D *open hexagonal* or *honeycomb* network as displayed in Fig. 4.4. Large arrays of ordered honeycomb islands are found, which can be seen in the large scale image on the left.

The image on the right of Fig. 4.4 suggests that the hexagonal network features carpet growth across step edges as known for thin NaCl islands [192–194] on metal substrates. However, the observed honeycomb structure across the step edge is actually due to a strain relaxation along glide planes of the crystal very common for the rather soft Cu single crystals. This is concluded from an overview image of this region, where it is observed that another boundary step edge of the terrace in STM image is running under an angle of exactly 60° towards the step edge shown. Most probably, this strain relaxation took place after the hexagonal network was formed and while the sample was cooling down from the 300 °C annealing temperature.

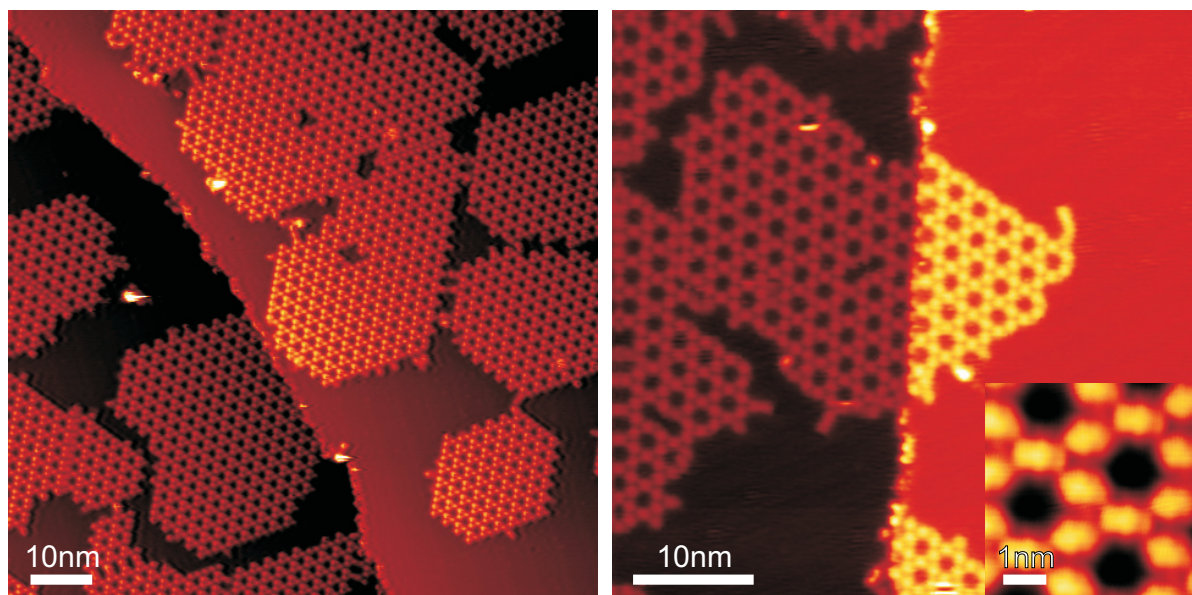


Figure 4.4: (left) STM height image of ≈ 0.6 ML DPDI on Cu(111) after annealing at 300°C . (right) STM image apparently showing carpet growth across a step edge. (small inset) Porous network with a periodicity of 2.55 nm. By subtracting the width of one molecule (0.93 nm) determined in the previous section this results in a pore diameter of about 1.62 nm.

From the small inset of the right part of the figure it can be seen, that 3 molecules arrange in a way that their short sides point against each other. 6 molecules then build up a pore leaving an uncovered Cu surface in its center. Since the periodicity of the network was determined to 2.55 nm, as will be shown in the following section, and if we assume the width of one molecule as 0.93 nm (determined from the unit cell parameter of the monolayer arrangement) the pore diameter of this nanoporous network is in the order of 1.62 nm.

Based on the STM data and the information obtained from the LEED pattern shown on the left of Fig. 4.5, a commensurate arrangement of the DPDI monomers with regard to the Cu substrate is determined. The nine adsorbate diffraction spots in-between the hexagonal substrate spots indicate a primitive (10×10) unit cell for the adsorbate superstructure. This leads to a lattice constant of 2.55 nm for the superstructure, since the lattice constant of the substrate lattice is the nearest-neighbour distance of copper with 2.55 Å.

The unit cell of this open hexagonal structure is made up from a basis consisting of 3 molecules which are rotated by 120° with respect to each other (see Fig. 4.5). From symmetry considerations the DPDI molecules should adsorb on top sites² of the copper substrate, since other adsorption geometries would lead to inequivalent adsorption sites for the 3 basis molecules; in particular the end groups would then adsorb at different adsorption sites. Due to the similar symmetries of substrate and adsorbate, there only exist translational domains. Consequent to the $p(10 \times 10)$ superstructure the nucleation of an island can start at several inequivalent Cu atoms. This may lead to many small ordered islands with many domain boundaries in-between instead of one big islands. During our studies we found out that we are able to increase the islands size by modifying the annealing process. Normally, annealing

²For molecules the geometric center of the molecule is considered for the definition of the adsorption site. In this case the top site adsorption corresponds to the central benzene ring adsorbed on top of a Cu atom.

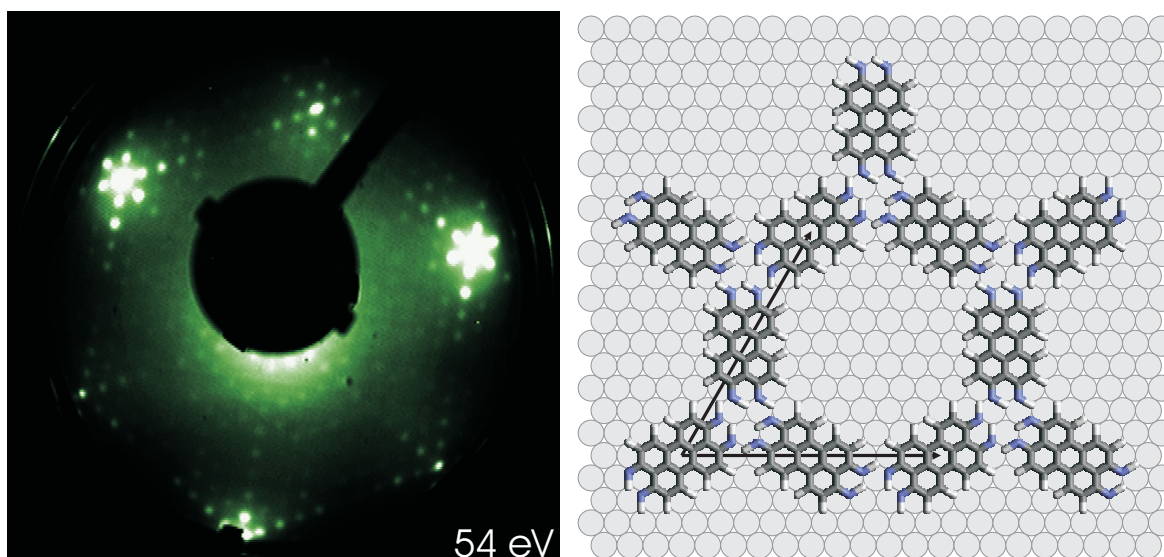


Figure 4.5: (left) LEED pattern of a maximum of 0.7 ML of DPDI on Cu(111) after annealing at 300 °C. (right) Model of the hydrogen bond supramolecular network with a hexagonal unit cell and a lattice constant of 2.55 nm. The basis of the adsorbate lattice consists of 3 molecules rotated 120° against each other. Therefore, each DPDI monomer is connected to 4 other monomers.

was carried out by setting a certain heating power (filament current) and waiting for about 45–60 min until the annealing temperature of 300 °C was reached. After the temperature was reached the heating power was immediately switched off and the sample was left cooling down on the manipulator. For the modified annealing process we prolonged this cool down process by adding an hour with half the heating power after reaching the 300 °C, which finally led to quite big ordered islands.

Once cooled down to room-temperature, the network exhibits an extraordinary stability as is reflected by its inertness towards manipulation of individual monomers with the STM tip. Moreover, in LEED experiments which were performed while annealing the sample the diffraction pattern of the overlayer persisted up to a temperature of 450 °C. Further increase of the temperature resulted in an irreversible destruction of the hexagonal perylene network. This does not necessarily mean that monomers of the structure get mobilized at such high thermal energies, but rather that their probability to be included in the ordered structure is still higher than the probability to remain in the 2D gas phase, which indicates high nucleation energies of the hexagonal structure.

4.5 DPDI on Cu(111) - Trimeric Bowls

For geometrical reasons, the honeycomb structure described above can only exist up to a maximum coverage of 0.7 ML. It was therefore of interest to assess if and how the structure changed upon going to higher surface coverage. And thus, a final step of probing the concentration dependence of DPDI assemblies, was to prepare a sample with a coverage of ≈ 0.85 ML. Upon annealing at 300 °C trimeric structures in the form of rings are identified as shown in Fig. 4.6. As expected for the higher coverage these rings are packed more densely on the surface than the honeycomb network discussed above.

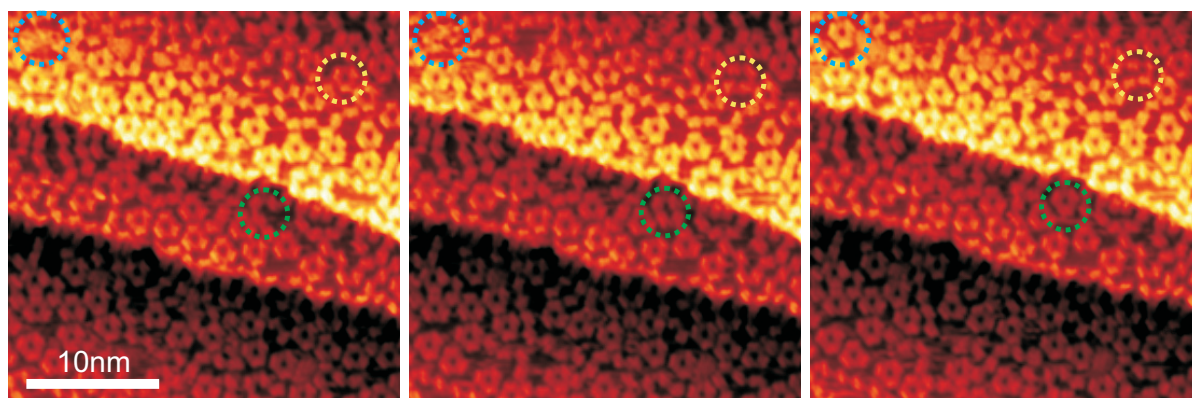


Figure 4.6: Series of STM images of 0.85 ML DPDI deposited on Cu(111) and annealed at 300 °C. The blue and green dashed circles exemplarily highlight areas where a trimer is formed. The yellow dashed circle marks a trimer which breaks open during the course of the STM sequence.

In contrast to the monolayer and the honeycomb structure, a dynamic equilibrium is observed since the trimeric structures are not stable. As designated by the dashed circles in Fig. 4.6, this is evidenced by the observation of a dynamic equilibrium of 'open' and 'closed' structures (trimers, chains and individual molecules) upon subsequent scanning of the same sample area at room temperature. Nevertheless, the trimers must be energetically more favourable than the linear chains at high coverage as observed for the monolayer. Otherwise the surface would be partially covered with the linear chain structure and the remaining space would show the energetically most favoured honeycomb structure.

4.6 Discussion

Due to its redox convertability explained in section 4.2, DPDI lends itself to chemical modification during annealing subsequent to its controlled deposition on metal surfaces and thus to significant changes in its intermolecular interactions.

The assembly of the observed honeycomb networks can be readily explained by a dehydrogenation of the DPDI monomers on the copper surface providing the autocomplementary compound **1b**, in which the now modified N-functions may act as both H-bond acceptors and donors. The molecules thus link up via H-bonding with each DPDI monomer binding to a total of four neighboring monomers (Fig. 4.7) to form the honeycomb network. Hydrogen bonding between the N-functions is consistent with the structural data from STM and LEED experiments from which an N—N distance of adjacent molecules of about 3.1 Å is derived. This distance is within a standard range of hydrogen bond lengths [195]. Additional evidence for the proposed chemical modification of compound **1** to **1b** as a result of the annealing process at 300 °C is given by XPS experiments before and after the thermolysis, which are described in detail in the following section.

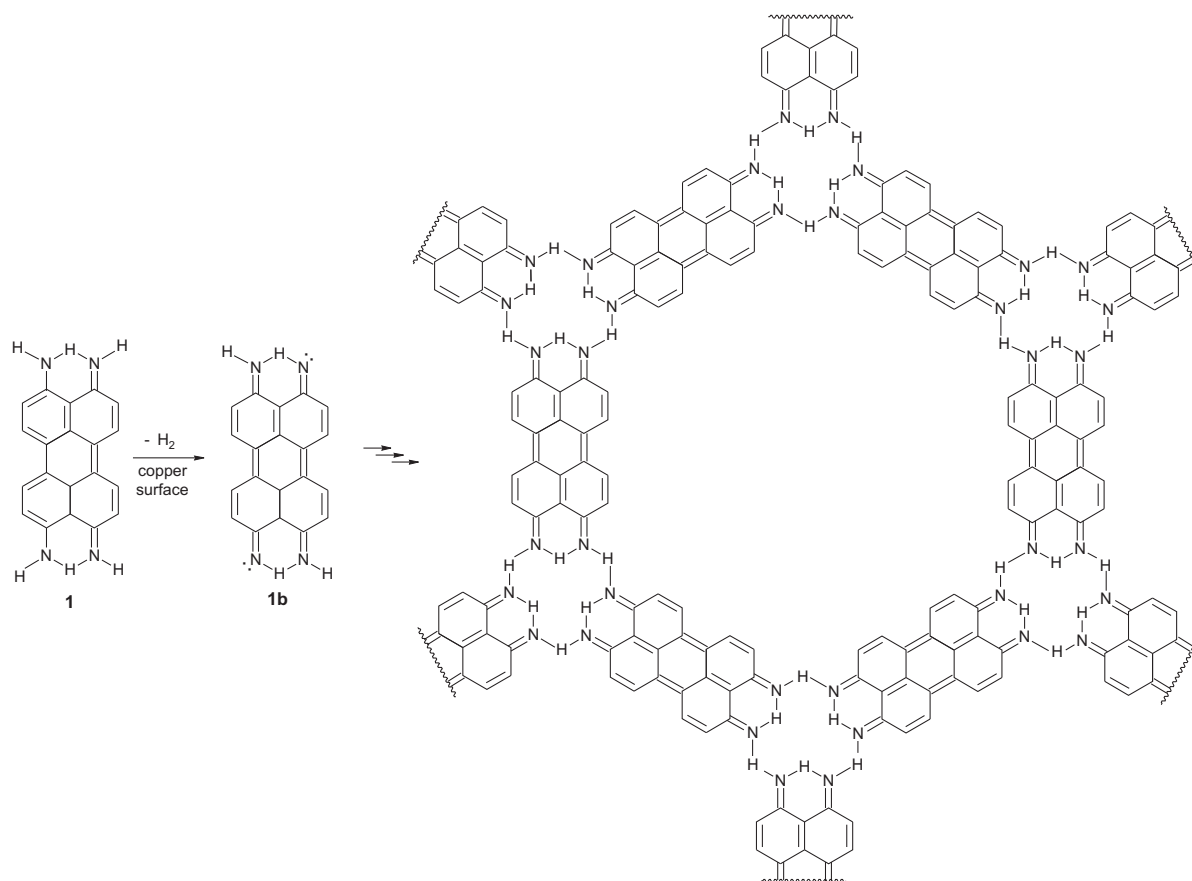


Figure 4.7: Hexagonal assembly of thermally generated **1b** on a Cu(111) surface.

Since it was not possible to observe a similar structure formation on Ag(111) by annealing, the dehydrogenation reaction of DPDI must be related to the higher reactivity of Cu compared to Ag. The Cu substrate may directly act as a catalyst for the dehydrogenation of DPDI and/or it sort of assists the reaction by hindering desorption from the surface, because the

adsorption energy of DPDI on Cu is higher than on Ag. First results on Pd(111) (Fig. 4.8) support the latter or at least indicate that the system is unspecific towards the catalyst in use: Before annealing, randomly distributed mobile DPDI molecules were imaged on Pd indicating a lower mobility as on Cu. After annealing, first initial nucleation stages of the hexagonal arrangement were observed, but the mobility of the dehydrogenated monomers was too low to form extended networks. Optimisation of the temperature treatment potentially might lead to extended assemblies also on the Pd surface.

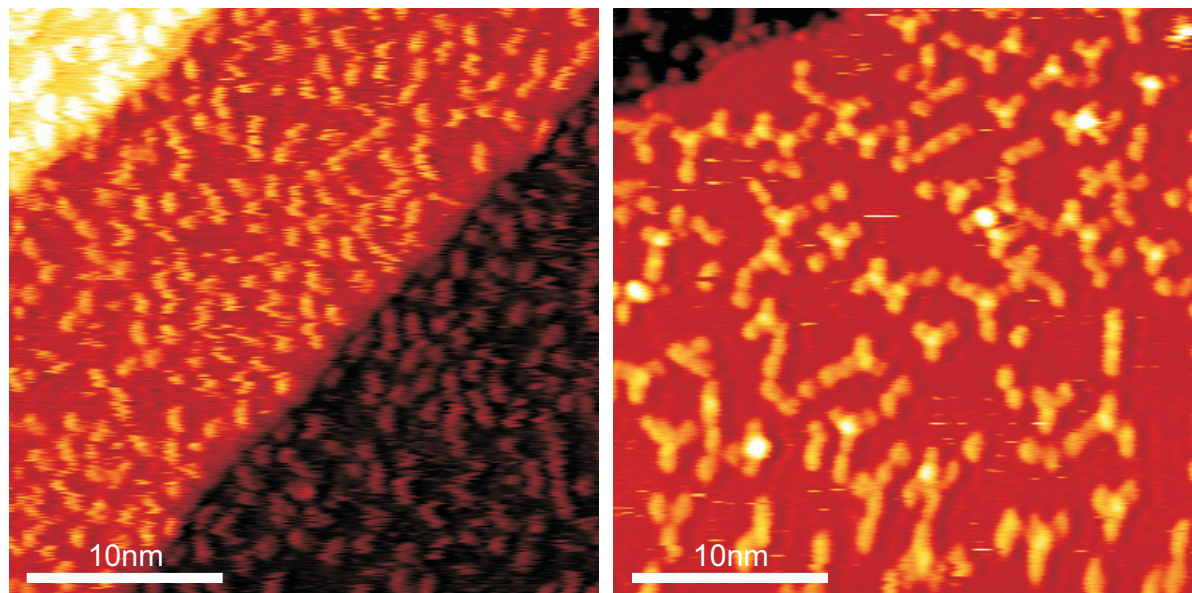


Figure 4.8: (left) STM image ($I = 25$ pA, $U = -1.61$ V) of mobile, unannealed DPDI on Pd(111). (right) STM image ($I = 20$ pA, $U = -1.61$ V) of the same sample after annealing. The molecules are not mobile anymore and initial nucleation stages of an ordered structure can be observed.

Therefore a key requirement for the formation of the highly ordered network appears to be the free mobility of **1**, and subsequently **1b** on the Cu(111) surface in order to attain the appropriate molecular arrangement and, secondly, the rather low molecular coverage on the metal support in order to accommodate the large hexagonal cavities in the two-dimensional network. Thus, as already stated, the honeycomb structure corresponds to a maximum coverage of 0.7 ML for geometrical reasons and trimers are formed at a slightly higher coverage. The formation of these trimers may be explained by the same dehydrogenation reaction as proposed for the honeycomb network yielding **1b**. This compound, activated for H-bond formation, then forms the observed cyclic hydrogen bonded structure in a self assembly process which is modified by a characteristic change of the diffusion length at the higher 2D molecular density. For the steric, repulsive interactions between the inward pointing hydrogen atoms of the perylene trimer, the overall structure is expected to deviate from a strictly planar arrangement and is expected to adopt an overall bowl-shaped form, a notion which is also supported by the STM images (Fig. 4.6). Due to this steric interaction and due to the fact that each monomer is only hydrogen bonded to two neighboring monomers, a less robust structure of lower binding energy is expected in this case. This is evidenced by the observation of the dynamical equilibrium of 'open' and 'closed' structures (trimers, chains and individual molecules) upon subsequent scanning of the same sample area at room temperature.

Furthermore, it was observed that only two preferred orientations of the trimers relative to the substrate exist, indicating that the structure of the Cu surface potentially contributes to the stabilization of the cyclic trimer.

The least stable structure of the concentration dependent polymerization patterns, is the full monolayer of DPDI on Cu(111). In contrast to the mobile submonolayer phases of the monomer, there is little room for molecular reorientation upon annealing of such a densely packed and highly ordered molecular array. The result of the thermal annealing of a DPDI monolayer on Cu(111) at 300 °C is displayed in Fig. 4.2 on the right. The STM revealed a zigzag chain structure of the polymer with the chains packing one alongside the other. These chains derive from the regular monolayer structure of the monomer by an apparently concerted "shearing" movement which is accompanied by shortening of the distance between adjacent molecular rows along the long molecular axis by about 1 Å. The same dehydrogenation reaction as for submonolayer coverage is thought to take place, resulting in each monomer being linked via H-bonds to four adjacent monomers. The moiré pattern in the STM images, as well as the LEED patterns of section 4.3 indicated that the molecular arrangement obtained in this annealing process does not interact strongly with the substrate. Weak interaction is tantamount to a higher potential energy and therefore this is well in line with statement that the monolayer arrangement is the least stable one.

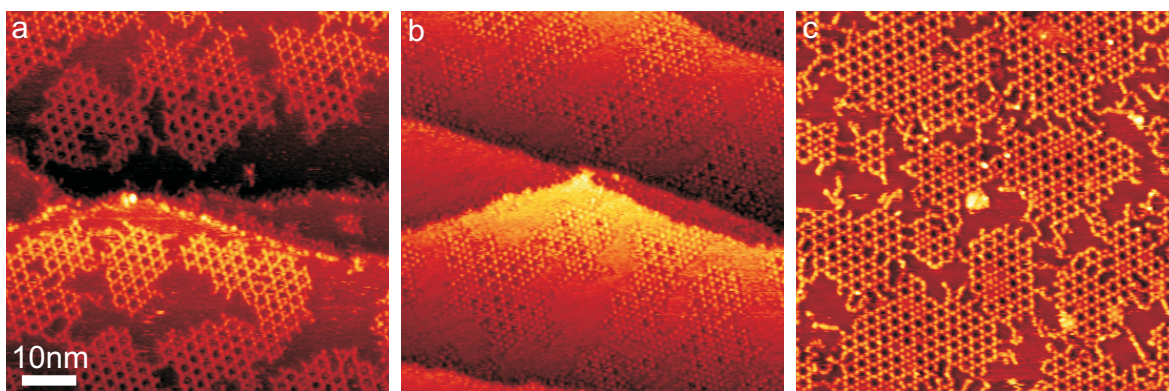


Figure 4.9: STM images ($70 \times 70 \text{ nm}^2$) of the same sample at different phases of sample preparation. First, the honeycomb network was prepared (a) and subsequently 0.15 ML DPDI were deposited (b). The additional DPDI molecules form a mobile phase on the bare Cu substrate and some are trapped in the pores of the honeycomb network. Annealing this sample again at 300 °C converts the mobile phase into a solid phase because of dehydrogenation of DPDI, thus resulting in an enlargement of the honeycomb network (c). Individual molecules remain trapped within the network. However, the characteristic confined mobility disappears after annealing.

Direct evidence for the importance of the conversion of DPDI to **1b**, and thus the formation of a monomer capable of forming two dimensional H-bonding networks, was obtained by depositing the equivalent of 0.15 ML additional DPDI onto the previously prepared honeycomb network (see Fig. 4.9). These additional monomers in their initial, non-dehydrogenated form are not assembled into the existing honeycomb network at room temperature, because the area covered by the network did not increase. Instead, the additional monomer molecules give rise to a mobile 2D gas phase on the free metal surface, as found for submonolayer coverage prior to thermal treatment. Other DPDI molecules are also trapped randomly in the hexagonal cavities of the honeycomb network, in which they are still mobile, as can be deduced from

their blurred appearance in the STM images. Extension of the honeycomb structure only occurs after a second annealing process, when part of the free metal surface gets covered with the honeycomb network.

As stated above, once the hexagonal network was formed it was very stable in terms of manipulation of single monomers and in terms of thermal stability. This considerable stability of the hexagonal network together with its commensurability with the Cu surface may be attributed to a combination of resonance assisted hydrogen bonding (RAHB) [196–198] and a strong interaction with the copper support. RAHB designates the amplification effect of a cooperative hydrogen-bond interaction, which leads to increased binding energy if a molecule exhibits hydrogen-bond donor and acceptor functions coupled over a resonant (mesomeric) structure. This means if one of the autocomplementary monomers **1b** has established a hydrogen-bond towards another monomer as a donor (acceptor) partial charge is shifted across the π -orbital of the two imine groups and its ability to act as an acceptor (donor) is increased. An example for RAHB interaction on surfaces is provided by the formation of guanidine quartets stabilized by cooperative hydrogen bonds [199, 200]. RAHB has also been suggested to contribute to the stabilization of Watson-Crick pairs between DNA bases [196]. Inspired by the extraordinary stability of the network we tried to probe its limits and chemically break the network by offering another hydrogen-bond acceptor molecule. The ideal candidate for this purpose most probably is the PTCDA molecule with its carboxyl groups already described above. Therefore PTCDA was subsequently deposited on the sample *after* the standard preparation of the honeycomb network on the Cu(111) sample; with the astonishing result that PTCDA did not break the network even after extensive annealing. Finally, PTCDA desorbed again whereas the DPDI network stayed untouched.

These findings indicate that the highly robust honeycomb networks can conveniently be used as a template to arrange or to trap molecules which can be even larger than the DPDI monomers, as will be shown in following sections.

4.7 XPS Measurements

The idea behind XPS measurements on the DPDI-Cu(111) system was to check, if it would be possible to see any differences in the chemical shift of the nitrogen core levels before and after annealing due to the proposed dehydrogenation of the DPDI molecule. As described in section 2.3, the binding energies of core levels of atoms are influenced by their valence electrons and thus their chemical environment. Since the tautomerization of DPDI takes place on a timescale much slower than the photoemission of electrons, the unoxidized form of DPDI (**1** in Fig. 4.1) should therefore show two different N1s core level binding energies: One for the amine and one for the imine group.

In the upper part of Fig. 4.10 three XPS spectra of the N1s binding energy region are shown, which were recorded in the Nanojunction laboratory of the Paul Scherrer Institute on a SPECS Phoibos 150. All spectra were taken with the Al K_{α} x-ray source because a series of Auger peaks shifts in to this region of binding energy when the Mg anode is used. Trace (a) is the spectrum for the clean Cu(111) sample. Another broad Auger peak is visible in this region, which slightly complicates the evaluation of the data set. Spectra (b) and (c) are recorded from a sample covered with about 0.7 ML of DPDI before and after the annealing process, respectively. Due to the low adsorption cross section of nitrogen and due to the Auger peak in this region, the spectra were taken at a timescale of about 2–3 hours. In order

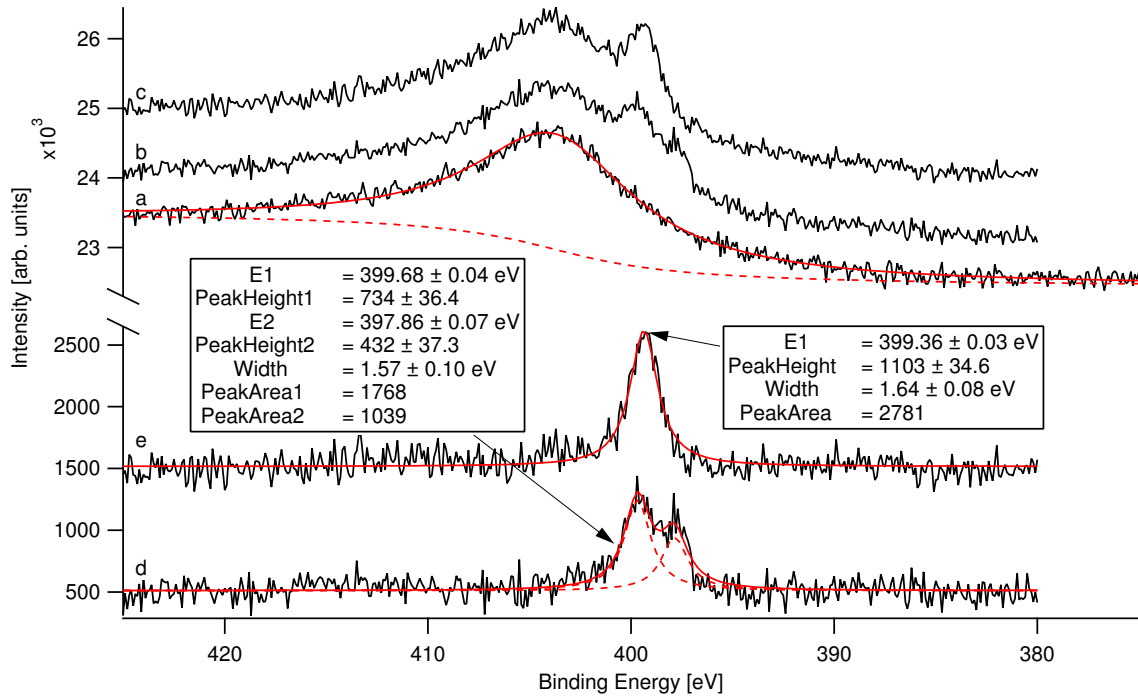


Figure 4.10: XPS spectra of (a) the clean Cu(111) substrate (b) DPDI on Cu(111) before annealing (c) DPDI on Cu(111) after annealing at 300 °C. Traces (d) and (e) show the results of the background subtraction described in the text, applied to traces (b) and (c).

to exclude false interpretation of degradation effects due to beam damage, experiments were therefore done with and without a new sample preparation before the annealing step. The results of both experiments qualitatively showed the same results as presented below.

To avoid a further worsening of the signal to noise ratio, we had to forbear from just subtracting the trace for the clean substrate from the traces for the DPDI covered substrates. Instead, a smooth function was fitted to the shape of the clean background and later on subtracted. In the following the formula used to fit the background and peaks of the XPS data are derived. A measured photoelectron spectrum $M(E)$ as a function of the binding energy E consists of a contribution from a primary function $F(E)$ and a background function $U(E)$:

$$M(E) = F(E) + U(E). \quad (4.3)$$

The background function is mainly caused by secondary electrons which are excited by the emitted photoelectrons during their escape to and from the surface and by the photoelectrons themselves which lost kinetic energy due to these excitations. The definition of the Shirley Background [201]

$$U(E) = \int_0^E F(E')dE' + c \quad (4.4)$$

therefore accounts that only electrons with higher binding energy (lower kinetic energy) of the primary spectrum $F(E)$ can contribute to the background at a certain energy E . With the assumption that the broad Auger peak doesn't deviate strongly from a Lorentzian peak shape

$$Lor(E) = \text{PeakHeight} \cdot \frac{\Gamma^2}{\Gamma^2 + 4 \cdot (E - E_0)^2} \quad (4.5)$$

we can set $F(E) = Lor(E)$ and therefore derive the following analytical expression for the background function $U(E)$ in binding energy scale

$$U(E) = \int_0^E \text{PeakHeight} \cdot \frac{\Gamma^2}{\Gamma^2 + 4 \cdot (E' - E_0)^2} dE' \quad (4.6)$$

$$= \int_0^E \text{PeakHeight} \cdot \frac{1}{1 + \left[\frac{2(E' - E_0)}{\Gamma}\right]^2} dE' = \text{PeakHeight} \cdot \left[\frac{\Gamma}{2} \arctan \frac{2(E' - E_0)}{\Gamma} \right]_0^E \quad (4.7)$$

$$= \text{PeakHeight} \cdot \left(\frac{\Gamma}{2} \arctan \frac{2(E - E_0)}{\Gamma} + 0 \right). \quad (4.8)$$

With E_0 being the position, PeakHeight the height and Γ the full width at half maximum (FWHM) of the peak. Altogether the analytical fit function for the measured spectrum $M(E)$ of the clean Cu(111) substrate becomes

$$M(E) = \text{PeakHeight} \cdot \frac{\Gamma^2}{\Gamma^2 + 4 \cdot (E - E_0)^2} + \text{Yield} \cdot \text{PeakHeight} \cdot \frac{\Gamma}{2} \arctan \frac{2(E - E_0)}{\Gamma} + \text{BgOffset} \quad (4.9)$$

where Yield is a factor representing the secondary electron yield and BgOffset is a constant background factor due to other features in the spectrum and the usual detector background.

After fitting equation 4.9 to trace (a) of Figure 4.10, the resulting function was scaled with a linear prefactor to fit traces (b) and (c). After subtracting these functions the N1s peaks are clearly visible and it was tried to fit the actual N1s peaks to a product of a Gaussian and Lorentzian peak with the mixing parameter m

$$\text{GaussLor}(E) = \text{PeakHeight} \cdot e^{-4 \cdot (1-m) \ln 2 \frac{(E-E_0)^2}{\Gamma_G^2}} \cdot \frac{1}{1 + 4 \cdot m \frac{(E-E_0)^2}{\Gamma_L^2}}. \quad (4.10)$$

But the signal to noise ratio was not good enough and the two additional fit parameters therefore lead to a strong fit dependence on the initial values. Therefore, only Gaussian shaped peaks were fitted to the data.

In trace (d) (DPDI/Cu(111) before annealing) the two peaks at positions $E_1 = 399.68$ eV and $E_2 = 397.86$ eV are clearly visible, whereas after annealing (trace (e)) only the peak at $E_1 = 399.36$ eV is left. The value of the intensity/peak area (before: PeakArea1 = 1768, after annealing: PeakArea1 = 2781) increased by approximately the amount of the peak area of the vanished peak from trace (d) (PeakArea2 = 1039). This observation further corroborates the suggested dehydrogenation model set up earlier. Before annealing the different chemical shifts for the imine and amine nitrogen atoms lead to the observed splitting of the N1s peak due to the different constitution of the valence orbitals around the nitrogen atoms. After annealing at 300 °C, where the dehydrogenation of DPDI is induced, the end groups of the resulting molecule (**1b** in Fig. 4.1) are only imine groups and therefore only one chemical surrounding of the nitrogen atoms exists in the self-assembled structure (Fig. 4.7). For calculation of the exact chemical shift, or better the N1s core level binding energy, a very demanding ab initio density functional calculation with a core hole pseudo-potential is necessary. However, the known [202] electronegativities of hydrogen, carbon and nitrogen rationalize the chemical shifts observed with a simplified chemist's model of the photoemission process.

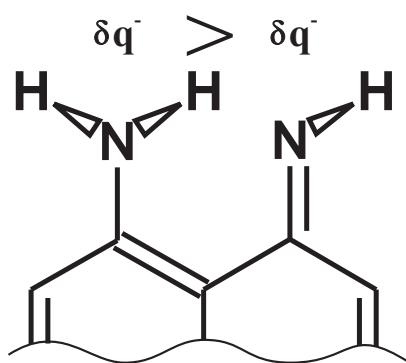


Figure 4.11: Chemical shift of N in amine and imine groups. Due to the different electronegativities of the elements the partial charge of N in an amine group is slightly more negative than in an imine group.

The Pauling electronegativities χ_P [203] for N, C and H are 3.04, 2.55 and 2.20, respectively. Thus, of the 3 electron pairs involved in the covalent binding of the N atom in the amine group, the 2 electron pairs towards the H atoms are attracted strongly towards the N due to the high electronegativity difference of $\Delta\chi_P = 0.84$ between N and H. Since the difference $\Delta\chi_P = 0.49$ between C and N is lower compared to N and H, the covalent bond towards the C atom is less asymmetric. An imine group features a single N–H bond and a double bond between C and N. Like the C–N single bond, this double bond is rather symmetrically spread between C and N, and the valence electron density around the imine N is therefore lower, than in the amine group (see Fig. 4.11). For a photoelectron which is emitted from an unperturbed N1s core level less energy to leave the nitrogen atom of the amine group, since it is repelled by a higher valence electron density, compared to the imine group. Consequently, the binding energy of the N1s core level of the amine group should be lower than the one of the imine group. With this line of argument our findings are consistent with the proposed dehydrogenation model, because the N1s peak which remains after annealing is the one at higher binding energy - and thus the one of the imine end group.

In principle one would also expect different chemical shifts for the core levels of the carbon atoms of DPDI. Before annealing the stoichiometry of the chemically different carbon atoms is 2 : 2 : 8 : 8 as can be deduced from Fig. 4.1. After annealing this stoichiometry should be changed to 4 : 8 : 8, giving a ratio of 1 : 2 : 2 for the strong C1s peak. Unfortunately, no splitting of the carbon peak could be observed with our lab based XPS setup. Nevertheless, this is not a contradiction to the above statements, as the expected chemical shift would be small due to the smaller electronegativity difference of nitrogen and carbon. Additionally, all carbon atoms of DPDI are part of the large large π -system. The influence of the valence orbitals on the carbon core levels is hence further smeared out.

4.8 Co-adsorbed Mixtures of DPDI and PTCDA

If PTCDA was deposited after the hexagonal network was formed by annealing at 300 °C, it was not able to break the network and incorporate itself, as already stated in section 4.6. This is different for a co-adsorption of DPDI and PTCDA on Cu(111). Such a sample was prepared by first depositing DPDI and then directly afterwards, while DPDI is still in its

highly mobile precursor form **1**, PTCDA was deposited. The results of such an approach are presented in Fig. 4.12.

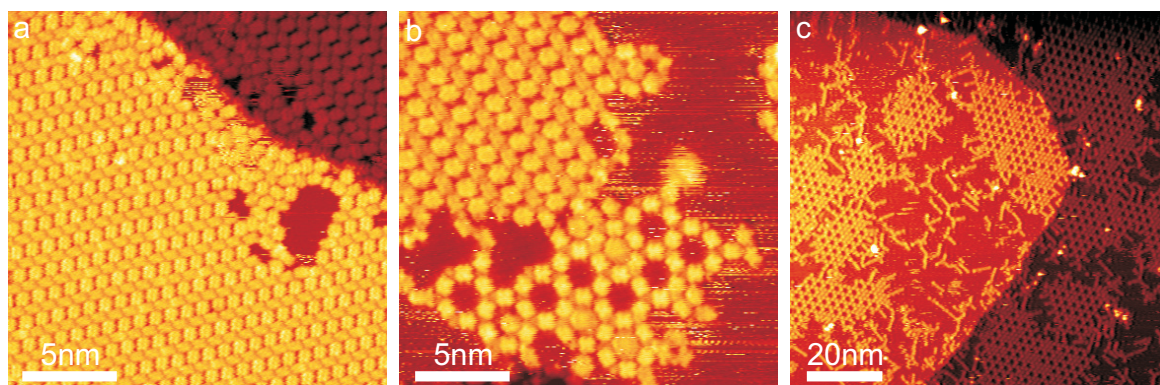


Figure 4.12: STM images of a mixture of DPDI and PTCDA (ratio about 1 : 1) co-adsorbed on Cu(111). All images show the same sample at different phases of sample preparation: (a) not annealed ($I = 14$ pA, $U = -1.8$ V) (b) after annealing at 300 °C ($I = 16$ pA, $U = -2.07$ V) and (c) after annealing at 358 °C ($I = 19$ pA, $U = -2.28$ V).

As can be seen from Fig. 4.12 a, DPDI and PTCDA intermix and form a ladder like structure, with the rungs or crossbars of the ladder appearing brighter and larger than the molecules forming the stand of the ladder. Because we have yet not been able to carry out useful LEED measurements of this sample the exact parameters for the unit cell could not be deduced. From some STM images it looks as if the unit cell of this structure is slightly rhombic or that the rung molecules are slightly distorted from a perpendicular orientation with regard to the stand molecules. Based on the initial idea to covalently link the constituent molecules of a self-assembly, the sample was annealed in order to induce a polycondensation reaction between DPDI and PTCDA under the release of H_2O . However, after annealing the sample at 300 °C the ladder structure persisted unchanged (Fig. 4.12 b). Due to the temperature treatment some of the DPDI molecules were converted to their autocomplementary species **1b** and thus started to nucleate occasionally to the already presented honeycomb structure. Fortunately, a sample area was found where the honeycomb structure directly evolves out of a ladder structure and it is therefore possible to identify the individual molecules in the intermixed structure. According to Fig. 4.12 b, the stand of the ladder is made up of DPDI molecules and the rungs are made up from PTCDA molecules. To assign PTCDA the brighter and larger appearance is also consistent with geometrical considerations, because the anhydride end groups of PTCDA are bigger than the imine and amine groups of DPDI. Further annealing of the same sample at 358 °C led to the desorption of PTCDA and left the sample covered with many DPDI honeycomb islands (Fig. 4.12 c).

Such intermixing experiments (including LEED) of DPDI and PTCDA were also performed on Ag(111) and a variety of different assemblies were found depending on the ratio between DPDI and PTCDA. However, these results are better discussed together with new Scanning Tunneling Spectroscopy (STS) based investigations of my project successor Manfred Matena and are therefore not included in this thesis.

Similar self-intermixed bi-molecular assemblies will most probably become of great importance to any type of application as e.g. molecular electronics and were already studied earlier in the Nanolab by de Wild et al. [155, 204].

4.9 Trapping Subsequently Deposited Molecules

The far most evident application of a porous and very stable honeycomb network as the one formed by DPDI is the possibility to trap other molecules inside. The feasibility of such a trapping was already shown for the subsequent deposition of DPDI in Fig. 4.9. However, the most obvious choice of a molecule to be trapped inside cavities is the fullerene C_{60} molecule (Fig. 4.13) as shown recently by Theobald et al. [160, 205]. After its discovery in 1985 [206] and after the emergence of efficient methods for its synthesis [207], it is one of the best known molecules in terms of adsorption on surfaces and thin film growth to date. To a large extent this is partially due to the fact that the handling of C_{60} under UHV conditions is straight forward. Additionally, C_{60} was successfully used for different types of positioning experiments on the surface with the STM tip [208, 209] and even an electromechanical amplifier was demonstrated [210, 211]. By pressing a C_{60} molecule with the metallic tip of the STM a small force is applied, which distorts the molecule and thereby shifts the molecular orbital energy levels. This shift modulates the tunneling current through the C_{60} and can thus be used as an amplifier.

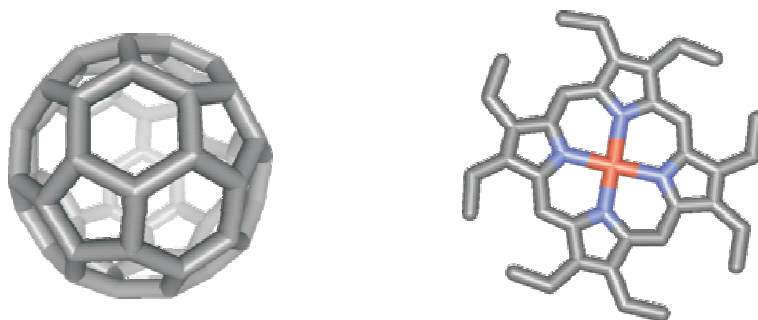


Figure 4.13: Stick model of C_{60} (left) and OEP (right).

Another class of well studied molecules in surface science in general and specifically in STM investigations are porphyrin molecules and their derivatives. A porphyrin is a heterocyclic macrocycle made from 4 pyrrole subunits linked on opposite sides (α position) through 4 methine bridges. In the inner cavity formed by the 4 N atoms a center metal atom can be inserted via coordination bonding. An interesting feature of porphyrin molecules is the fact that organic synthesis is very advanced for these molecules. Therefore, a number of porphyrins with different metal atoms in the center or different peripheral substituents are commercially available. For example, porphyrins to which four ditertbutylphenyl substituents were attached have been successfully used for the first controlled lateral manipulation of molecules at room-temperature [212]. During our studies it turned out that octaethylporphyrins (OEP)(Fig. 4.13 right), whose substituents consist of ethyl legs, fit conveniently in the cavities formed by the DPDI honeycomb network. Both OEPs with a Cu and a Zn center metal ion were used for trapping experiments. However, both OEPs show the same behaviour for these experiments since their size, the relevant feature for trapping, is equal and from now on are not distinguished anymore.

4.9.1 C₆₀ and OEP at Room-temperature

Fig. 4.14 shows STM images of C₆₀ and OEP subsequently deposited on the previously prepared honeycomb network. Both, C₆₀ and OEP, are trapped and statistically distributed in the network, but still show some mobility inside the pores. This can be seen from the partially disrupted zig-zag appearance of the C₆₀ inside the cavities along the slow scanning direction. This appearance is due to temperature activated or induced molecular motion while the STM tip is scanning across the surface. Nevertheless, the C₆₀ cannot escape from one cavity to another. It is known that a large charge transfer (about 0.8 e⁻) from the metal substrate to C₆₀ takes place [213] which leads to a strong interaction with the surface. Therefore the probability for a C₆₀ to jump from one pore (energetic minimum) to another is low across the high energy barrier formed by the cavity walls of the DPDI network.

Such a confined mobility inside a pore can also be observed for OEP. The blurred appearance of the OEP is a clear indication that still considerable movement exists, as e.g. the rotation or translation of the whole molecule. Furthermore, the motion can be also due to a wobbling or breathing motion of the legs. One might object that the blurred appearance of OEP is its intrinsic STM appearance, but from earlier studies of Luca Ramoino [67] and from experiments at low temperature we know that it is possible to resolve the eight ethyl legs of OEP.

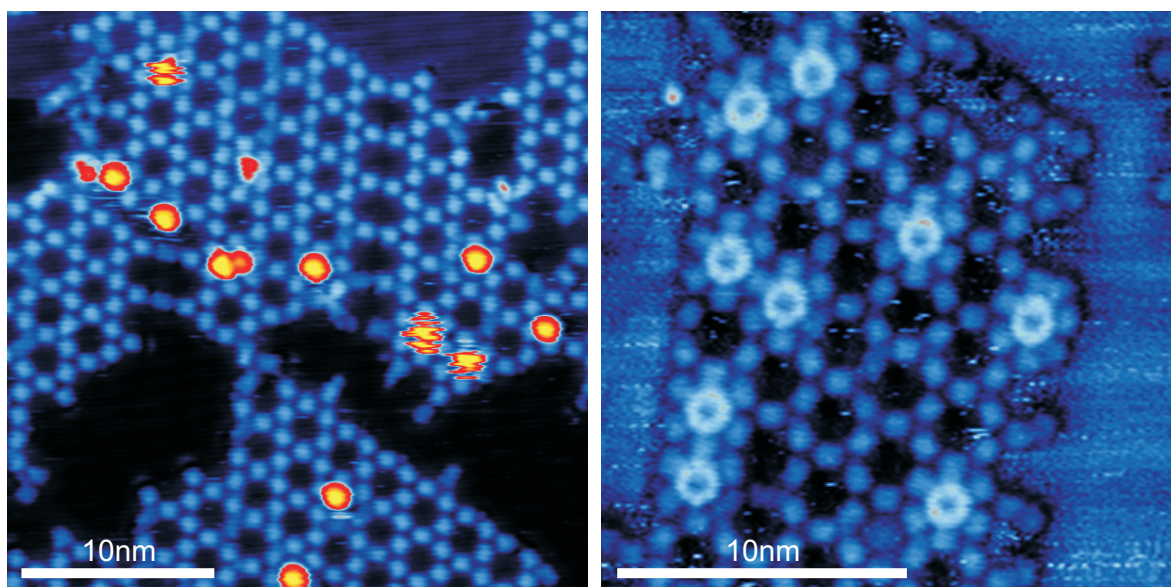


Figure 4.14: (left) STM image ($I = 30$ pA, $U = -1.56$ V) of C₆₀ trapped in the DPDI honeycomb network on Cu(111) at room-temperature. (right) STM image ($I = 20$ pA, $U = -1.1$ V) of OEP trapped in the DPDI honeycomb network on Cu(111) at room-temperature.

Outside the honeycomb network, however, the behaviour of C₆₀ and OEP differs. The OEP molecules which are not trapped inside the honeycomb network give rise to a mobile 2D gas phase on the bare metal surface. Like the subsequent deposition of unreacted DPDI molecules presented in Fig. 4.9 b of section 4.6 this mobile phase is imaged as a characteristic streak noise pattern (compare the area outside the network in Fig. 4.14 right with the one in Fig. 4.9 b). The mobile phase of OEP on Cu is well in line with earlier findings of Ramoino [67] and is a clear sign for small attractive interaction between adsorbed OEP molecules. In contrast, C₆₀ exhibits high attractive molecule-molecule interactions, because it does not fill a mobile phase

but instead C_{60} forms islands on Cu(111) [214] (also compare Fig. 4.15 in the following section). These strong molecule-molecule interactions of C_{60} originate from its frontier π -orbitals which extend out of the carbon cage and lead to significant attractive van-der-Waals interactions due to polarization fluctuation waves on the molecule [215]. Therefore no streak noise is observable in Fig. 4.14 left and one can image the bare metal surface outside the network.

4.9.2 C_{60} and OEP at 77 K

Versus the end of my thesis, we received a commercial low-temperature STM from Omicron and therefore had the possibility to do low temperature experiments. Samples which were prepared in the same way as described in the previous section were investigated with this instrument at 77 K—liquid nitrogen temperature. The resulting STM images are shown in Fig. 4.15 and interesting features are visible on these two images.

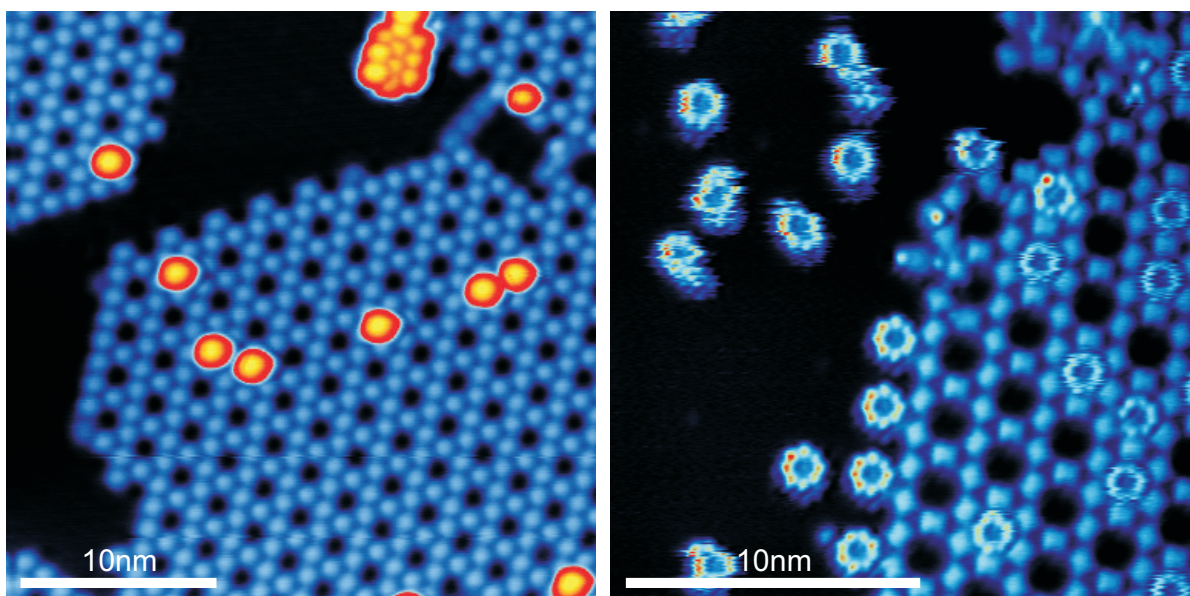


Figure 4.15: (left) STM image ($I = 50$ pA, $U = -0.40$ V) of C_{60} trapped in the DPDI honeycomb network on Cu(111) at 77 K. (right) STM image ($I = 25$ pA, $U = -1.55$ V) of OEP in the DPDI honeycomb network on Cu(111) at 77 K.

The STM image of subsequently deposited C_{60} molecules shows a small island of about 10 C_{60} molecules assembled in the typical hexagonal close packed pattern. This visually confirms the statement made earlier about the attractive molecule-molecule interaction of C_{60} . The molecules trapped inside the cavities of the network do not show a zig-zag appearance anymore at these low temperatures. Probably, the dragging effect of the STM tip is only possible for C_{60} molecules already slightly excited by the coupling to the phonon bath of the substrate at room-temperature.

In the case of OEP, whose intermolecular interaction is rather weak, the diffusive process of the OEP molecules on the free metal area is nearly frozen and single molecules are visible at 77 K. Again the zig-zag appearance of these molecules indicates that they are still mobile. However, some OEP molecules are pinned at the edges of the hexagonal DPDI islands and their eight ethyl legs are nicely visible. Since pinning is mainly observed at the linking position

of two marginal **1b** monomers, it is probable that hydrogen bonding towards the ethyl legs is involved in this interaction. The fuzzy appearance of the OEPs trapped in the network indicates that the OEP molecules still have a considerable mobility inside the pores.

4.9.3 OEP Switching

It can be interesting to access the properties of molecules with low molecule-molecule interactions trapped in the porous network since those measurements would not be possible without trapping due to their high mobility as shown in the previous section.

If the tip of the STM is laterally placed above a trapped OEP molecule and the height signal is recorded with the feedback loop turned on, a bi-state signal is observed. Such a signal is shown in Fig. 4.16 left with a time resolution of 20 ms for each data point. Clearly distinct from the inherent noise level of the STM, the rising and falling edges of switches between two fixed heights are visible. Depending on the exact position of the tip and the tunneling conditions the height difference between the two plateaus is about 0.05–0.10 Å. These switching events can be best observed if the tip is placed a little bit off center of the OEP, above the ring of legs of the molecule. If the feedback loop of the STM tip is switched off and the z -height is held constant the switching behaviour consequently appears in the current signal. This fact assures that the measured features are not just artefacts of the feedback loop. However, an influence of the response parameters of the loop on the observed height difference is not excluded.

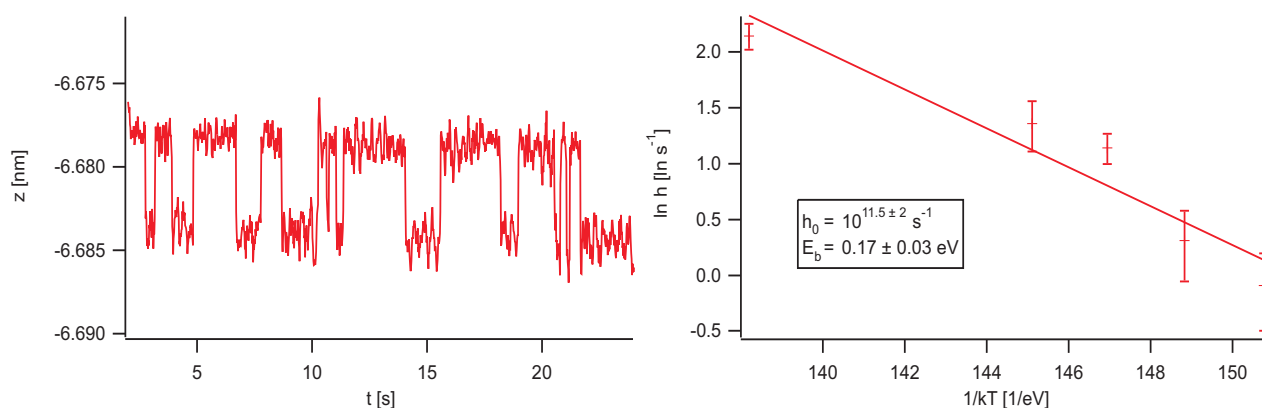


Figure 4.16: Observation of small molecular motion of trapped OEP. (left) Bi-state z -signal plotted against time while the tip was placed above a trapped OEP molecule at $I = 20 \text{ pA}$ and $U = -1.5 \text{ V}$. (right) Arrhenius plot of the number of switching events per second for the determination of the energy barrier and of the exponential prefactor.

On the basis of these observations, one might speculate that the OEP molecule with its eight ethyl legs rotates (bi-directional or uni-directional) in the DPDI pores and thus the ethyl legs cause the difference in height and conductivity respectively. If a rotation of the molecule is assumed the DPDI network would then represent a stator with a six-fold symmetry and the OEP would represent the anchor with a four-fold symmetry. However, the zig-zag appearance of trapped OEP molecules at these temperatures (Fig. 4.15 right) suggests that the OEP molecules are slightly smaller than the DPDI cavities and therefore have the possibility to carry out translational movements. Also, wobbling or breathing motions of the OEP molecules

are imaginable. Anyhow, without further information or experiments the underlying motion will stay subject to speculations. A possible solution would be to preform the same experiment with ethylporphyrins which, instead of eight ethyl legs, do have a reduced number of legs preferably distributed in an asymmetric way around the porphyrin core. This could help to clearly identify an induced uni-directional rotation.

Since the experiments in this section were done with the Omicron LT STM we had the possibility to counter heat and perform measurements at different temperatures. After these were carried out, the average number of switching events per second were counted manually from the measured signals and the results are shown in the Arrhenius plot in Fig. 4.16 right.

As already described in chapter 2 the temperature dependence of the attempt frequency h for a diffusive process follows an exponential law

$$h = h_0 e^{-\frac{E_D}{k_B T}}, \quad (4.11)$$

where h_0 is the so-called pre-exponential constant and E_D is the activation energy barrier. By taking the logarithm of equation 4.11, it follows the standard function of an Arrhenius plot

$$\ln h = \ln h_0 - \frac{E_D}{k_B T}, \quad (4.12)$$

in which $\ln h$ is plotted against $1/k_B T$. The slope of the Arrhenius plot in Fig. 4.16 right therefore corresponds to the energy barrier $E_D = 0.17 \pm 0.03$ eV. The cut with the ordinate axis determines the pre-exponential constant of the attempt frequency to $10^{11.5 \pm 2} \text{ s}^{-1}$. The energy barrier and especially the pre-exponential constant are probably underestimated. This is because at elevated temperatures (lower $1/k_B T$ values) switching events are missed due to the time resolution of the loop signal and because it gets more and more difficult to distinguish switching events from random noise of the signal.

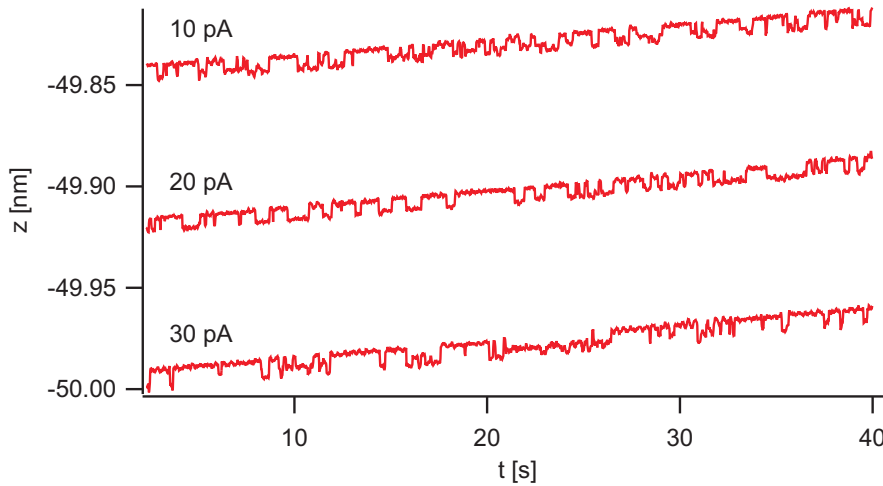


Figure 4.17: Bi-state z -signal of an individual OEP molecule at 80 K trapped in the network plotted against time for different current setpoints as indicated and a bias voltage of -1.5 V. From the curves a tip-induced slow-down of the molecular motion can be deduced.

As a final remark to these observations Fig. 4.17 shows the z -signal of an experiment at 80 K in which the lateral tip position and the bias voltage were kept constant. In this experiment

the current setpoint of the feedback loop was changed from 30 pA to 20 pA and finally to 10 pA. Reasonably, the tip is further retracted (higher z values) for lower setpoints. The minimal slope of the curves is due to thermal drift caused by the counter heating of the STM. Interestingly, the signal at higher setpoints (smaller tip-sample distance) shows less falling and rising edges, which indicates a slow down of the OEP motion under the increased tip influence. Unfortunately, this effect is not very prominent and cannot be regarded as a typical result yet. But additional experiments with an emphasis on this effect should provide clarification.

4.9.4 Manipulation

Manipulation of single atoms and molecules is the ultimate application reserved to STM or Scanning Probe Microscopes alone. First presented by J.A. Stroscio and D.M. Eigler [216], the new and fascinating approach to use the tip of an STM to move or otherwise manipulate single atoms and molecules soon became a general tool. The STM tip was even used to induce chemical reactions as e.g. the Ullman reaction [217]. For an overview of all the manipulations already realized the interested reader is referred to two reviews [218, 219] which concentrate on manipulation of larger molecules. In our case it was interesting to figure out if and how trapped molecules could be moved from one pore in the DPDI network to another.

Fig. 4.18 summarizes a series of controlled manipulation events. These manipulations were carried out by switching off the feedback system and setting a negative tip lift value of 0.40 nm. This means that once the feedback is switched off the tip is approached 0.40 nm towards the sample surface. Herein, this distance is measured relative to the initial z -height, which is defined by the combination of current setpoint and bias voltage. Therefore the reproducibility of the manipulation is assured. The pushing motion along the directions of the arrows in Fig. 4.18 results in lateral positioning events of the C_{60} molecules from one pore to another. This can be best seen by comparing image 4 and 5 of the sequence in which the central C_{60} is manipulated into the pore to the lower right.

Normally, the feedback system is switched off while the tip is placed above an empty pore in front of the molecule which is going to be pushed. However, if the tip is placed directly above a C_{60} molecule and the loop is turned off, the tip might occasionally pick up the molecule. This perpendicular picking of a molecule can be followed in the current and height signals, because they change their characteristic noise when the molecule is picked up. Going back to scanning mode and recording an image gives a fuzzy looking image, as can be seen in image number 3 in Fig. 4.18. This is due to the modification of the tip by the C_{60} molecule at its apex. The cross inside image 3 presents the position where the tip was placed after the completion of the image scan and the same procedure (switching off feedback several times) was used to place the C_{60} molecule.

The series of STM images in Fig. 4.19 shows how such a C_{60} manipulation can be used to fabricate a model system of a ball-bearing. The sequence shows how a C_{60} molecule is moved on top of a OEP molecule. This bi-molecular system can be imagined as solid ball supported by the eight ethyl legs of OEP. However, this construct is not very stable and difficult to prepare as can be seen by the failed try from image 5 to 6.

The biggest difficulties of such positioning experiments is the fact that one does not have the possibility to manipulate and image at the same time. Due to thermal drift and the time-lapse approach of taking snapshot images before and after positioning events the experimentator is left in a situation where he/she does not have a realtime feedback about the current status of the surface while manipulating. However, the forcefeedback system currently developed by

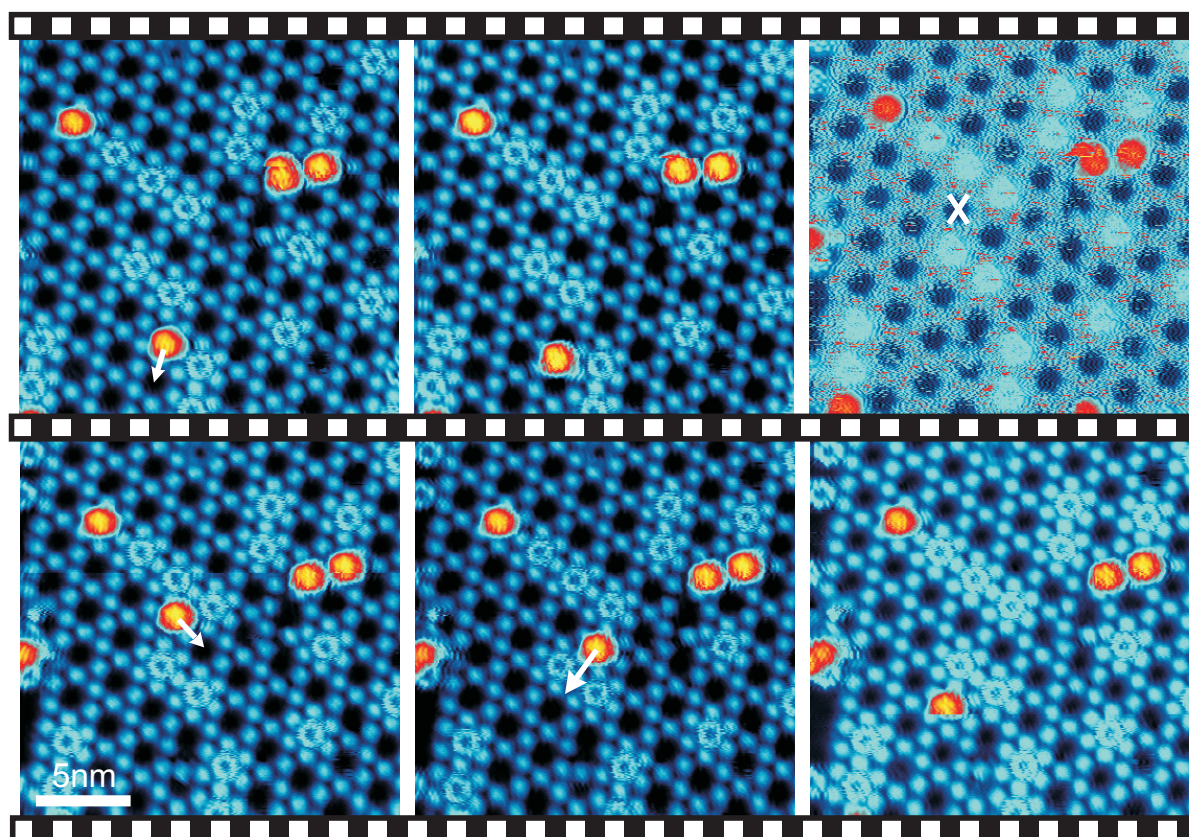


Figure 4.18: Sequence of STM images ($I = 90 \text{ pA}$, $U = -0.47 \text{ V}$) recorded during a series of manipulation events of trapped C_{60} and OEP inside a DPDI honeycomb network at 77 K . The arrows indicate the movement of the STM tip, which was approached 0.40 nm to the surface while the feedback loop was turned off. The 3rd image of the sequence was recorded with a C_{60} attached to the tip apex which was previously picked up in the lower part of image 2. After completion of the scan of image number 3 the C_{60} molecule was successfully dropped at the position marked with an X.

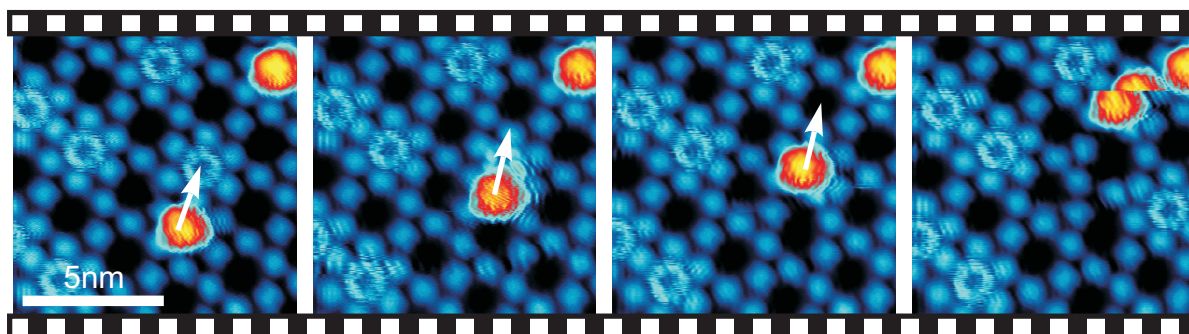


Figure 4.19: Sequence of STM images ($I = 90 \text{ pA}$, $U = -0.47 \text{ V}$) recorded during a series of manipulation events of trapped C_{60} and OEP inside a DPDI honeycomb network at 77 K . The arrows indicate the movement of the STM tip, whose feedback loop was turned off and which was lowered 0.40 nm to the surface in manipulation mode. By moving a C_{60} molecule on top of a OEP molecule the fabrication of a model system for a molecular ball-bearing is shown.

Nanonis in collaboration with the Nanolab might help to overcome these difficulties. Herein, a forcefeedback joystick is coupled to the feedback loop of the STM tip in order to control the movement of the tip in all 3 dimensions. Additionally, the error signal of the current is fed to a forcefeedback system of the joystick which consists of several little electric motors. If the tip is lowered to the surface the error signal becomes large and the counter force exerted on the joystick is increased. The experimentator manipulating the joystick therefore has the perception to *feel* the surface and adsorbates during positioning events. In the case of AFM this analogy is not far fetched, because the forces exerted on the AFM cantilever can be scaled and fed to the forcefeedback system.

4.10 Conclusions and Outlook

In conclusion, the deposition of 4,9-diaminoperylene-quinone-3,10-diimine **1** on a metal surface provides highly mobile submonolayer phases due to the impossibility of significant intermolecular interactions in two dimensions. However, thermally activated dehydrogenation leads to **1b** which is autocomplementary and serves both as an H-bond donor and acceptor. This irreversibly leads to well-defined polymeric structures which can be controlled by the typical diffusion length between the activation of the precursor and its "polymerization" which in turn is controlled through different amounts of initial monomer coverage. This reactive self-assembly represents a "surface dilution principle" akin to the dilution principle in chemical synthesis [220–222]. The connectivity and the resulting dimensionality of the aggregates may be varied between 0D for the trimers and 2D for the hexagonal network. Once formed, these molecular surface assemblies are highly robust and therefore suitable for the construction of hierarchic structures by self-organization of subsequently deposited material.

The results presented for the successful trapping of C₆₀ and OEP molecules in this thesis demonstrated the feasibility of such an approach and opened new possibilities for the investigation of single molecules which normally would not be accessible due to their high mobility at RT. As an example, the residual mobility of trapped OEP at 77 K gave rise to a bi-state current or *z*-signal, respectively. This bi-state behaviour was recorded by placing the STM tip above such a molecule. The energy barrier E_D and the pre-exponential constant of the attempt frequencies were determined for such a system by taking data at various temperatures. For the first time, thermal excitations of molecular vibrations or motions within a supramolecular lateral confinement were investigated by STM. Since we have the possibility to confine different molecules inside the cavities, we might be able to probe individual degrees of freedom of single molecules. Such experiments with molecular systems may lateron help to understand the kinetics and thermodynamics of small devices.

Finally, lateral and perpendicular manipulation of C₆₀ molecules from one pore to another was presented. The construction of a model system for a bi-molecular ball-bearing was achieved by controlled manipulation of a C₆₀ molecule onto an OEP molecule.

In order to gain more insight into the mechanism involved in the reaction process and especially to better understand the reason for the strong resonance-assisted hydrogen-bonding (RAHB) of the hexagonal network, ab-initio calculations have been initiated in collaboration with the group of Prof. R. de Felice from Modena, Italy. Therefore, X-ray standing wavefield (XSW) measurements [223, 224] were carried out at the European Synchrotron Radiation Facility (ESRF) in Grenoble, France. The data analysis is still in progress and the results are thus not presented. The XSW method uses the nodes and antinodes of an X-ray standing

wavefield above a perfect single crystal as a ruler to determine the adsorption height of an adsorbate. This value is most interesting for theoretical ab-initio calculations of adsorbates on surfaces since it allows the verification of the overall accuracy of density functional theory (DFT) calculations. Intrinsically to DFT, van-der-Waals forces, which are a major contribution to the interaction of the adsorbate with the substrate, are not included in such calculations. With the help of the experimentally determined adsorption height the exchange correlation approximations of DFT can then be tuned to match this height.

Other ongoing work towards a deeper understanding of the DPDI system are STS measurements, which are carried out on the PTCDA and DPDI mixtures on Ag(111). In combination with ab-initio calculations these measurements might help to elucidate the bonding mechanisms between DPDI and PTCDA in the ladder structure also observed on Cu(111).

Bibliography

- [1] G.A. Somorjai, *Introduction to Surface Chemistry and Catalysis*, John Wiles & Sons, New York (1994).
- [2] F. Zaera, *Probing catalytic reactions at surfaces*, Prog. Surf. Sci. **69**, 1–98 (2001).
- [3] H. S. Taylor, *A theory of the catalytic surface*, Proceedings of the Royal Society of London Series A **108**, 105–111 (1925).
- [4] T. A. Jung, R. R. Schlittler, and J. K. Gimzewski, *Conformational identification of individual adsorbed molecules with the STM*, Nature **386**, 696–698 (1997).
- [5] Z. Ma and F. Zaera, *Organic chemistry on solid surfaces*, Surf. Sci. Rep. **61**, 229–281 (2006).
- [6] A. Aviram and M. A. Ratner, *Molecular rectifiers*, Chem. Phys. Lett. **29**, 277–283 (1974).
- [7] R.P. Feynman, *There's plenty of room at the bottom*, Eng. Sci. **23**, 22–36 (1960).
- [8] J. V. Barth, G. Costantini, and K. Kern, *Engineering atomic and molecular nanostructures at surfaces*, Nature **437**, 671–679 (2005).
- [9] G. Binnig and H. Rohrer, *Scanning tunneling microscopy*, Helvetica Physica Acta **55**, 762 (1982).
- [10] C. J. Chen, *Introduction to Scanning Tunneling Microscopy*, Oxford University Press (1993).
- [11] R. Wiesendanger and H.-J. Güntherodt, *Introduction to Scanning Tunneling Microscopy*, Springer-Verlag (1996).
- [12] D. Drakova, *Theoretical modelling of scanning tunneling microscopy, scanning tunneling spectroscopy and atomic force microscopy*, Reports on Progress in Physics **64**, 205 (2001).
- [13] J. Bardeen, *Tunneling from a many-particle point of view*, Phys. Rev. Lett. **6**, 57 (1961).
- [14] J. Tersoff and D. R. Hamann, *Theory and Application for the Scanning Tunneling Microscope*, Phys. Rev. Lett. **50**, 1998 (1983).
- [15] J. Tersoff and D. R. Hamann, *Theory of the scanning tunneling microscope*, Phys. Rev. B **31**, 805 (1985).
- [16] L.D. Landau and L.M. Lifschitz, *Quantum mechanics*, Pergamon Press, Oxford, 3rd ed. (1977).

- [17] A. D. Gottlieb and L. Wesoloski, *Bardeen's tunnelling theory as applied to scanning tunnelling microscopy: a technical guide to the traditional interpretation*, *Nanotechnology* **17**, R57–R65 (2006).
- [18] J. Wintterlin, R. Schuster, and G. Ertl, *Existence of a "hot" atom mechanism for the dissociation of O₂ on Pt(111)*, *Phys. Rev. Lett.* **77**, 123–126 (1996).
- [19] T. Zambelli, J. V. Barth, J. Wintterlin, and G. Ertl, *Complex pathways in dissociative adsorption of oxygen on platinum*, *Nature* **390**, 495–497 (1997).
- [20] G. Meyer, B. Neu, and K. H. Rieder, *Controlled lateral manipulation of single molecules with the Scanning Tunneling Microscope*, *Appl. Phys. A: Mater. Sci. Process.* **60**, 343–345 (1995).
- [21] S. Zöphel, J. Repp, G. Meyer, and K. H. Rieder, *Determination of binding sites in ordered phases of CO/Cu(211) employing molecular level manipulation*, *Chem. Phys. Lett.* **310**, 145–149 (1999).
- [22] J. K. Gimzewski, T. A. Jung, M. T. Cuberes, and R. R. Schlittler, *Scanning tunneling microscopy of individual molecules: beyond imaging*, *Surf. Sci.* **386**, 101–114 (1997).
- [23] J. K. Gimzewski, E. Stoll, and R. R. Schlitter, *Scanning tunneling microscopy of individual molecules of copper phthalocyanine adsorbed on polycrystalline silver surfaces*, *Surf. Sci.* **181**, 267–277 (1987).
- [24] H. Ohtani, R. J. Wilson, S. Chiang, and C. M. Mate, *Scanning tunneling microscopy observations of benzene molecules on the Rh(111)-(3X3)(C₆H₆+2CO) surface*, *Phys. Rev. Lett.* **60**, 2398–2401 (1988).
- [25] T. Sleator and R. Tycko, *Observation of individual organic-molecules at a crystal-surface with use of a scanning tunneling microscope*, *Phys. Rev. Lett.* **60**, 1418–1421 (1988).
- [26] P. H. Lippel, R. J. Wilson, M. D. Miller, C. Wöll, and S. Chiang, *High-resolution imaging of copper-phthalocyanine by scanning-tunneling microscopy*, *Phys. Rev. Lett.* **62**, 171–174 (1989).
- [27] B. I. Lundqvist, O. Gunnarsson, H. Hjelmberg, and J. K. Norskov, *Theoretical description of molecules-metal interaction and surface-reactions*, *Surf. Sci.* **89**, 196–225 (1979).
- [28] B. Hammer and J. K. Norskov, *Theoretical surface science and catalysis: Calculations and concepts*, *Adv. Catal.* **45**, 71–129 (2000).
- [29] N. D. Lang, *Vacuum tunneling current from an adsorbed atom*, *Phys. Rev. Lett.* **55**, 230–233 (1985).
- [30] N. D. Lang, *Theory of single-atom imaging in the scanning tunneling microscope*, *Phys. Rev. Lett.* **56**, 1164–1167 (1986).
- [31] D. M. Eigler, P. S. Weiss, E. K. Schweizer, and N. D. Lang, *Imaging Xe with a low-temperature scanning tunneling microscope*, *Phys. Rev. Lett.* **66**, 1189–1192 (1991).

- [32] P. Sautet, *Atomic adsorbate identification with the STM: A theoretical approach*, Surf. Sci. **374**, 406–417 (1997).
- [33] I. S. Tilinin, M. K. Rose, J. C. Dunphy, M. Salmeron, and M. A. Van Hove, *Identification of adatoms on metal surfaces by STM: experiment and theory*, Surf. Sci. **418**, 511–520 (1998).
- [34] P. Sautet and C. Joachim, *Electronic transmission coefficient for the single-impurity problem in the scattering-matrix approach*, Phys. Rev. B **38**, 12238–12247 (1988).
- [35] P. S. Weiss and D. M. Eigler, *Site dependence of the apparent shape of a molecule in scanning tunneling microscope images - benzene on Pt(111)*, Phys. Rev. Lett. **71**, 3139–3142 (1993).
- [36] P. Sautet and M. L. Bocquet, *Shape of molecular adsorbates in STM images: A theoretical study of benzene on Pt(111)*, Phys. Rev. B **53**, 4910–4925 (1996).
- [37] P. Sautet, *Images of adsorbates with the scanning tunneling microscope: Theoretical approaches to the contrast mechanism*, Chem. Rev. **97**, 1097–1116 (1997).
- [38] X. C. Guo and R. J. Madix, *Real-time observation of surface reactivity and mobility with scanning tunneling microscopy*, Acc. Chem. Res. **36**, 471–480 (2003).
- [39] S. Berner, M. Brunner, L. Ramoino, H. Suzuki, H. J. Güntherodt, and T. A. Jung, *Time evolution analysis of a 2D solid-gas equilibrium: a model system for molecular adsorption and diffusion*, Chem. Phys. Lett. **348**, 175–181 (2001).
- [40] R. Schaub, E. Wahlström, A. Ronnau, E. Laegsgaard, I. Stensgaard, and F. Besenbacher, *Oxygen-mediated diffusion of oxygen vacancies on the TiO₂(110) surface*, Science **299**, 377–379 (2003).
- [41] T. R. Linderoth, S. Horch, E. Laegsgaard, I. Stensgaard, and F. Besenbacher, *Surface diffusion of Pt on Pt(110): Arrhenius behavior of long jumps*, Phys. Rev. Lett. **78**, 4978–4981 (1997).
- [42] T. R. Linderoth, S. Horch, E. Laegsgaard, I. Stensgaard, and F. Besenbacher, *Dynamics of Pt adatoms and dimers on Pt(110)-(1x2) observed directly by STM*, Surf. Sci. **404**, 308–312 (1998).
- [43] T. Tansel and O. M. Magnussen, *Video STM studies of adsorbate diffusion at electrochemical interfaces*, Phys. Rev. Lett. **96**, 026101 (2006).
- [44] S. Arrhenius, *Über die Reaktionsgeschwindigkeit bei der Inversion von Rohrzucker in Säuren*, Z. Phys. Chem. **4**, 226–248 (1889).
- [45] A. Zangwill, *Physics at surfaces*, Cambridge University Press (1988).
- [46] Michael Schunack, *Scanning Tunneling Microscopy Studies of Organic Molecules on Metal Surfaces*, Ph.D. thesis, University of Aarhus, Denmark (2002).
- [47] R. Gomer, *Diffusion of adsorbates on metal-surfaces*, Reports on Progress in Physics **53**, 917–1002 (1990).

- [48] M. Schunack, T. R. Linderoth, F. Rosei, E. Laegsgaard, I. Stensgaard, and F. Besenbacher, *Long jumps in the surface diffusion of large molecules*, Phys. Rev. Lett. **88**, 156102 (2002).
- [49] K. D. Dobbs and D. J. Doren, *Dynamics of molecular-surface diffusion: Origins and consequences of long jumps*, J. Chem. Phys. **97**, 3722–3735 (1992).
- [50] E. J. Scheibner, L. H. Germer, and C. D. Hartman, *Apparatus for Direct Observation of Low-Energy Electron Diffraction Patterns*, Rev. Sci. Instrum. **31**, 112 (1960).
- [51] C. Davisson and L. H. Germer, *Diffraction of Electrons by a Crystal of Nickel*, Physical Review **30**, 705 (1927).
- [52] N. W. Ashcroft and N. D. Mermin, *Solid state physics*, Saunders College Publishing (1976).
- [53] Charles Kittel, *Introduction to Solid State Physics*, John Wiley & Sons, New York (1986).
- [54] Jens Als-Nielsen and Des McMorrow, *Elements of Modern X-Ray Physics*, John Wiley and Sons, Chichester (2001).
- [55] E. A. Wood, *Vocabulary of surface crystallography*, J. Appl. Phys. **35**, 1306–& (1964).
- [56] M. A. Van Hove, W. H. Weinberg, and C.-M. Chan, *Low-Energy Electron Diffraction, Experiment, Theory and Surface Structure Determination*, Springer (1986).
- [57] K. Heinz, *Structural analysis of surfaces by LEED*, Prog. Surf. Sci. **27**, 239 (1988).
- [58] Heinrich Hertz, *Über einen Einfluss des ultravioletten Lichtes auf die elektrische Entladung*, Ann. Phys.-Berlin **31**, 983 (1887).
- [59] A. Einstein, *Über einen die Erzeugung und Verwandlung des Lichts betreffenden heuristischen Gesichtspunkt*, Ann. Phys.-Berlin **17**, 132 (1905).
- [60] K. Siegbahn, C. Nordling, R. Fahlman, R. Nordberg, K. Hamrin, J. Hedman, G. Johansson, T. Bergmark, S.-E. Karlsson, I. Lindgren, and B. Lindberg, *ESCA, Atomic, Molecular and Solid State Structure Studies by Means of Electron Spectroscopy*, vol. 20 of 4, Almquist & Wiksells Boktryckeri (1967).
- [61] R. G. Musket, W. Mc Lean, C. A. Colmenares, D. M. Makowiecki, and W. J. Siekhaus, *Preparation of atomically clean surfaces of selected elements: a review*, Application of Surface Science **10**, 143 (1982).
- [62] S. Berner, *Molecular diffusion and self-organization on metal surfaces: sub-phthalocyanine on Ag(111)*, Ph.D. thesis, Universität Basel (2002).
- [63] T. M. Schaub, *Untersuchung nichtperiodischer Oberflächen im Ultrahochvakuum mittels Rastertunnelmikroskopie*, Ph.D. thesis, Universität Basel (1994).
- [64] D. E. Bürgler, C. M. Schmidt, J. A. Wolf, T. M. Schaub, and H.-J. Güntherodt, *Ag films on Fe/GaAs(001): from clean surfaces to atomic Ga structures*, Surf. Sci. **366**, 295 (1996).

- [65] F. Meisinger, *Rastersondenmikroskopie an magnetischen Systemen*, Ph.D. thesis, Universität Basel (2000).
- [66] C. M. Schmidt, *Magnetic Interlayer Exchange Coupling in Fe/Cr/Fe(001) Trilayers is Correlated to Nanometer Scale Lateral Interface Structure*, Ph.D. thesis, Universität Basel (1988).
- [67] Luca Ramoino, *Adsorption and Self-Organization of CuOEP on Heterogeneous Surfaces: Tuning the Molecule-Substrate Interaction*, Ph.D. thesis, Universität Basel (2005).
- [68] F. Schreiber, *Structure and growth of self-assembling monolayers*, Prog. Surf. Sci. **65**, 151–256 (2000).
- [69] S. De Feyter and F. C. De Schryver, *Two-dimensional supramolecular self-assembly probed by scanning tunneling microscopy*, Chem. Soc. Rev. **32**, 139–150 (2003).
- [70] F. Rosei, M. Schunack, Y. Naitoh, P. Jiang, A. Gourdon, E. Laegsgaard, I. Stensgaard, C. Joachim, and F. Besenbacher, *Properties of large organic molecules on metal surfaces*, Prog. Surf. Sci. **71**, 95–146 (2003).
- [71] J. Bailey, A. Chrysostomou, J. H. Hough, T. M. Gledhill, A. McCall, S. Clark, F. Menard, and M. Tamura, *Circular polarization in star-formation regions: Implications for biomolecular homochirality*, Science **281**, 672–674 (1998).
- [72] S. P. Mathew, H. Iwamura, and D. G. Blackmond, *Amplification of enantiomeric excess in a proline-mediated reaction*, Angew. Chem., Int. Ed. **43**, 3317–3321 (2004).
- [73] H. Becker and K. B. Sharpless, *Asymmetric Oxidation Reactions: A Practical Approach in Chemistry*, Oxford University Press New York (2001).
- [74] R. Noyori, *Asymmetric catalysis: Science and opportunities.*, Adv. Synth. Catal. **345**, 15–32 (2003).
- [75] W. S. Knowles, *Asymmetric hydrogenations*, Adv. Synth. Catal. **345**, 3–13 (2003).
- [76] N. Künzle, R. Hess, T. Mallat, and A. Baiker, *Continuous enantioselective hydrogenation of activated ketones*, J. Catal. **186**, 239–241 (1999).
- [77] A. Baiker, *Chiral catalysis on solids*, Curr. Opin. Solid State Mater. Sci. **3**, 86–93 (1998).
- [78] Thomas Bürgi and Alfons Baiker, *Heterogeneous Enantioselective Hydrogenation over Cinchona Alkaloid Modified Platinum: Mechanistic Insights into a Complex Reaction*, Acc. Chem. Res. **37**, 909–917 (2004).
- [79] Matthias von Arx, *Platinum-Catalyzed Enantioselective Hydrogenation of Trifluoromethyl Ketones*, Ph.D. thesis, Swiss Federal Institute of Technology (ETH), Zurich (2001).
- [80] T. Osawa, T. Harada, and O. Takayasu, *Progress of enantio-differentiating hydrogenation of prochiral ketones over asymmetrically modified nickel catalysts and a newly proposed enantio-differentiation model*, Top. Catal. **13**, 155–168 (2000).

- [81] T. Sugimura, *Recent progress in tartaric acid-modified Raney nickel system for enantio-differentiating hydrogenation*, Catalysis Surveys from Japan **3**, 37–42 (1999).
- [82] M. von Arx, T. Mallat, and A. Baiker, *Asymmetric hydrogenation of activated ketones on platinum: relevant and spectator species*, Top. Catal. **19**, 75–87 (2002).
- [83] M. Studer, H. U. Blaser, and C. Exner, *Enantioselective hydrogenation using heterogeneous modified catalysts: An update*, Adv. Synth. Catal. **345**, 45–65 (2003).
- [84] P. B. Wells and A. G. Wilkinson, *Platinum group metals as heterogeneous enantioselective catalysts*, Top. Catal. **5**, 39–50 (1998).
- [85] W. R. Huck, T. Mallat, and A. Baiker, *Heterogeneous enantioselective hydrogenation of 2-pyrone over cinchona-modified palladium*, New J. Chem. **26**, 6–8 (2002).
- [86] Y. Nitta and A. Shibata, *Enantioselective hydrogenation of (E)-alpha-phenylcinnamic acid on Pd/TiO₂ catalyst modified by cinchona alkaloids: Effect of modifier structure*, Chem. Lett. pp. 161–162 (1998).
- [87] M. O. Lorenzo, C. J. Baddeley, C. Muryn, and R. Raval, *Extended surface chirality from supramolecular assemblies of adsorbed chiral molecules*, Nature **404**, 376–379 (2000).
- [88] V. Humblot, S. Haq, C. Muryn, W. A. Hofer, and R. Raval, *From local adsorption stresses to chiral surfaces: (R,R)-tartaric acid on Ni(110)*, J. Am. Chem. Soc. **124**, 503–510 (2002).
- [89] T. E. Jones and C. J. Baddeley, *A RAIRS, STM and TPD study of the Ni111/R,R-tartaric acid system: Modelling the chiral modification of Ni nanoparticles*, Surf. Sci. **513**, 453–467 (2002).
- [90] J. M. Bonello, R. M. Lambert, N. Künzle, and A. Baiker, *Platinum-catalyzed enantioselective hydrogenation of alpha-ketoesters: An unprecedented surface reaction of methyl pyruvate*, J. Am. Chem. Soc. **122**, 9864–9865 (2000).
- [91] J. M. Bonello, F. J. Williams, and R. M. Lambert, *Aspects of enantioselective heterogeneous catalysis: structure and reactivity of (S)-(-)-1-(1-naphthyl)ethylamine on Pt111*, J. Am. Chem. Soc. **125**, 2723–2729 (2003).
- [92] T. Heinz, G. Z. Wang, A. Pfaltz, B. Minder, M. Schürch, T. Mallat, and A. Baiker, *1-(1-naphthyl)ethylamine and derivatives thereof as chiral modifiers in the enantioselective hydrogenation of ethyl pyruvate over Pt-alumina*, Chem. Commun. **14**, 1421–1422 (1995).
- [93] Q. M. Xu, D. Wang, L. J. Wan, C. L. Bai, and Y. Wang, *Adsorption mode of cinchonidine on Cu(111) surface*, J. Am. Chem. Soc. **124**, 14300–14301 (2002).
- [94] Q. M. Xu, D. Wang, M. J. Han, L. J. Wan, and C. L. Bai, *Direct STM investigation of cinchona alkaloid adsorption on Cu(111)*, Langmuir **20**, 3006–3010 (2004).
- [95] D. Friebel, T. Mangen, B. Obliers, C. Schlaup, P. Broekmann, and K. Wandelt, *On the existence of ordered organic adlayers at the Cu(111)/electrolyte interface*, Langmuir **20**, 2803–2806 (2004).

- [96] F.A. Carey and R.J. Sundberg, *Advanced organic chemistry*, Plenum Press, New York, 3rd ed. (1990).
- [97] R.A. Sheldon, *Chirotechnology*, Marcel Dekker, New York (1993).
- [98] R. S. Cahn, C. Ingold, and V. Prelog, *Specification of molecular chirality*, *Angew. Chem., Int. Ed.* **5**, 385 (1966).
- [99] V. Prelog and G. Helmchen, *Basic principles of the CIP-system and proposals for a revision*, *Angew. Chem., Int. Ed.* **21**, 567–583 (1982).
- [100] Y. Orito, S. Imai, S. Niwa, and N.G. Hung, *Asymmetric hydrogenation of methyl benzoylformate using platinum-carbon catalyst modified with cinchonidine*, *J. Synth. Org. Chem. Japan* **37**, 173 (1979).
- [101] Y. Orito, S. Imai, and S. Niwa, *Asymmetric hydrogenation of methyl pyruvate using Pt-C catalyst modified with cinchonidine*, *Nippon Kagaku Kaishi* **8**, 1118 (1979).
- [102] Y. Orito, S. Imai, and S. Niwa, *Asymmetric hydrogenation of Alpha-Keto esters using platinum-alumina catalyst modified with cinchona alkaloid*, *Nippon Kagaku Kaishi* **4**, 670–672 (1980), *Journal of the Chemical Society Japan*.
- [103] Y. Orito, S. Imai, and S. Niwa, *Asymmetric hydrogenation of ethyl benzoylformate using the platinum-carbon catalyst modified with cinchonidine - Influence of preparation of the catalyst on the asymmetric selectivity*, *Nippon Kagaku Kaishi* **1**, 137 (1982).
- [104] G.V. Smith and F. Notheisz, *Heterogeneous Catalysis in Organic Chemistry*, Academic Press, San Diego (1999).
- [105] P. B. Wells, K. E. Simons, J. A. Slipszenko, S. P. Griffiths, and D. F. Ewing, *Chiral environments at alkaloid-modified platinum surfaces*, *J. Mol. Catal. A: Chem.* **146**, 159–166 (1999).
- [106] A. Baiker, *Transition state analogues A guide for the rational design of enantioselective heterogeneous hydrogenation catalysts*, *J. Mol. Catal. A: Chem.* **163**, 205–220 (2000).
- [107] O. Schwalm, B. Minder, J. Weber, and A. Baiker, *Enantioselective hydrogenation of alpha-ketoesters over Pt/alumina modified with cinchonidine - Theoretical investigation of the substrate-modifier interaction*, *Catal. Lett.* **23**, 271–279 (1994).
- [108] A. Vargas, T. Bürgi, M. von Arx, R. Hess, and A. Baiker, *Relation between electronic structure of alpha-substituted ketones and their reactivity in racemic and enantioselective platinum-catalyzed hydrogenation*, *J. Catal.* **209**, 489–500 (2002).
- [109] M. Schürch, O. Schwalm, T. Mallat, J. Weber, and A. Baiker, *Enantioselective hydrogenation of ketopantolactone*, *J. Catal.* **169**, 275–286 (1997).
- [110] M. Garland and H. U. Blaser, *A heterogeneous ligand-accelerated reaction: Enantioselective hydrogenation of ethyl pyruvate catalyzed by cinchona-modified Pt/Al₂O₃*, *J. Am. Chem. Soc.* **112**, 7048–7050 (1990).

- [111] G. Bond, K. E. Simons, A. Ibbotson, P. B. Wells, and D. A. Whan, *Platinum-catalyzed enantioselective hydrogenation effects of low coverage of modifier*, Catal. Today **12**, 421–425 (1992).
- [112] A. Baiker, *Progress in asymmetric heterogeneous catalysis: Design of novel chirally modified platinum metal catalysts*, J. Mol. Catal. A: Chem. **115**, 473–493 (1997).
- [113] B. Minder, T. Mallat, K.H. Pickel, K. Steiner, and A. Baiker, *Enantioselective hydrogenation of ethyl pyruvate in supercritical fluids*, Catal. Lett. **34**, 1–9 (1995).
- [114] H. U. Blaser, H. P. Jalett, and J. Wiehl, *Enantioselective hydrogenation of alpha-ketoesters with cinchona-modified platinum catalysts - Effect of acidic and basic solvents and additives*, J. Mol. Catal. **68**, 215–222 (1991).
- [115] A. Vargas, T. Bürgi, and A. Baiker, *Adsorption of cinchonidine on platinum: a DFT insight in the mechanism of enantioselective hydrogenation of activated ketones*, J. Catal. **226**, 69–82 (2004).
- [116] D. Klyachko and D.M. Chen, *Cluster shapes in STM images of isolate clusters and cluster materials*, Surf. Sci. **446**, 98–102 (2000).
- [117] M. von Arx, M. Wahl, T. A. Jung, and A. Baiker, *Adsorption and surface mobility of cinchonidine on Pt(111) studied by STM*, Phys. Chem. Chem. Phys. **7**, 273–277 (2005).
- [118] T. Bürgi and A. Baiker, *Conformational behavior of cinchonidine in different solvents: A combined NMR and ab initio investigation*, J. Am. Chem. Soc. **120**, 12920–12926 (1998).
- [119] G. D. H. Dijkstra, R. M. Kellogg, H. Wynberg, J. S. Svendsen, I. Marko, and K. B. Sharpless, *Conformational study of cinchona alkaloids - A combined NMR, molecular mechanics and X-ray approach*, J. Am. Chem. Soc. **111**, 8069–8076 (1989).
- [120] S. R. Calvo, R. J. LeBlanc, C. T. Williams, and P. B. Balbuena, *Molecular dynamics simulations of cinchonidine-modified platinum in ethanol: comparisons with surface studies*, Surf. Sci. **563**, 57–73 (2004).
- [121] D. Ferri, T. Bürgi, and A. Baiker, *Chiral modification of platinum catalysts by cinchonidine adsorption studied by in situ ATR-IR spectroscopy*, Chem. Commun. pp. 1172–1173 (2001).
- [122] D. Ferri and T. Bürgi, *An in situ attenuated total reflection infrared study of a chiral catalytic solid-liquid interface: Cinchonidine adsorption on Pt*, J. Am. Chem. Soc. **123**, 12074–12084 (2001).
- [123] H. U. Blaser, H. P. Jalett, W. Lottenbach, and M. Studer, *Heterogeneous enantioselective hydrogenation of ethyl pyruvate catalyzed by cinchona-modified Pt catalysts: Effect of modifier structure*, J. Am. Chem. Soc. **122**, 12675–12682 (2000).
- [124] M. Bartok, T. Bartok, G. Szollosi, and K. Felfoldi, *Electrospray ionization mass spectrometry in the heterogeneous catalyzed organic reactions: unknown compounds in the pyruvate hydrogenation*, Catal. Lett. **61**, 57–60 (1999).

- [125] S. Y. Bhide and S. Yashonath, *Dependence of the self-diffusion coefficient on the sorbate concentration: A two-dimensional lattice gas model with and without confinement*, J. Chem. Phys. **111**, 1658–1667 (1999).
- [126] J. T. Goldstein and G. Ehrlich, *Site blocking in surface diffusion*, Surf. Sci. **420**, 1–5 (1999).
- [127] D. A. Reed and G. Ehrlich, *Surface diffusivity and the time correlation of concentration fluctuations*, Surf. Sci. **105**, 603–628 (1981).
- [128] J. M. Bonello, R. Lindsay, A. K. Santra, and R. M. Lambert, *On the orientation of quinoline on Pd111: Implications for heterogeneous enantioselective hydrogenation*, J. Phys. Chem. B **106**, 2672–2679 (2002).
- [129] S. Diezi, A. Szabo, T. Mallat, and A. Baiker, *Inversion of enantioselectivity in the hydrogenation of ketopantolactone on platinum modified by ether derivatives of cinchonidine*, Tetrahedron-Asymmetry **14**, 2573–2577 (2003).
- [130] W. R. Huck, T. Bürgi, T. Mallat, and A. Baiker, *Asymmetric hydrogenation on platinum: nonlinear effect of coadsorbed cinchona alkaloids on enantiodifferentiation*, J. Catal. **216**, 276–287 (2003).
- [131] I. Bakos, S. Szabo, M. Bartok, and E. Kalman, *Adsorption of cinchonidine on platinum: an electrochemical study*, J. Electroanal. Chem. **532**, 113–119 (2002).
- [132] A. Vargas, D. Ferri, and A. Baiker, *DFT and ATR-IR insight into the conformational flexibility of cinchonidine adsorbed on platinum: Proton exchange with metal*, J. Catal. **236**, 1–8 (2005).
- [133] Angelo Vargas and Alfons Baiker, *First Principles Study of the Conformation of Cinchonidine on a Pt(111) Surface*, J. Catal. **239**, 220 (2006).
- [134] Y. Nitta, J. Watanabe, T. Okuyama, and T. Sugimura, *Activation-temperature dependence in enantioselective hydrogenation of unsaturated carboxylic acids over cinchonidine-modified Pd/C catalysts*, J. Catal. **236**, 164–167 (2005).
- [135] D. Ferri, T. Bürgi, and A. Baiker, *In situ ATR-IR study of the adsorption of cinchonidine on Pd/Al₂O₃: Differences and similarities with adsorption on Pt/Al₂O₃*, J. Catal. **210**, 160–170 (2002).
- [136] J.N. Israelachvili, *Intermolecular and Surface Forces*, Academic Press, 2nd ed. (1992).
- [137] T. Zambelli, J. Wintterlin, J. Trost, and G. Ertl, *Identification of the "active sites" of a surface-catalyzed reaction*, Science **273**, 1688–1690 (1996).
- [138] M. Wahl, M. von Arx, T. A. Jung, and A. Baiker, *Time-Lapse STM Studies of Diastereomeric Cinchona Alkaloids on Platinum Metals*, J. Phys. Chem. B **110**, 21777–21782 (2006).
- [139] M. Bartok, K. Felfoldi, B. Torok, and T. Bartok, *A new cinchona-modified platinum catalyst for the enantioselective hydrogenation of pyruvate: the structure of the 1 : 1 alkaloid-reactant complex*, Chem. Commun. **23**, 2605–2606 (1998).

- [140] S. Berner, S. Biela, G. Ledung, A. Gogoll, J.-E. Bäckvall, C. Puglia, and S. Oscarsson, *Activity boost of a biomimetic oxidation catalyst by immobilization onto a gold surface*, *J. Catal.* **244**, 86–91 (2006).
- [141] G.E. Moore, *Cramming more components onto integrated circuits*, *Electronics* **38**, 114–117 (1965).
- [142] K. Ziemelis, *The future of microelectronics*, *Nature* **406**, 1021–1021 (2000).
- [143] Rainer Waser, *Nanoelectronics and Information Technology*, Wiley-VCH (2003).
- [144] J. D. Meindl, *Low-power microelectronics retrospect and prospect*, *Proceedings of the IEEE* **83**, 619–635 (1995).
- [145] J. D. Meindl, Q. Chen, and J. A. Davis, *Limits on silicon nanoelectronics for terascale integration*, *Science* **293**, 2044–2049 (2001).
- [146] M.A. Nielsen and I.L. Chuang, *Quantum Computation and Quantum Information*, Cambridge University Press (2000).
- [147] ITRS, *International Technology Roadmap for Semiconductors*, Tech. rep., ITRS (2005).
- [148] G. M. Whitesides, J. P. Mathias, and C. T. Seto, *Molecular Self-Assembly and Nanochemistry - A Chemical Strategy for the Synthesis of Nanostructures*, *Science* **254**, 1312–1319 (1991).
- [149] J.-M. Lehn, *Supramolecular Chemistry: Concepts and Perspectives*, VCH, Weinheim (1995).
- [150] For a collection of recent overviews of the principle of molecular self-assembly, see the whole volume of *Science* **295** (2002).
- [151] T. Yokoyama, S. Yokoyama, T. Kamikado, Y. Okuno, and S. Mashiko, *Selective assembly on a surface of supramolecular aggregates with controlled size and shape*, *Nature* **413**, 619–621 (2001).
- [152] S. Ito, M. Wehmeier, J. D. Brand, C. Kubel, R. Epsch, J. P. Rabe, and K. Mullen, *Synthesis and self-assembly of functionalized hexa-peri-hexabenzocoronenes*, *Chem.–Eur. J.* **6**, 4327–4342 (2000).
- [153] J. Weckesser, A. De Vita, J. V. Barth, C. Cai, and K. Kern, *Mesoscopic correlation of supramolecular chirality in one-dimensional hydrogen-bonded assemblies*, *Phys. Rev. Lett.* **8709**, 096101 (2001).
- [154] A. Dmitriev, N. Lin, J. Weckesser, J. V. Barth, and K. Kern, *Supramolecular assemblies of trimesic acid on a Cu(100) surface*, *J. Phys. Chem. B* **106**, 6907–6912 (2002).
- [155] M. de Wild, S. Berner, H. Suzuki, H. Yanagi, D. Schlettwein, S. Ivan, A. Baratoff, H. J. Güntherodt, and T. A. Jung, *A novel route to molecular self-assembly: Self-intermixed monolayer phases*, *ChemPhysChem* **3**, 881–885 (2002).

- [156] S. De Feyter, M. Larsson, N. Schuurmans, B. Verkuijl, G. Zorinants, A. Gesquiere, M. M. Abdel-Mottaleb, J. van Esch, B. L. Feringa, J. van Stam, and F. De Schryver, *Supramolecular control of two-dimensional phase behavior*, Chem.–Eur. J. **9**, 1198–1206 (2003).
- [157] D. Bonifazi, H. Spillmann, A. Kiebele, M. de Wild, P. Seiler, F. Y. Cheng, H. J. Guntherodt, T. Jung, and F. Diederich, *Supramolecular patterned surfaces driven by cooperative assembly of C-60 and porphyrins on metal substrates*, Angew. Chem., Int. Ed. **43**, 4759–4763 (2004).
- [158] L. Brunsveld, B. J. B. Folmer, E. W. Meijer, and R. P. Sijbesma, *Supramolecular polymers*, Chem. Rev. **101**, 4071–4097 (2001).
- [159] A. Dmitriev, H. Spillmann, N. Lin, J. V. Barth, and K. Kern, *Modular assembly of two-dimensional metal-organic coordination networks at a metal surface*, Angew. Chem. Int. Ed. **42**, 2670–2673 (2003).
- [160] J. A. Theobald, N. S. Oxtoby, M. A. Phillips, N. R. Champness, and P. H. Beton, *Controlling molecular deposition and layer structure with supramolecular surface assemblies*, Nature **424**, 1029–1031 (2003).
- [161] H. Ozaki, T. Funaki, Y. Mazaki, S. Masuda, and Y. Harada, *Single sheet of a quasi-planar macromolecule prepared by photopolymerization at a solid-surface*, J. Am. Chem. Soc. **117**, 5596–5597 (1995).
- [162] H. Ozaki, M. Kasuga, T. Tsuchiya, T. Funaki, Y. Mazaki, M. Aoki, S. Masuda, and Y. Harada, *Formation of atomic cloth observed by Penning Ionization Electron-Spectroscopy*, J. Chem. Phys. **103**, 1226–1228 (1995).
- [163] Y. Okawa and M. Aono, *Materials science Nanoscale control of chain polymerization*, Nature **409**, 683–684 (2001).
- [164] B. Grevin, P. Rannou, R. Payerne, A. Pron, and J. P. Travers, *Multi-scale scanning tunneling microscopy imaging of self-organized regioregular poly(3-hexylthiophene) films*, J. Chem. Phys. **118**, 7097–7102 (2003).
- [165] E. Mena-Osteritz, A. Meyer, B. M. W. Langeveld-Voss, R. A. J. Janssen, E. W. Meijer, and P. Bauerle, *Two-dimensional crystals of poly(3-alkylthiophene)s: Direct visualization of polymer folds in submolecular resolution*, Angew. Chem. Int. Ed. **39**, 2680–2684 (2000).
- [166] H. Sakaguchi, H. Matsumura, and H. Gong, *Electrochemical epitaxial polymerization of single-molecular wires*, Nat. Mater. **3**, 551–557 (2004).
- [167] N. Karl and C. Günther, *Structure and ordering principles of ultrathin organic molecular films on surfaces of layered semiconductors organic-on-inorganic MBE*, Cryst. Res. Technol. **34**, 243–254 (1999).
- [168] E. Umbach, M. Sokolowski, and R. Fink, *Substrate-interaction, long-range order, and epitaxy of large organic adsorbates*, Appl. Phys. A: Mater. Sci. Process. **63**, 565–576 (1996).

- [169] C.C. Leznoff and A.B.P. Lever, eds., *Phthalocyanines: Properties and Applications*, John Wiley & Sons (1993).
- [170] S. R. Forrest, *Ultrathin organic films grown by organic molecular beam deposition and related techniques*, Chem. Rev. **97**, 1793–1896 (1997).
- [171] G. Witte and C. Wöll, *Growth of aromatic molecules on solid substrates for applications in organic electronics*, J. Mater. Res. **19**, 1889–1916 (2004).
- [172] M. Möbus, N. Karl, and T. Kobayashi, *Structure of perylene-tetracarboxylic-dianhydride thin-films on alkali-halide crystal substrates*, J. Cryst. Growth **116**, 495–504 (1992).
- [173] A. J. Lovinger, S. R. Forrest, M. L. Kaplan, P. H. Schmidt, and T. Venkatesan, *Structural and Morphological Investigation of the Development of Electrical-Conductivity in Ion-Irradiated Thin-Films of an Organic Material*, J. Appl. Phys. **55**, 476–482 (1984).
- [174] K. Glöckler, C. Seidel, A. Soukopp, M. Sokolowski, E. Umbach, M. Böhringer, R. Berndt, and W. D. Schneider, *Highly ordered structures and submolecular scanning tunnelling microscopy contrast of PTCDA and DM-PBDCI monolayers on Ag(111) and Ag(110)*, Surf. Sci. **405**, 1–20 (1998).
- [175] C. Ludwig, B. Gompf, J. Petersen, R. Strohmaier, and W. Eisenmenger, *STM investigations of PTCDA and PTCDI on graphite and MoS₂ - A systematic study of epitaxy and STM image-contrast*, Zeitschrift für Physik B - Condensed Matter **93**, 365–373 (1994).
- [176] G. Horowitz, *Organic field-effect transistors*, Adv. Mater. **10**, 365–377 (1998).
- [177] C. D. Dimitrakopoulos and D. J. Masearo, *Organic thin-film transistors: A review of recent advances*, IBM Journal of Research and Development **45**, 11–27 (2001).
- [178] D. A. Pardo, G. E. Jabbour, and N. Peyghambarian, *Application of screen printing in the fabrication of organic light-emitting devices*, Adv. Mater. **12**, 1249 (2000).
- [179] C. W. Tang and S. A. VanSlyke, *Organic Electroluminescent Diodes*, Appl. Phys. Lett. **51**, 913–915 (1987).
- [180] A. Zinke, W. Hirsch, and E. Brozek, *Untersuchungen über Perylen und seine Derivate*, Monatsh. Chem. **51**, 205–220 (1929).
- [181] K. W. Hellmann, C. H. Galka, I. Rudenauer, L. H. Gade, I. J. Scowen, and M. McPartlin, *Metal-ligand versus metal-metal redox chemistry: Thallium(I)-induced synthesis of 4,9-diaminoperylenequinone-3,10-diimine derivatives*, Angew. Chem., Int. Ed. **37**, 1948–1952 (1998).
- [182] L. H. Gade, C. H. Galka, K. W. Hellmann, R. M. Williams, L. De Cola, I. J. Scowen, and M. McPartlin, *Tetraaminoperylenes: Their efficient synthesis and physical properties*, Chem.–Eur. J. **8**, 3732–3746 (2002).
- [183] M. Eremtchenko, J. A. Schaefer, and F. S. Tautz, *Understanding and tuning the epitaxy of large aromatic adsorbates by molecular design*, Nature **425**, 602–605 (2003).

- [184] M. Eremtchenko, D. Bauer, J. A. Schaefer, and F. S. Tautz, *Polycyclic aromates on close-packed metal surfaces: functionalization, molecular chemisorption and organic epitaxy*, New J. Phys. **6**, 4 (2004).
- [185] A. Hauschild, K. Karki, B. C. C. Cowie, M. Rohlfing, F. S. Tautz, and M. Sokolowski, *Molecular distortions and chemical bonding of a large pi-conjugated molecule on a metal surface*, Phys. Rev. Lett. **94**, 036106 (2005).
- [186] H. Itoh, T. Ichinose, C. Oshima, T. Ichinokawa, and T. Aizawa, *Scanning tunneling microscopy of monolayer graphite epitaxially grown on at TiC(111) surface*, Surf. Sci. **254**, L437–L442 (1991).
- [187] T. A. Land, T. Michely, R. J. Behm, J. C. Hemminger, and G. Comsa, *STM investigation of single layer graphite structures produced on Pt(111) by hydrocarbon decomposition*, Surf. Sci. **264**, 261–270 (1992).
- [188] K. Kobayashi, *Moire pattern in scanning-tunneling-microscopy of monolayer graphite*, Phys. Rev. B **50**, 4749–4755 (1994).
- [189] K. Kobayashi, *Moire pattern in scanning tunneling microscopy: Mechanism in observation of subsurface nanostructures*, Phys. Rev. B **53**, 11091–11099 (1996).
- [190] K. Hermann and M. A. van Hove, *LEED pattern simulator LEEDPAT Version 2* (2002).
- [191] D. E. Hooks, T. Fritz, and M. D. Ward, *Epitaxy and molecular organization on solid substrates*, Adv. Mater. **13**, 227 (2001).
- [192] C. Schwennicke, J. Schimmelpfennig, and H. Pfnür, *Morphology of NaCl thin films grown epitaxially on Ge(100)*, Surf. Sci. **293**, 57 (1993).
- [193] K. Glöckler, M. Sokolowski, A. Soukopp, and E. Umbach, *Initial growth of insulating overlayers of NaCl on Ge(100) observed by scanning tunneling microscopy with atomic resolution*, Phys. Rev. B **54**, 7705 (1996).
- [194] J. Repp, *Rastertunnelmikroskopie und -spektroskopie an Adsorbaten auf Metall- und Isolatoroberflächen*, Ph.D. thesis, Freie Universität Berlin (2002).
- [195] T. Steiner, *The hydrogen bond in the solid state*, Angew. Chem., Int. Ed. **41**, 48–76 (2002).
- [196] G. Gilli, F. Bellucci, V. Ferretti, and V. Bertolasi, *Evidence for resonance-assisted hydrogen-bonding from crystal-structure correlations on the enol form of the beta-diketone fragment*, J. Am. Chem. Soc. **111**, 1023–1028 (1989).
- [197] P. Gilli, V. Bertolasi, V. Ferretti, and G. Gilli, *Covalent nature of the strong homonuclear hydrogen-bond: Study of the O-H—O system by crystal-structure correlation methods*, J. Am. Chem. Soc. **116**, 909–915 (1994).
- [198] P. Gilli, V. Bertolasi, L. Pretto, V. Ferretti, and G. Gilli, *Covalent versus electrostatic nature of the strong hydrogen bond: Discrimination among single, double, and asymmetric single-well hydrogen bonds by variable-temperature X-ray crystallographic methods in beta-diketone enol RAHB systems*, J. Am. Chem. Soc. **126**, 3845–3855 (2004).

- [199] R. Otero, M. Schock, L. M. Molina, E. Laegsgaard, I. Stensgaard, B. Hammer, and F. Besenbacher, *Guanine quartet networks stabilized by cooperative hydrogen bonds*, *Angew. Chem., Int. Ed.* **44**, 2270–2275 (2005).
- [200] G. Louit, A. Hocquet, M. Ghomi, M. Meyer, and J. Suhnel, *Are guanine tetrads stabilised by bifurcated hydrogen bonds? An AIM topological analysis of the electronic density*, *PhysChemComm* pp. 94–98 (2002).
- [201] D. A. Shirley, *High-resolution X-ray photoemission spectrum of valence bands of gold*, *Phys. Rev. B* **5**, 4709–& (1972).
- [202] L. Pauling, *The nature of the chemical bond*, Oxford Univ. Press, Oxford (1950).
- [203] D.F. Shriver, P.W. Atkins, and C.H. Langford, *Inorganic Chemistry*, Oxford University Press (1995).
- [204] M. de Wild, *Novel Principle for 2D Molecular Self-Assembly: Self-Intermixed Monolayer Phases of Sub-Phthalocyanine and C₆₀ on Ag(111)*, Ph.D. thesis, Universität Basel (2002).
- [205] J. A. Theobald, N. S. Oxtoby, N. R. Champness, P. H. Beton, and T. J. S. Dennis, *Growth induced reordering of fullerene clusters trapped in a two-dimensional supramolecular network*, *Langmuir* **21**, 2038–2041 (2005).
- [206] H. W. Kroto, J. R. Heath, S. C. O’Brien, R. F. Curl, and R. E. Smalley, *C₆₀: Buckminsterfullerene*, *Nature* **318**, 162 (1985).
- [207] W. Krätschmer, L. Lamb, K. Fostiropoulos, and D. Huffman, *Solid C₆₀: A New Form of Carbon*, *Nature* **347**, 354 (1990).
- [208] M. T. Cuberes, R. R. Schlittler, and J. K. Gimzewski, *Room-temperature repositioning of individual C-60 molecules at Cu steps: Operation of a molecular counting device*, *Appl. Phys. Lett.* **69**, 3016–3018 (1996).
- [209] S. J. H. Griessl, M. Lackinger, F. Jamitzky, T. Markert, M. Hietschold, and W. M. Heckl, *Room-temperature scanning tunneling microscopy manipulation of single C-60 molecules at the liquid-solid interface: Playing nanosoccer*, *J. Phys. Chem. B* **108**, 11556–11560 (2004).
- [210] C. Joachim and J. K. Gimzewski, *An electromechanical amplifier using a single molecule*, *Chem. Phys. Lett.* **265**, 353–357 (1997).
- [211] C. Joachim, J. K. Gimzewski, and H. Tang, *Physical principles of the single-C-60 transistor effect*, *Phys. Rev. B* **58**, 16407–16417 (1998).
- [212] T. A. Jung, R. R. Schlittler, J. K. Gimzewski, H. Tang, and C. Joachim, *Controlled room-temperature positioning of individual molecules: Molecular flexure and motion*, *Science* **271**, 181–184 (1996).
- [213] L. L. Wang and H. P. Cheng, *Rotation, translation, charge transfer, and electronic structure of C-60 on Cu(111) surface*, *Phys. Rev. B* **69**, 045404 (2004).

- [214] K. Motai, T. Hashizume, H. Shinohara, Y. Saito, H. W. Pickering, Y. Nishina, and T. Sakurai, *C₆₀ grown on the Cu(111)1x1 surface*, Japanese Journal of Applied Physics Part 2 - Letters **32**, L450–L453 (1993).
- [215] P. Lambin, A. A. Lucas, and J. P. Vigneron, *Polarization-Waves and Van-Der-Waals Cohesion of C-60 fullerite*, Phys. Rev. B **46**, 1794–1803 (1992).
- [216] J. A. Stroscio and D. M. Eigler, *Atomic and Molecular Manipulation with the Scanning Tunneling Microscope*, Science **254**, 1319–1326 (1991).
- [217] S. W. Hla, L. Bartels, G. Meyer, and K. H. Rieder, *Inducing all steps of a chemical reaction with the scanning tunneling microscope tip: Towards single molecule engineering*, Phys. Rev. Lett. **85**, 2777–2780 (2000).
- [218] F. Moresco, *Manipulation of large molecules by low-temperature STM: model systems for molecular electronics*, Phys. Rep. **399**, 175–225 (2004).
- [219] R. Otero, F. Rosei, and F. Besenbacher, *Scanningtunneling microscopy manipulation of complex organic molecules on solid surfaces*, Annu. Rev. Phys. Chem. **57**, 497–525 (2006).
- [220] K. Ziegler, *Methoden der Anorganischen Chemie*, vol. IV, p. 729, Houben-Weyl (1955).
- [221] A. Lüttringhaus and H. Simon, Justus Liebigs Ann. Chem. **557**, 120 (1947).
- [222] P. Ruggli, *A ring with a threefold bond*, Justus Liebigs Annalen der Chemie **392**, 92–100 (1912).
- [223] S. Sellner, *Stehende Röntgenwellen und oberflächensensitive Röntgenstreuung an epitaktischen organischen Schichten*, Master's thesis, Max-Planck Institut für Metallforschung Stuttgart (2001).
- [224] D. P. Woodruff, *Surface structure determination using x-ray standing waves*, Reports on Progress in Physics **68**, 743–798 (2005).

List of Publications

Publications

- J. Major, H. Dosch, G.P. Felcher, K. Habicht, T. Keller, S.G.E. te Velthuis, A. Vorobiev and M. Wahl, *Combining of neutron spin echo and reflectivity: a new technique for probing surface and interface order*, Physica B **336** (2003) 8-15
- M. von Arx, M. Wahl, T.A. Jung and A. Baiker, *Adsorption and surface mobility of cinchonidine on Pt(111) studied by STM*, Phys. Chem. Chem. Phys. **7** (2005) 273-277
- M. Stöhr, M. Wahl, C.H. Galka, T. Riehm, T.A. Jung, and L.H. Gade, *Controlling Molecular Assembly in Two Dimensions: The Concentration Dependence of Thermally Induced 2D Aggregation of Molecules on a Metal Surface*, Angew. Chem. Int. Ed. **44** (2005) 7394 -7398 (Highlighted in Science **310** (2005) 1392)
- M. Wahl, M. von Arx, T.A. Jung and A. Baiker, *Time-lapse STM studies of Diastereomeric Cinchona-alkaloids on Platinum*, J. Phys. Chem. B. **110** (2006) 21777-21782
- M. Wahl, M. Stöhr, H. Spillmann, T.A. Jung, L.H. Gade, *Rotation-libration in a hierarchic supra-molecular rotor-stator system: Arrhenius activation and retardation by local interaction*, submitted
- L. Ramoino, S. Schintke, M. von Arx, M. Wahl, A. Alkauskas, A. Baratoff, H.-J. Güntherodt, T.A. Jung, *Adsorption geometry and tunneling voltage-dependent submolecular contrast of copper octaethylporphyrin adsorbed on metals and ultrathin insulators*, in preparation
- A. Scheybal, R. Bertschinger, K. Müller, M. Wahl, P. Aebi, T.A. Jung, *Modification of the Cu(110) Shockley surface state by an adsorbed pentacene monolayer*, in preparation

Conference Presentations

- M. Wahl, M. Stöhr, M. de Wild, H.-J. Güntherodt, C.H. Galka, L.H. Gade, T.A. Jung, *Polymerization of planar molecular networks*, SPM Workshop, University of Bielefeld, Germany, September 2004, talk
- M. Wahl, M. Stöhr, M. de Wild, H.-J. Güntherodt, C.H. Galka, L.H. Gade, T.A. Jung, *Polymerization of planar molecular networks*, TNT2004 Trends in Nanotechnology, Segovia, Spain, September 2004, talk
- M. Wahl, M. von Arx, T.A. Jung, A. Baiker, *Adsorption and surface mobility of cinchonidine on Pt(111) studied by STM*, Swiss Chemical Society Fall Meeting, Zürich, Switzerland, Oktober 2004, poster

- M. Wahl, M. von Arx, T.A. Jung, A. Baiker, *Adsorption and surface mobility of cinchonidine on Pt(111) studied by STM*, German Physical Society Spring Meeting, Berlin, Germany, March 2005, poster
- M. Wahl, M. Stöhr, T.A. Jung, H.-J. Güntherodt, L.H. Gade, *Building planar molecular networks by polymerization*, German Physical Society Spring Meeting, Berlin, Germany, March 2005, talk
- M. Wahl, M. Stöhr, T.A. Jung, H.-J. Güntherodt, L.H. Gade, *Generating coverage dependent supramolecular structures via a surface induced reaction*, Atomically Controlled Surfaces, Interfaces and Nanostructures 8, Stockholm, Sweden, June 2005, talk
- M. Wahl, M. Stöhr, T.A. Jung, L.H. Gade, H.-J. Güntherodt, *2D confinement of molecules - a possibility for new chemistry?*, LMN Seminar Paul Scherrer Institut, Villigen, Switzerland, Oktober 2005, invited talk
- M. Wahl, M. Stöhr, T. Riehm, T.A. Jung, L.H. Gade, *Intermixed patterns of perylene derivatives on Ag(111)*, German Physical Society Spring Meeting, Dresden, Germany, March 2006, talk
- M. Wahl, M. Stöhr, T. Riehm, T.A. Jung, L.H. Gade, *Trapping of guest molecules in supramolecular polymers*, International Conference on Nanoscience and Technology, Basel, Switzerland, August 2006, talk
- M. Wahl, M. Stöhr, T.A. Jung, L.H. Gade, *Trapping of guest molecules in supramolecular polymers*, European Conference on Surface Science, Paris, France, September 2006, talk

Acknowledgements

This thesis would not have been possible to realize without the support and the help of many people, whom I would like to thank at this place.

First of all, I am grateful to Prof. H.-J. Güntherodt and to Dr. T.A. Jung, who gave me the opportunity to work in the Nanolab in Basel and whose continuous support I could always count on. I also want to thank both and additionally Prof. E. Meyer for accepting to be referees of this thesis.

Special thanks belong to Matthias von Arx, who is an excellent scientist and was more than a PhD supervisor to me. To a great extent his managing competence and his social tact kept the Nanolab, the 'Anfängerpraktikum' and last but not least my PhD thesis running. It was a great pleasure to work with him in the lab and I wish him all the best with his pupils. "Matthias, do not hesitate to call if some furniture has to be moved around in your huge apartment!"

I also would like to thank Meike Stöhr for the time we spent together on the DPDI project. Meike was a great help while I was writing this thesis. She was an inexhaustible source of all sorts of references and did a great job in correcting my thesis. I wish her good luck for her scientific career and thank her very much for her help! "Although I do not confirm most of your STM image treatments, I have to admit that your images look great."

My office colleague Hannes Spillmann, I would like to thank for the nice discussions about science and life (wife) in general. We had a great time and I think he still owes us a visit with his little kids.

My former PhD colleague Luca Ramoino I want to thank for all the practical knowledge about the UHV equipment of the Nanolab system, that he managed to pass on to me. I always enjoyed working with him because he was interested in fundamental physical questions and nevertheless always open for a swim in the Rhy or a drink right on its waterfront.

Especially, I would like to acknowledge the kind and helpful collaboration received from all the people of the mechanical and electronic workshops, who really do an excellent job from which all PhDs profit a lot. I also owe Alexander Heuri a dept of gratitude because his work was invaluable for the tight schedule of running 4 to 5 different projects on one STM system. I always enjoyed our "repair sessions" together with Luca.

I'd like to thank G. Weaver, A. Kalt and B. Kammermann for the great work they do in mastering all the complicated bureaucratic issues for us.

I then want to express my gratitude to all the past and present members of the Nanolab and the whole Güntherodt and Meyer group which I met during my PhD time. All of them I thank for the friendly atmosphere and the numerous and very interesting discussions I had during my time in Basel.

Finally, I want to thank my family and all the friends who supported me during this time. Especially I want to honour my little brother Matthias at this place who always welcomes me warmly at home. And I want to thank my girlfriend Veronika who is far more valuable to me than this thesis, but who had to take second place especially during the end of this writing.

Curriculum Vitae

Markus Wahl

15.02.1977	geboren in Stuttgart, Deutschland
1983-1987	Besuch der <i>Grundschule</i> in Weinstadt-Schnait
1987-1996	Besuch des <i>Remstal-Gymnasiums</i> in Weinstadt
Juni 1996	Allgemeine Hochschulreife
1996 - 1997	Zivildienst
1997 - 1999	Vordiplom in Physik an der Universität Stuttgart
1999 - 2001	Hauptdiplom in Physik und Wirtschaftsingenieurwesen in Form eines internationalen Doppel-Diplom Programms an der <i>École Centrale de Paris</i> , Frankreich
2001 - 2003	Diplomarbeit am Max Planck Institut für Metallforschung Stuttgart in der Forschungsgruppe von Prof. Dr. H. Dosch <i>Aufbau einer Messanordnung zur Neutronenreflektometrie</i>
Feb. 2003	Abschluss des Studiums mit den akademischen Graden Diplom-Physiker (Dipl.-Phys.) und Ingénieur diplômé des Arts et Manufactures
März 2003 – Nov. 2006	Doktorarbeit und Assistentztätigkeit unter der Leitung von Dr. T. A. Jung in der Gruppe von Prof. H.-J. Güntherodt am Institut für Physik der Universität Basel, Schweiz

Folgenden Dozentinnen und Dozenten verdanke ich meine Ausbildung:

H. Dosch (S), H.J. Herrmann (S), W. Kimmerle (S), U. Kneisl (S), S. Luding (S), A. Muramatsu (S), M. Pilkuhn (S), K.W. Roggenkamp (S), M. Wagner (S), J. Weidlein (S), M. Abello (ECP), D. Aubry (ECP), P. Becker (ECP), J.-C. Bône (ECP), S. Candel (ECP), M. Chiroleux (ECP), B. Chouffrey (ECP), J.-M. Cognon (ECP), J.-C. Culioli (ECP), J.-L. Decornoy (ECP), T. Durand (ECP), J.-P. Fanton (ECP), P. Garderet (ECP), J.-J. Greffet (ECP), J.-B. Guillot (ECP), D. Hirondele (ECP), C. Lamoureux (ECP), P. Laurent (ECP), A. Leluan (ECP), B. Mammeri (ECP), J.-P. Moulin (ECP), D. Pareau (ECP), T. Phan (ECP), J. Taine (ECP), Y. Vandenboomgaerde (ECP), D. Verwaerde (ECP), J.-L. Zolésio (ECP), A. Baratoff (BS), S. Goedecker (BS), H.-J. Güntherodt (BS), E. Meyer (BS), T. Vetter (BS)

S: Universität Stuttgart

ECP: Ecole Centrale de Paris

BS: Universität Basel